

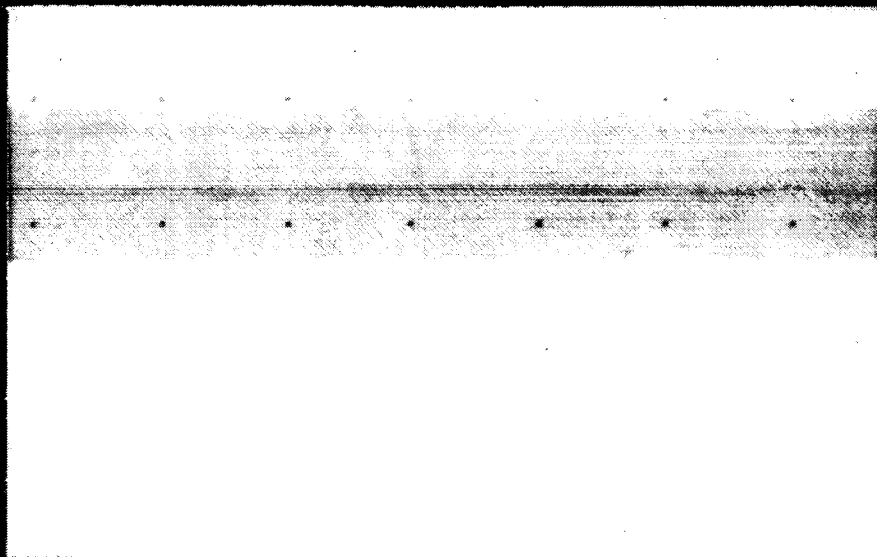


ENERGY
ENGINEERING
CENTER

Faculty of
Mechanical Engineering

המרכז
להנדסת
אנרגיה

ליד הפקולטה
להנדסת מכונות



(NASA-CR-180617) COMPUTATION OF ASYMMETRIC
SUPERSONIC FLOWS AROUND CONES AT LARGE
INCIDENCE Final Report (Technion - Israel
Inst. of Tech.) 88 p Avail: MIS HC
AG5/MF A01

N87-22114

Unclas

G3/34 0065666

RECEIVED BY
NASA STI FACILITY

DATE:

5/4/87

DCAF NO.

619800

PROCESSED BY

NASA STI FACILITY

ESA - SDS AIAA

Technion Research & Development Foundation LTD.
Technion City, Haifa, Israel

COMPUTATION OF ASYMMETRIC
SUPERSONIC FLOWS AROUND
CONES AT LARGE INCIDENCE

Final Report

NASA Grant No: NAGW-609

Supported by

National Aeronautics and Space Administration
Ames Research Center

Principal Investigator:

Prof. David Degani

Faculty of Mechanical Engineering

Technion, Israel Institute of Technology

Principal Investigator

D. Degani
D. Degani

Institution Administrator

Y. Dvir
Y. Dvir

1. Introduction

One of the current problems of interest in aerodynamics is understanding and controlling the development of the asymmetric flow which occurs when a simple body of revolution is placed at large angle of attack in subsonic flow. This phenomenon is of basic scientific interest, since it represents a bifurcation from a stable symmetric flow to an unstable symmetric (and stable asymmetric) flow as the angle of attack is increased. It is also of practical importance in the design of aircraft and missiles, since the side forces and yawing moments generated by the asymmetrical flow are surprisingly large, and can, in some instances, be larger than the normal force and pitching moment acting on the vehicle. Designers must take account of these large, nonlinear forces in sizing control surfaces and developing control systems. Thus, control of the onset of vortex asymmetry can result in improved performance and flight safety.

The phenomenon of vortex asymmetry was first observed experimentally in wind-tunnel tests conducted in the 1950's, and was then termed "phantom-yaw". Early flow-visualization experiments (Ref. 1) showed that at low angles of attack flow separates from the sides of a circular cross-section body and forms a symmetric pair of vortices on the leeward side of the body. When the angle of attack is increased beyond a critical value, the symmetric vortex pattern changes into a steady asymmetric pattern, and large side forces result. In the intervening thirty years a great number of experimental and analytical investigations have been carried out to document and understand vortex behavior (see, for example, Refs. 2-5). It has been found that the onset of vortex asymmetry is strongly influenced by several factors, including Reynolds number and the state of the boundary layer at the crossflow separation line, model smoothness, and tunnel turbulence level. Recent experimental results (Ref. 6,7), carried out in a low-turbulence wind tunnel, obtained detailed surface-pressure distributions over a range of Reynolds numbers ranging from fully laminar, through transitional, to "fully" turbulent. These results are particularly useful, since they permit delineation of the onset of vortex asymmetry from the boundary-layer transition phenomenon. In addition, they provide a detailed data base for verification of analytical methods.

Over the past three decades, many theoretical and computational methods have been developed and applied in attempting to predict the three-dimensional separated asymmetrical vortex flows. These have included methods based on the impulsive flow analogy, in which the steady three-dimensional flow over a body can be related to the evolution with time of the flow over a cylinder in crossflow (Ref. 8-10, for example). Also, vortex methods based on conical flow assumptions (Ref. 11) have

been employed. More recently, three-dimensional inviscid vortex-lattice methods (Ref. 12), and interactive inviscid/boundary layer method (Ref. 13)

have been utilized. However, the strong interaction between the viscous crossflow separation and the leeward vortex structure has precluded obtaining definitive computational results from these approximate methods. As a result, computational methods based on the Navier-Stokes equations appear to be required.

Recently [14], a numerical method based on the thin-layer form of the parabolized Navier-Stokes equations [15] was used to compute supersonic turbulent flow field surrounding ogive-cylinder and ogive-cylinder-boattail bodies at low and moderate angles of attack ($\alpha \leq 10^\circ$). Extensive comparisons indicated that the computed results were generally in good agreement with experimental measurements [16-18]. However, discrepancies between the computed and experimental results were seen in the regions of experimentally observed crossflow separation. The authors of [14] suggested as possible sources of these discrepancies between the computed and experimental results the lack of circumferential viscous terms within the thin-layer viscous model, and, more likely, inadequacies of the algebraic eddy-viscosity model to properly treat the regions of separated flow. (Another possible source of the discrepancies may have been the marginal computational resolution of the leeward-side vortex structures).

Degani and Schiff [19] improved the PNS code by adding the cross derivative and circumferential viscous terms to the original PNS code and modifies the algebraic eddy viscosity turbulence model to take into account regions of so called cross-flow separations. The above-mentioned sources of discrepancy were investigated. It was found that, given a computational grid which provides adequate spatial resolution of the leeward-side vortices, a rational modification of the eddy-viscosity turbulence model that is consistent with the physics of the flows extends the applicability of the method to flows having large regions of crossflow separation. The turbulence model, once modified, was used without further changes to compute the flows around an ogive-cylinder body and several cones at various angles of attack. The computed results were in uniformly good agreement with experimental measurements throughout the flow field, for all cases considered. ($\alpha \leq 22.6^\circ$).

As the first part of our investigation we assumed that the flow field is conical (but not necessarily symmetric). The validity of the assumption of locally conical viscous flow has been demonstrated in Ref. [14].

As a test case for the computations the experiments obtained by Bannik and Nebbeling [20] were chosen. In these experiments a cone of 7.5° half angle at Mach number 2.94 and Reynolds number 1.372×10^7 was tested up to 34° angle of attack. At high angle of attack nonconical asymmetric leeward side vortex patterns were observed. In the computation, using an earlier obtained solution of the above cone for angle of attack of 22.6° and at station $x=0.5$ as a starting solution, the angle of attack was gradually increased up to 34° . During this procedure the grid was carefully adjusted to capture the bow shock and to keep y^+ near the cone surface smaller than 5. A stable, converged symmetric solution was obtained.

Since the numerical code converged to a symmetric solution which is not the physical one, the stability was tested by a random perturbation at each point. The possible effect of surface roughness or non perfect body shape was investigated too. In all the cases that were investigated the changes in the converged solutions were of the order of the surface perturbation.

At this point of the investigation it was concluded that although the assumption of conical viscous flows can be very useful for certain cases, it can not be used for the present case and the full marching technique should be used (although Peake et al. [21] concluded in their paper that conical asymmetric vortex pattern is possible). Thus at the second part of the investigation an attempt to obtain a marching (in space) solution with the PNS method using the conical solution as an initial data was made, for the same cases.

Since the transition from symmetric to asymmetric pattern probably occurs near the tip of the cone the marching should be started very much near the tip and a new starting solution should be used instead of the one at $x = .5$ (for conical solutions as described above the location of the computed cross section does not matter), and therefore a new conical solution near the tip of the cone at $x=0.05$ is generated for angle of attack of 22.6° .

The solution that was obtained using the PNS method were very much alike the solution we got with the assumption of a conical flow field. Thus we test the stability of the solution to a random perturbation and the possible effect of the surface roughness as we did with the previous solution and again we got a similar behavior.

All these solutions were done using three different turbulent models. The first one is the simple algebraic eddy viscosity model, the second is a

modified algebraic eddy viscosity model and the third model was the one equation model (or kinetic energy equation model) which uses an additional partial differential equation to calculate the eddy viscosity coefficients. The model which is used in the present work was formulated by Rubesin [22] for compressible flows, based on the Glushko [23] model for incompressible flat plate boundary-layer flows.

For $\alpha \leq 20.6^\circ$ it was found that the use of the improved eddy viscosity model resulted with strong primary symmetric vortices, secondary vortices and simple eddy viscosity reattachment between them. For the case of $\alpha = 34^\circ$ the modified eddy viscosity model was used with the PNS code but the solution became unstable. The only solution which shows some improvement and was still stable obtained by relaxing the two models together. The results were not impressive since the eddy viscosity was probably an order of magnitude larger than it should be. The results using the one equation model didn't show any improvement as well.

At this point of the investigation it was concluded that although the PNS method code could be very useful for certain cases, it can not be used for the present case, of a large angle of attack. The natural step after the use of PNS code would be the solution of the full Navier Stokes Equations. Since the Navier Stokes Equations are parabolic in time the most common method to obtain a steady solution is by marching in time until convergence reached. To overcome the stability problem of the PNS solution we had to choose a method that does not suffer from this difficulty. The method of flux splitting and upwind spatial differencing for the convection terms in the streamwise direction has the advantage of having a natural numerical dissipation and better stability properties and therefore this method (24) was adopted.

Using the flux split method we have generated solutions for two test cases: The first was the case of the cone that was tested earlier with the PNS (but for laminar flow). The second test case for the computation was one of the experiments obtained by Lemont [7]. In the experiments an ogive-cylinder body of 3.5D nose and 7D afterbody, $Re = 200,000$ based on body diameter, and $\alpha = 40^\circ$ was chosen. We assumed that the solution is laminar. The solution was made in two steps. As a first step we used a grid of 59x50x60 free stream as initial condition and as a second step we used a grid of 59x50x120, where by linear interpolation we used the first step as an initial condition.

The second step was done in three paths. The first one was a time marching solution without any disturbance, the second was a solution with a perturbation at the nose (small jet perpendicular to the surface) at an angle of 90° to the plane of symmetry in the cross section. The third one

was a solution where small geometrical disturbance (2% of the diameter) was placed instead of the jet and at the same location.

During the investigation we had to give an answer for two questions. The first is, does the solution that we have generated, is the physical one or just a methastable solution that will not actually appear. The second question is, when we generate a solution using a method of time marching, do we reach the seady state solution ?

Thus a criterion to determine if the flow pattern will actually appear or will it be a steady state solution, is needed. We try to develop this criterion by using stability analysis. This is based on the assumption that solutions which are unstable to small disturbances can not be a steady state solution, and metastable solutions appear only for certain initial conditions.

Since the stability analysis is quite complicated and consumes a lot of computing time for the three dimension, compressible flow, we needed a simple test case where we have several solutions for the same boundary conditions. The case that was chosen was Jeffery Hammel flow in a diverging channel with large divergence angle [25]. (The case of large divergence angle, has not been examined for stability yet). Thus the goal of this part of the investigation is to develop stability criteria for an arbitrary α (where α is the angle between the walls).

In the stability analysis we limit ourselves to the analysis of linear stability of small disturbances such that the nonlinear terms in the disturbance equation are neglected. We study the disturbances that fulfill the same similarity condition as the base flow, meaning that the tangential distributions of velocity of both the distubance and the base flow, are independent of the streamwise direction. This assumption is equivalent to the case of wave-like disturbance of infinite wave-length in the streamwise direction. It was found that the only stable flow pattern is the one that an increase of the mass flow rate causes the downstream pressure to decrease.

2. The General Governing Equations (in body coordinates)

The general unsteady three-dimensional Navier-Stokes equations, written in strong conservation-law form, for Cartesian coordinates can be expressed in nondimensional variables as:

$$\frac{\partial \bar{q}}{\partial t} + \frac{\partial \bar{E}}{\partial x} + \frac{\partial \bar{F}}{\partial y} + \frac{\partial \bar{G}}{\partial z} = \frac{1}{Re} + \left(\frac{\partial \bar{Q}}{\partial x} + \frac{\partial \bar{R}}{\partial y} + \frac{\partial \bar{S}}{\partial z} \right) \quad (2.1)$$

The inviscid flux vectors in Eq. (2.1) are:

$$\begin{aligned} \bar{E} = E(q) &= \begin{bmatrix} \rho u \\ \rho u^2 + p \\ \rho uv \\ \rho uw \\ (e + p)u \end{bmatrix} & \bar{G} = G(q) &= \begin{bmatrix} \rho w \\ \rho w^2 + p \\ \rho vw \\ (e + p)w \end{bmatrix} \\ \bar{F} = F(q) &= \begin{bmatrix} \rho v \\ \rho v^2 + p \\ \rho vw \\ (e + p)v \end{bmatrix} & \bar{q} &= \begin{bmatrix} \rho \\ \rho u \\ \rho v \\ \rho w \\ e \end{bmatrix} \end{aligned} \quad (2.2)$$

The internal energy of the gas is defined in terms of the conservative variables as

$$e_i = (e/\rho) - 0.5(u^2 + v^2 + w^2) \quad (2.3)$$

while the equation of state for a perfect gas with ratio of specific heats γ is:

$$p/\rho = (\gamma - 1)e_i = a^2/\gamma \quad (2.4)$$

The viscous flux terms in Eq. (2.1) are:

$$\begin{aligned}
 \underline{\underline{Q}} = \underline{\underline{Q}}(q) = \begin{bmatrix} 0 \\ \tau_{xx} \\ \tau_{xy} \\ \tau_{xz} \\ Q_5 \end{bmatrix}, \quad \underline{\underline{R}} = \underline{\underline{R}}(q) = \begin{bmatrix} 0 \\ \tau_{yx} \\ \tau_{yy} \\ \tau_{yz} \\ R_5 \end{bmatrix}, \quad \underline{\underline{S}} = \underline{\underline{S}}(q) = \begin{bmatrix} 0 \\ \tau_{zx} \\ \tau_{zy} \\ \tau_{zz} \\ S_5 \end{bmatrix}
 \end{aligned}
 \tag{2.5}$$

where

$$(2.6)$$

In obtaining Eq. (1.6) the Stokes hypothesis was used: $\lambda = -2\mu/3$. In Eqs. (2.1)-(2.6) the Cartesian velocity components u, v, w are made nondimensional with respect to a_∞ (the freestream speed of sound), the density ρ is normalized by ρ_∞ and total energy e is referenced to $\rho_\infty a_\infty^2$.

We introduce a general transformation as follows:

$$\begin{aligned}
 \xi &= \xi(x, y, z, t) \\
 \eta &= \eta(x, y, z, t) \\
 \zeta &= \zeta(x, y, z, t)
 \end{aligned}
 \tag{2.7}$$

Subject to the transformation, Eq. (2.1) can still be expressed in a strong conservation-law form as:

$$\frac{\partial \hat{q}}{\partial t} + \frac{\partial \hat{E}}{\partial \xi} + \frac{\partial \hat{F}}{\partial \eta} + \frac{\partial \hat{G}}{\partial \zeta} = \frac{1}{Re} + \left(\frac{\partial \hat{Q}}{\partial \xi} + \frac{\partial \hat{R}}{\partial \eta} + \frac{\partial \hat{S}}{\partial \zeta} \right) \quad (2.8)$$

where

$$\begin{aligned} \hat{q} &= \bar{q}/J \\ \hat{E} &= (\xi_x \bar{E} + \xi_y \bar{F} + \xi_z \bar{G} + \xi_t \bar{q})/J \\ \hat{F} &= (\eta_x \bar{E} + \eta_y \bar{F} + \eta_z \bar{G} + \eta_t \bar{q})/J \\ \hat{G} &= (\zeta_x \bar{E} + \zeta_y \bar{F} + \zeta_z \bar{G} + \zeta_t \bar{q})/J \end{aligned} \quad (2.9)$$

and

$$\hat{Q} = \hat{Q}\xi(\bar{q}, \bar{q}_\xi) + \hat{Q}\eta(\bar{q}, \bar{q}_\eta) + \hat{Q}\zeta(\bar{q}, \bar{q}_\zeta) = (\xi_x \bar{Q} + \xi_y \bar{R} + \xi_z \bar{S})/J \quad (2.10)$$

$$\hat{R} = \hat{R}\xi(\bar{q}, \bar{q}_\xi) + \hat{R}\eta(\bar{q}, \bar{q}_\eta) + \hat{R}\zeta(\bar{q}, \bar{q}_\zeta) = (\eta_x \bar{Q} + \eta_y \bar{R} + \eta_z \bar{S})/J \quad (2.11)$$

$$\hat{S} = \hat{S}\xi(\bar{q}, \bar{q}_\xi) + \hat{S}\eta(\bar{q}, \bar{q}_\eta) + \hat{S}\zeta(\bar{q}, \bar{q}_\zeta) = (\zeta_x \bar{Q} + \zeta_y \bar{R} + \zeta_z \bar{S})/J \quad (2.12)$$

The Jacobian of the transformation, which appears in Eqs. (2.8)-(2.12), is defined as:

$$J^{-1} = x_\xi(y_\eta z_\zeta - z_\eta y_\zeta) + y_\xi(z_\eta x_\zeta - x_\eta z_\zeta) + z_\xi(x_\eta y_\zeta - y_\eta x_\zeta) \quad (2.13)$$

3. The P.N.S. Code

The P.N.S. code deals with the steady state solution. Thus the variables are independent of time. The parabolized Navier-Stokes equations are obtained from Eq. (2.1) by a generalized independent spatial variables that map the physical x, y, z space surrounding a body into a rectangular ξ, η, ζ computational region:

$$\begin{aligned}\xi &= \xi(x) &&= \text{streamwise (marching) coordinate,} \\ \eta &= \eta(x, y, z) &&= \text{spanwise or circumferential coordinate,} \\ \zeta &= \zeta(x, y, z) &&= \text{normal coordinate.}\end{aligned}$$

which maps the body surface into the $\zeta = 0$ plane, and by neglecting all streamwise derivative, $\partial/\partial\xi$, within the viscous terms, and by modifying the streamwise flux vector to permit stable time-like marching of the equations downstream from initial data. Following [15], we introduce the subsonic sublayer approximation, and the resulting parabolized Navier-Stokes equations can be written as:

$$\frac{\partial \hat{E}_S}{\partial \xi} + \frac{\partial \hat{F}}{\partial \eta} + \frac{\partial \hat{G}}{\partial \zeta} = \frac{1}{Re} \left[\frac{\partial}{\partial \eta} (\hat{R}\eta + \hat{R}\zeta) + \frac{\partial}{\partial \zeta} (\hat{S}\eta + \hat{S}\zeta) \right] \quad (3.1)$$

The modified streamwise flux vector in Eq. (2.1) is

$$\hat{E}_S = (\xi_x/J)E_S = (\xi_x/J) \begin{bmatrix} \rho u \\ \rho u^2 + p_S \\ \rho uv \\ \rho uw \\ (e+p_S)u \end{bmatrix} \quad (3.2)$$

where $p_S = p$ for supersonic flow, and p_S is defined from $\partial p / \partial \zeta = 0$ for subsonic flow in the viscous layer adjacent to the body surface. By evaluating p_S in this manner, Eq. (3.1) can be stably marched in the ξ direction for all flows where $u > 0$; that is, for flows without streamwise reversal (see [15] for associated stability analysis).

The viscous flux vectors in Eq. (2.1) R^η , R^ζ , S^η and S^ζ are given in the appendix.

3.1 Numerical Algorithm

The numerical algorithm used to march Eq. (3.1) downstream is an implicit, non-iterative, approximately factored finite-difference scheme, which is analogous to the one developed by Beam and Warming for the solution of the unsteady Navier-Stokes equations. The marching algorithm is derived in the same manner used by Schiff and Steger [15], but the viscous cross-derivative term $\partial \hat{R}^\zeta / \partial \eta$ $\partial \hat{S}^\eta / \partial \zeta$ in Eq. (3.1) cannot be treated implicitly, and, following Beam and Warming [26], are evaluated explicitly. The resulting algorithm can be written in so-called delta form as

$$\begin{aligned}
 & [\tilde{A}_s^j + (1-\alpha)\Delta\xi(\delta_\eta \tilde{B}^j - Re^{-1}\delta_\eta \tilde{N}^j)](\tilde{A}_s^j)^{-1} \\
 & * [\tilde{A}_s^j + (1-\alpha)\Delta\xi(\delta_\zeta \tilde{C}^j - Re^{-1}\delta_\zeta \tilde{M}^j)]\Delta\hat{q}^j \\
 & = (\tilde{A}_s^j - \tilde{A}_s^{j-1})\hat{q}^j + \alpha(\hat{E}_s^j - \hat{E}_s^{j-1}) - (1-\alpha)\Delta\xi\{\delta_\eta[\eta_x^{j+1}(\bar{E}/J)] + \\
 & + \eta_y^{j+1}(\bar{F}/J)] + \eta_z^{j+1}(\bar{G}/J)] + \delta_\zeta[\zeta_x^{j+1}(\bar{E}/J)] + \zeta_y^{j+1}(\bar{F}/J)] + \\
 & + \zeta_z^{j+1}(\bar{G}/J)] - Re^{-1}[\delta_\eta(\tilde{R}^\eta)^j + \delta_\eta(\tilde{R}^\zeta)^j + \delta_\zeta(\tilde{S}^\eta)^j + \\
 & + \delta_\zeta(\tilde{S}^\zeta)^j] - \theta Re^{-1}[\delta_\eta(\Delta\tilde{R}^\zeta)^{j-1} + \delta_\zeta(\Delta\tilde{S}^\eta)^{j-1}] - [(\zeta_x/J)^{j+1}\hat{E}_p^j \\
 & - (\xi_x/J)^j\hat{E}_p^{j-1}] + D\hat{q}^j + O(\Delta\xi)^{1+3\alpha}
 \end{aligned} \tag{3.3}$$

In Eq. (3.3) α is set equal to 0 for first-order accuracy (Euler implicit method) and $\alpha = 1/3$ for second-order accuracy (3-point backward differencing). Similarly, in the viscous terms $\theta = 0$ for first-order accuracy and $\theta = 1$ for second-order accuracy. The Jacobian matrices of the flux vectors, \tilde{A}_s , \tilde{B} , and \tilde{C} are obtained from local linearization [28] of \hat{E}_s , \hat{F} and \hat{G} . The Jacobian matrix \tilde{M} is obtained from local linearization

[28] of \hat{S}^{ζ} and, in an analogous manner, the Jacobian matrix \tilde{N} is obtained from linearization of \hat{R}^{η} . The symbol $\tilde{}$ indicates that the matrices are evaluated using flow variables q located at $j\Delta\xi$ and metric quantities at $(j + 1)\Delta\xi$. The term $D\hat{q}^j$ is a fourth-order explicit dissipation term, defined as:

$$D\hat{q}^j = \epsilon_e \tilde{A}^j_{s k 1} (1/J)^j [(\nabla_{\eta} \Delta_{\eta})^2 (J\hat{q})^j + (\nabla_{\zeta} \Delta_{\zeta})^2 (J\hat{q})^j] \quad (3.4)$$

which is added to the algorithm to suppress high-frequency oscillations. Linear stability analysis indicates that ϵ_e in Eq. (3.4) must be less than 1/16 to ensure stability of the algorithm. Although adding implicit smoothing terms within the operators on the left-hand side of Eq. (3.3) overcomes the linear stability limit and permits the use of larger values of ϵ_e , no such implicit smoothing was used. While the use of implicit smoothing tends to stabilize the numerical method, the added smoothing terms can be larger than the viscous terms of interest, and thus can degrade the accuracy of the solution.

Equation (3.3) contains all viscous terms and viscous cross terms applicable to the parabolized Navier-Stokes equations. The thin-layer viscous model form of the equations, previously used by Schiff and Steger [15] can be obtained by neglecting all viscous terms except those solely in the normal ζ direction. Thus, by dropping the terms \tilde{N} , \tilde{R} , \tilde{S}^{η} , $\Delta\tilde{R}^s$, and $\Delta\tilde{S}^{\eta}$ from Eq. (3.3), the thin-layer algorithm can be obtained.

4. The Conical Solution using the PNS Method

In general, the initial data for the marching method must be supplied from an auxiliary computation. However, when treating the flow over conical or pointed bodies this is not necessary. As outlined in [15], for inviscid flows about conical bodies a conical grid is selected and the flow variables are initially set to free-stream values. The solution is marched one step downstream from an initial station, and the resulting flow variables are then scaled to place the solution back at the original station. The process is repeated until no change in the variables is observed with further marching. The flow variables are then constant along rays of the flow field, and a conical solution has been generated. Upon assuming flow variables within the viscous layer to also be constant along rays, the same procedure can be used to generate viscous conical solutions. Although viscous flow cannot be strictly conical, the assumption that the flow variables are locally conical along rays is reasonable when treating high-Reynolds-number flows. The validity of the assumption of locally conical viscous flows has been demonstrated in [14]. The marching-stepback procedure was utilized to generate the conical solutions in the present work.

5. The Flux Split Scheme Applied to the Thin Layer Approximation.

The flux split method is a time marching method and thus the Eq. to be solved is Eq. (2.8), The thin-layer approximation means to neglect the viscous terms in the streamwise and the spanwise direction and keep only the viscous terms in the normal direction. Thus the Equation to be solved is:

$$\frac{\partial \hat{q}}{\partial t} + \frac{\partial \hat{E}}{\partial \xi} + \frac{\partial \hat{F}}{\partial \eta} + \frac{\partial \hat{G}}{\partial \zeta} = Re^{-1} \frac{\partial \hat{S}}{\partial \xi} \quad (5.1)$$

where \hat{S} now is:

$$\hat{S} = J^{-1} \begin{pmatrix} \mu(\zeta_x^2 + \zeta_y^2 + \zeta_z^2)u_\zeta + \mu/3 (\zeta_x u_\zeta + \zeta_y v_\zeta + \zeta_z w_\zeta) \zeta_x \\ \mu(\zeta_x^2 + \zeta_y^2 + \zeta_z^2)v_\zeta + \mu/3 (\zeta_x u_\zeta + \zeta_y v_\zeta + \zeta_z w_\zeta) \zeta_y \\ \mu(\zeta_x^2 + \zeta_y^2 + \zeta_z^2)w_\zeta + \mu/3 (\zeta_x u_\zeta + \zeta_y v_\zeta + \zeta_z w_\zeta) \zeta_z \\ \{(\zeta_x^2 + \zeta_y^2 + \zeta_z^2)[0.5\mu(u^2 + v^2 + w^2)_\zeta + \kappa Pr^{-1}(\gamma-1)^{-1}(\theta^2)_\zeta] + \\ + \mu/3 (\zeta_x u + \zeta_y v + \zeta_z w)(\zeta_x u_\zeta + \zeta_y v_\zeta + \zeta_z w_\zeta) \} \end{pmatrix} \quad (5.2)$$

5.1 Numerical Algorithm

The Split Flux method was developed to overcome the difficulty of stability. This goal could be achieved by combining two methods: The first is by using two steps factored scheme which was proved by Ying [28] to be unconditionally stable (differently from the three factored schemes), and the second is by splitting the Flux in ξ direction according to its eigenvalues. It was proved by Ying [28] that the stability of the scheme depend on the eigenvalues of the matrix \hat{E} . The splitting of \hat{E} is equivalent to adding a viscosity that stabilize the scheme.

The two steps implicit factored scheme with splitting of the \hat{E} flux for the thin layer approximation using the upwind approximation in the ξ direction and central differencing in the η and ζ direction can be written as follows:

$$\begin{aligned}
 & [I + h\delta_{\xi}^b(\hat{A}^+)^n + h\delta_{\zeta}^b\hat{C}^n - hRe^{-1}\delta_{\zeta}^{-1}\hat{M}^nJ - D_{i|\zeta}] \\
 & * [I + h\delta_{\xi}^f(\hat{A}^-)^n + h\delta_{\eta}^b\hat{B}^n - D_{i|\eta}] \Delta\hat{q}^n = \\
 & = -\Delta t\{\delta_{\xi}^b[(\hat{E}^+)^n - \hat{E}_{\infty}^+] + \delta_{\xi}^f[(\hat{E}^-)^n - \hat{E}_{\infty}^-] + \delta_{\eta}(\hat{F}^n - \hat{F}_{\infty}) + \\
 & + \delta_{\zeta}(\hat{G}^n - \hat{G}_{\infty}) - Re^{-1}\delta_{\zeta}(\hat{S}^n - \hat{S}_{\infty})\} - D_{\theta}(\hat{q}^n - \hat{q}_{\infty}) \tag{5.3}
 \end{aligned}$$

where $h = \theta\Delta t$. δ , δ_{ξ}^b , δ_{ξ}^f are central, backward and forward three points difference operator. \hat{A}^{\pm} , \hat{B} , \hat{C} , \hat{M} are obtained from the local linearization of \hat{E} , \hat{F} , \hat{G} , and \hat{S} . \hat{E}^{\pm} is the flux E which has been split into \hat{E}^+ and \hat{E}^- according to its eigenvalue in the following manner:

$$A = E = \begin{bmatrix} \epsilon_1(\lambda_1, \lambda_4, \lambda_5) \\ \epsilon_2(\lambda_1, \lambda_4, \lambda_5) \\ \epsilon_3(\lambda_1, \lambda_4, \lambda_5) \\ \epsilon_4(\lambda_1, \lambda_4, \lambda_5) \\ \epsilon_5(\lambda_1, \lambda_4, \lambda_5) \end{bmatrix} \tag{5.4}$$

and

$$\begin{aligned}
 E^{\pm} = \rho/2\gamma = & 2(\gamma-1)\lambda_1^{\pm} + \lambda_4^{\pm} + \lambda_5^{\pm} \\
 & 2(\gamma-1)\lambda_1^{\pm}u + \lambda_4^{\pm}U + \lambda_5^{\pm}U^- \\
 & 2(\gamma-1)\lambda_1^{\pm}v + \lambda_4^{\pm}V + \lambda_5^{\pm}V^- \\
 & 2(\gamma-1)\lambda_1^{\pm}w + \lambda_4^{\pm}W + \lambda_5^{\pm}W^- \\
 & 2\phi + \lambda_4^{\pm}/2 [(U^+)^2 + (V^+)^2 + (W^+)^2] + \lambda_4^{\pm}[(U^-)^2 + (V^-)^2 + \\
 & + (W^-)^2] + C_{III} \tag{5.5}
 \end{aligned}$$

$$C_{III} = \frac{(3-\gamma)(\lambda_4 + \lambda_5)c^2}{2(\gamma-1)}$$

and D_v and D_e are the numerical dissipation terms which are given as combination of second and fourth differences. The smooting terms have the following form:

$$D_{e|_{\eta}} = (\Delta t)J^{-1} \left\{ \epsilon_2 \bar{\delta} \rho(\hat{B}) \beta \bar{\delta} + \epsilon_4 \bar{\delta} \frac{\rho(\hat{B})}{1 + \beta} \bar{\delta}^3 \right\} |_{\eta} J$$

$$D_{v|_{\eta}} = (\Delta t)J^{-1} \left\{ \epsilon_2 \bar{\delta} \rho(\hat{B}) \beta \bar{\delta} + 2.5 \epsilon_4 \bar{\delta} \frac{\rho(\hat{B})}{1 + \beta} \bar{\delta} \right\} |_{\eta} J \quad (5.6)$$

where

$$\beta = \frac{|\bar{\delta}^2 p|}{|(1 + \delta^2) p|} \quad (5.7)$$

P is the nondimensional pressure and $\rho(\hat{B})$ is the spectral radius of \hat{B} .

6. Turbulence Models.

6.1 The Eddy-Viscosity Model

In this discussion we adopt the dimensional notation of Baldwin and Lomax [29]. The resulting coefficients can be nondimensionalized for use in Eq. (3.3) by normalizing them by their free-stream (laminar) values.

For laminar flow computations the coefficient of molecular viscosity $\mu = \mu_2$ is obtained from Sutherland's law and the coefficient of thermal conductivity κ is specified, assuming a constant Prandtl number, as $K_2/C_p = \mu L/Pr$. For turbulent-flow computations the laminar flow coefficients are replaced by

$$\mu = \mu_l + \mu_t$$

$$\kappa/C_p = \mu_l/Pr + \mu_t/Pr_t \quad (6.1)$$

The turbulent viscosity coefficient μ_t is computed using the isotropic, two-layer, Cebeci-type, algebraic eddy-viscosity model reported by Baldwin and Lomax [29].

In the Baldwin-Lomax formulation μ_t is given by

$$\mu_t = \begin{cases} (\mu_t)_{\text{inner}} & , \quad y \leq y_c \\ (\mu_t)_{\text{outer}} & , \quad y > y_c \end{cases} \quad (6.2)$$

where y is the local distance measured normal to the body surface and y_c is the smallest value of y at which the values from the inner and outer region formulas are equal. Within the inner region

$$(\mu_t)_{\text{inner}} = \rho \ell^2 |\omega| \quad (6.3)$$

where

$$\ell = ky [1 - e^{-(y^+/A^+)}] \quad (6.4)$$

$|\omega|$ is the magnitude of the local vorticity vector, and

$$y^+ = \sqrt{\rho \tau_w / \mu_w} y \quad (6.3)$$

In the outer region, for attached boundary layers the turbulent viscosity coefficient is given by

$$(\mu_t)_{\text{outer}} = K C_{cp} \rho F_{\text{wake}} F_{\text{kleb}}(y) \quad (6.6)$$

In Eq. (6.6) K and C_{cp} are constants, F_{kleb} is the Klebanoff intermittency factor, and

$$F_{wake} = y_{max} F_{max} \tag{6.7}$$

where F_{max} is the maximum value that the function $F(y)$, defined as

$$F(y) = |\omega| y [1 - e^{-(y^+/A^+)}] \tag{6.8}$$

takes in a local profile, and y_{max} is the value of y at which F_{max} occurs. The constants appearing in Eqs. (6.1)-(6.8) were determined in [29] by requiring the boundary-layer profiles computed with the model to be in agreement with those determined using the Cebeci [30] formulation. The values were determined to be

$$\begin{aligned} Pr &= 0.72, & k &= 0.4, \\ Pr_t &= 0.9, & K &= 0.01681, \\ A^+ &= 26, & C_{cp} &= 1.6. \end{aligned} \tag{6.9}$$

6.2 Modified Addy Viscosity Model

The major difficulty encountered in applying the Baldwin-Lomax turbulence model to bodies with crossflow separation is that of properly evaluating the scale length y_{max} and in turn, of determining $(\mu_t)_{outer}$ for boundary-layer profiles in the crossflow separation region. This difficulty becomes apparent upon considering the behavior of the function $F(y)$ [Eq.(6.8)] along two rays, one located on the windward side at $\phi = \phi_1$

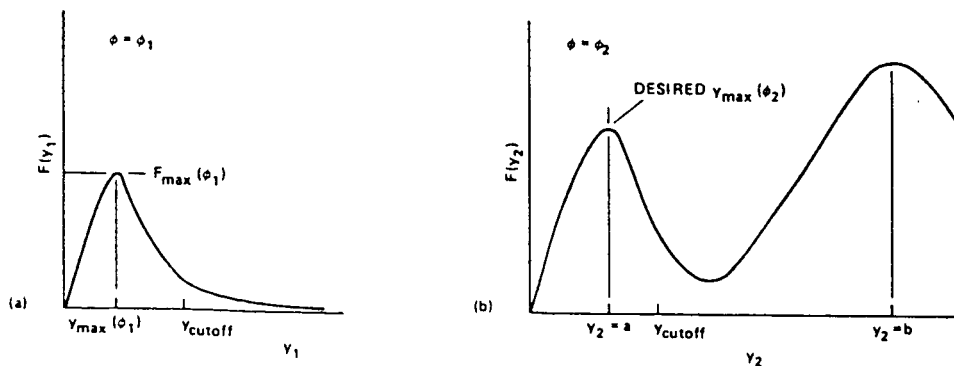


Fig. 6.1 Behavior of $F(y)$ at large incidence, (a) $\phi = \phi_1$ (windward side), (b) $\phi = \phi_2$ (leeward side).

and the other on the leeward side at $\phi = \phi_2$. The functions are shown schematically in Figs. 6.1(a) and (b), respectively. On the windward side the attached boundary layer gives rise to a profile of $F(y)$ which has a single, well-defined, peak, as shown in Fig. 6(a). Thus, the determination of $F_{\max}(\phi_1)$, $y_{\max}(\phi_1)$, and $F_{\text{wake}}(\phi_1)$ is straightforward. However, on the leeward-side ray [Fig. 6.1(b)], in addition to a local peak in $F(y)$ in the attached boundary layer at $y_2 = a$, the overlying vortex structure causes a larger peak in $F(y)$ at $y_2 = b$. As originally implemented, the computer code searches outward along each ray to determine the maximum in $F(y)$, and would, in this instance, select the peak in $F(y_2)$ occurring at $y_2 = b$. The choice of the peak at $y_2 = b$ results in a value of $F_{\text{wake}}(\phi_2)$ and, in turn, a value of the outer layer eddy-viscosity coefficient $(\mu_t)_{\text{outer}}$ which is much too high. The resulting value is at least one order of magnitude larger and can be as much as two orders of magnitude larger than the value of $(\mu_t)_{\text{outer}}$ resulting from evaluating $F_{\text{wake}}(\phi_2)$ from the peak at $y_2 = a$. Thus, in general, the computed eddy-viscosity coefficient in the crossflow separation region behind the primary separation point will be too high. This will cause the details of the computed flow to be distorted or washed out. In particular, the primary vortices will be smaller than those observed experimentally and the primary separation point will be located closer to the leeward symmetry plane. In addition, the secondary separation and secondary vortices will not appear in the computed flow.

To eliminate these difficulties we have modified our implementation of the turbulence model. At each axial station the code searches radially along successive rays, sweeping from the windward to the leeward plane of symmetry. Along each ray the code sweeps outward to find the first peak in $F(y)$, and cuts off the search when the peak is reached. To prevent the selection of extraneous peaks which might be caused by a nonsmooth behavior in $F(y)$, a peak is considered to have been found when the value of $F(y)$ drops to 90% of the local maximum value. Choice of F_{\max} in this manner will exclude the second, spurious, maximum [see Fig. 6.1(b)].

For most rays in the crossflow separation region the two peaks in $F(y)$ are spaced far enough apart that the logic described above will select the first peak. However, this is not true for rays in the vicinity of the primary

separation point (and to a lesser extent for rays in the immediate vicinity of the secondary separation point). Along these rays the vortex feeding sheets lie close to the outer edge of the attached boundary layers: the peaks in $F(y)$ merge. Under these conditions the code would choose a value of y_{max} near the top edge of the feeding sheet. Consequently, a further test is applied. On each ray (except the ray on the windward plane of symmetry) a cutoff distance is specified in terms of y_{max} from the previous ray, i.e., $y_{cutoff}(\phi) = cy_{max} (\phi - \Delta\phi)$, where c is a constant chosen equal to 1.5. If no peak in $F(y)$ is found along a ray for $y \leq y_{cutoff}$ the values of F_{max} and y_{max} are taken as those found on the previous ray. In this manner a physically reasonable value of the eddy-viscosity coefficient will be chosen for those rays close to the crossflow separation points.

It is readily apparent that conditions within the boundary layers which leave the body at the primary separation points are related to the conditions within the boundary layers on the windward side of the body. Further, it is physically reasonable to expect that the boundary-layer quantities vary smoothly circumferentially around the body. Thus, specifying the cutoff distance in terms of the values on the previous ray, and taking the values of y_{max} and F_{max} from those of the adjacent ray, allows the model to be applicable in a rational manner over a wide range of local flow conditions, and in particular, for varying local Reynolds numbers.

The various coefficients appearing in the Baldwin-Lomax turbulence model were varied to assess their effect on the computed boundary-layer profiles. The best match with experimental measurements was obtained with the coefficients set at the values suggested in Eq. (6.9).

6.3 One Equation Model.

This model has one turbulence source function H_k :

$$H_k = \mu_t S^2 - 2\rho k D/3 - C\mu_k k/L^2 \quad (6.10)$$

where

$$S^2 = (u_y + v_x)^2 + 2[u_x^2 + v_y^2 + (v/r)^2] - 2D^2/3$$

$$D = u_x + v_y + v/r$$

$$\mu_t = \alpha\mu_t R_t H(R_t/R_0)$$

$$R_t = \rho \sqrt{k} L/\mu_t$$

$$H(R) = \begin{cases} R & \text{for } R < 0.75 \\ R - (R-0.75)^2 & \text{for } 0.75 \leq R \leq 1.25 \\ 1 & \text{for } 1.25 < R \end{cases} \quad (6.11)$$

$$\alpha = 0.2, \quad C = 3.93, \quad R_0 = 110, \quad P_{rk} = 2.5$$

Here k is the turbulence kinetic energy, $k = \rho \overline{U_i' U_i'}/2\rho$, and L is the length scale as specified by Glushko [23]:

$$L/\delta = \begin{cases} y/\delta & \text{for } 0 \leq y/\delta < 0.23 \\ (y/\delta + 0.37)/2.61 & \text{for } 0.23 \leq y/\delta \leq 0.57 \\ (1.48 - y/\delta)/2.52 & \text{for } 0.57 \leq y/\delta \leq 1.48 \end{cases} \quad (6.12)$$

The total kinetic energy diffusivity μ_k is given by:

$$\mu_k = \mu_l + \mu_t / Pr_k \quad (6.13)$$

The total viscosity μ and the thermal energy diffusivity are

$$\mu = \mu_l + \mu_t$$

$$K/C_p = \mu_l / Pr + \mu_t / Pr_t \quad (6.14)$$

7. The Test Case for the Stability Criterion.

The test case that was chosen is the Jeffery Hammel flow in a divergent channel since for that case we have an analytic solution which provides two different patterns of flow for the same boundary conditions.

7.1 The flow field

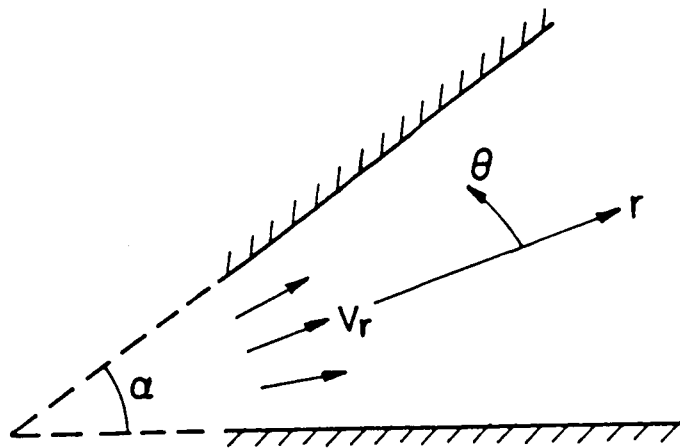


Fig. 7.1 - Configuration of the problem.

Statement of the problem.

We study a divergent channel, infinite in the z direction (Fig. 7.1) in cylindrical coordinates, r , θ , z . $r=0$ is the (virtual) intersection of the two walls. A Newtonian, viscous incompressible fluid flows in the channel as a result of inertia forces or an external pressure gradient which is a function of r and θ . We assume that the flow is isothermal and has only a radial component V_r . Thus

$$V_z = V_\theta = 0 \quad \text{everywhere in the flow} \quad (7.1)$$

where V_z and V_θ are the velocity components in the θ and z directions respectively.

The boundary conditions are the no-slip conditions:

$$V_r = 0 \quad \text{at the walls} \quad (7.2)$$

where V_r is the velocity component in the r direction.

We consider the mass flow rate or the pressure gradient at the walls as given (compatibility condition).

By defining nondimensional velocity and time as:

$$U \equiv V_r / U_{\max} \quad (7.3)$$

$$\tau \equiv t \frac{U_{\max}}{r} \quad (7.4)$$

we obtain a Re number:

$$Re = U_{\max} r / \nu \quad (7.5)$$

From the incompressible Navier-Stokes equation we get the time dependent equation for the flow field:

$$Re \left(\frac{\partial U}{\partial t} \right) = \left(\frac{\partial^2 U}{\partial \theta^2} \right) + 4U + ReU^2 + K \quad (7.6)$$

where

$$K = K(t) = -c(t)/Re = - \left. \frac{\partial^2 U}{\partial \theta^2} \right|_{\text{walls}} \quad (7.7)$$

The pressure equation is

$$P = P_0(\theta, t) + 2\rho \text{Re}U + K\text{Re} (\rho\nu^2/2r^2) \quad (7.8)$$

and the pressure gradient along the walls $(\partial p/\partial r)_W$, is:

$$(\partial p/\partial r)_W = (-K \text{Re}) \rho\nu/r \quad (7.9)$$

The mass flow rate M , for a unit depth of the channel is:

$$M = \text{Re}\mu \int_{\alpha} U d\theta \quad (7.10)$$

where μ is the dynamic viscosity.

7.2 Solution for the Steady State Flow Field.

The solution for this case was presented by Shapira, Degani and Weiss [25] as follows:

$$U' = \pm \sqrt{(2\text{Re}/3) (1-U) (\beta_2 - U) (\beta_3 - U)} \quad (7.11)$$

where

$$\begin{aligned} \beta_2 &= a + d \\ \beta_3 &= a - d \end{aligned} \quad (7.12)$$

and

$$a = -(3/Re + 1/2)$$

$$d = 1/(2Re) \sqrt{3[12 - Re(4k + Re + 4)]} \quad (7.13)$$

7.2.1 The steady state solution for $-(Re+6)/3 < k < -Re/4 + 3/Re - 1$ is:

The solution in the above range is given by:

$$U = 1 - (1-\beta_2) \operatorname{Sn}^2(\theta/\lambda_1, k_1) \quad (7.14)$$

where

$$k_1^2 = \frac{1 - \beta_2}{1 - \beta_3} \quad \lambda_1^2 = \frac{6}{Re(1-\beta_3)}$$

and $\operatorname{Sn}(\theta/\lambda_1, k_1)$ is the Jacobian elliptic function of the first kind, and

$$\theta = \lambda_1 \int_0^{\xi} \frac{d\xi}{(1-k_1^2 \sin^2 \xi)^{1/2}} = \lambda_1 F(\xi, k_1) \quad (7.15)$$

For the channel angle α and the corresponding mass flow rate we can get a number of solutions which fulfill one of the following rules:

$$\alpha = 2(n \alpha_1 + (n-1) \alpha_2) \quad ; \quad M = 2(n M_1 + (n-1) M_2)$$

or

$$\alpha = 2(n \alpha_1 + n \alpha_2) \quad ; \quad M = 2(n M_1 + n M_2)$$

or

$$\alpha = 2(n \alpha_1 + (n+1) \alpha_2) \quad ; \quad M = 2(n M_1 + (n+1) M_2) \quad (7.16)$$

where $n = 1, 2, \dots$, and $\alpha < \pi$.

and

$$\alpha_1 = \lambda_1 \int_0^{\xi_1} \frac{d\xi}{(1-k_1^2 \sin^2 \xi)^{1/2}} = \lambda_1 F(\xi, k_1) \quad (7.17)$$

where $F(\xi_1, k_1)$ is the incomplete elliptic function of the first kind. The mass flow rate passing through this element is:

$$M_1 = \frac{Re\mu}{k_1^2} [(k_1^2 - 1 + \beta_2)\alpha_1 + \lambda_1(1-\beta_2) E(\xi_1, k_1)] \quad (7.18)$$

where $E(\xi_1, k_1)$ is the incomplete elliptic function of the second kind.

The angle of the element $0 > U > \beta_2$ is:

$$\alpha_2 = \int_{\xi_1}^{\pi/2} \frac{d\xi}{(1-k_1^2 \sin^2 \xi)^{1/2}} = \lambda_1 F(k_1) - \alpha_1 \quad (7.19)$$

where $F(k_1)$ is the complete elliptic function of the first kind. The mass flow rate passing through this element is:

$$M_2 = M_1 - \frac{Re\mu}{k_1^2} [(k_1^2 - 1 + \beta_2) F(k_1) + (1-\beta_2) E(k_1)] \quad (7.20)$$

where $E(k_1)$ is the complete elliptic function of the second kind, and

$$\xi_1 = \arcsin(\sqrt{T/(1-\beta_2)}) \quad (7.21)$$

7.2.2 The steady state solution for $k > -Re/4 + 3/Re + 1$

The solution in the above range is given by :

$$U = 1 - L(1 - \text{Cn}(\theta/\lambda_2, k_2)) / (1 + \text{Cn}(\theta/\lambda_2, k_2)) \quad (7.22)$$

where

$$L^2 = 3(K + Re + 4) / Re \quad (7.23)$$

and

$$\lambda_2^2 = 3 / (2 Re L)$$

$$k_2^2 = (L + 3/Re + 3/2) / (2 L) \quad (7.24)$$

and $\text{Cn}(\theta/\lambda_2, k_2)$ in the Jacobian elliptic function of the second kind

$$\theta = \lambda_2 \int_0^{\xi} \frac{d\xi}{(1 - k_2^2 \sin^2 \xi)^{1/2}} = \lambda_2 F(\xi, k_2) \quad (7.25)$$

The half of the channel angle is:

$$\alpha/2 = \lambda_2 \int_0^{\xi_2} \frac{d\xi}{(1-k_2^2 \sin^2 \xi)^{1/2}} = \lambda_2 F(\xi_2, k_2) \quad (7.26)$$

The mass flow rate is:

$$M = \text{Re}\mu [(1-L)\alpha + 4L\lambda_2 (E(\xi_2, k_1) - L2)] \quad (7.27)$$

where

$$L2 = \sqrt{L(L-4L k_2 + 2L + 1) / [L(L+1)]} \quad (7.28)$$

and

$$\xi_2 = \arccos ((L-1) / (L+1)) \quad (7.29)$$

7.3 The stability equation.

Next we examine the linear stability of the flow patterns subject to perturbations that vary as $1/r$ and are functions of θ and t .

Let us define a nondimensional solution:

$$U(\theta, t) = U_0(\theta) + W(\theta, t) \quad (7.30)$$

which was obtained by multiplying the solutions of the previous section by r , where U_0 is the base flow that is analyzed for stability, and W is the perturbation.

Substituting Eq. (7.30) in Eq. (7.6), subtracting eq. (7.6) (written for U_0) and neglecting the nonlinear terms yields the following linear equation for small disturbances:

$$\partial W / \partial t = (W'' + 4W) / \text{Re} + 2U_0 W \quad (7.31)$$

Let us define a disturbance of the type:

$$W(\theta, t) = W(\theta) \exp(\beta t) \quad (7.32)$$

From Eq. (6.3) we obtain:

$$(4/Re + 2U_0)W + W''/Re - W = 0 \quad (7.33)$$

With the following boundary conditions:

$$W = 0 \quad \text{at the walls} \quad (7.34)$$

Eq. (7.33) and the boundary conditions (7.34) are a system of eigenvalues β and eigenfunctions $W(\theta)$.

The base flow pattern is stable if:

$$\beta < 0. \quad (7.35)$$

for all the eigenvalues of Eq. (6.33) with the boundary conditions (7.34)

Solution of the stability equation by a finite difference scheme.

Let us define the following approximation:

$$W_n = \frac{W_{n-1} + W_{n+1} - 2W_n}{h^2} \quad n = 0, 1, \dots, N \quad (7.36)$$

where h is the difference between two discrete points and W_n is the value of W at $\theta = n \cdot h$.

8. Results and Discussion

8.1 The Stability Analysis

8.1.1 Decreasing pressure in the downstream direction.

In the case where the pressure decrease is in the flow direction two counteracting mechanisms exist: The first is the pressure gradient that tries to accelerate the flow. The second is the deceleration and accompanying pressure rise due to the radial spreading of the flow.

In Fig. 1 contours of constant α are plotted in the plane of M (the mass flow rate) vs. $(\partial p/\partial r)_w$ (the pressure gradient on the walls). As a result of the two opposing mechanisms mentioned above there is a critical value of the mass flow rate M_c for each α that behaves in the following manner: For $M < M_c$ an increase in the mass flow rate, will cause the downstream pressure to decrease. When $M > M_c$ an increase in the mass flow rate, will cause the downstream to increase.

Another result that can be deduced from Fig. 1 is: For any pressure gradient on the walls $(\partial p/\partial r)_w$, we can find two values of mass flow rate M . One is greater than M_c and one is smaller.

Curves of M_c are depicted in Fig. 1 and Fig. 4. The accompanying K and $(\partial p/\partial r)_w$ are given in Fig. 6 and Fig. 3.

The stability method, described in Paragraph 7, leads us to the following conclusion: When $M > M_c$ the flow is unstable, and when $M < M_c$ the flow is stable, but when $M > M_c$, the mechanism that limitss and stabilizes the flow, is missing.

We also see from Fig. 1 that for any α the pressure gradient and the mass flow rate M are bounded. In Fig. 3, we see the line that separates the zone of two solutions and the zone where no solution of the type $V_{\theta} = 0$ exists. Fig. 2 depicts graphs of pressure gradients vs. α for constant Re . We see that each curve ascends to the contour depicted in Fig. 3 becomes tangent to it, and then returns back into the two solutions range. From the stability analysis we found that the solution is unstable in the range of ascent and stable afterwards.

In Fig. 4, zones of existence of the solutions and their stability are depicted. For any α there is a stable zone of low mass flow rate, an unstable zone of higher mass flow rate, and a zone where no solution of the type $V = 0$ exists.

In Fig. 5 contours of constant α are plotted for α between 5° and 60° . From Fig. 5 we see that the contours of constant α are slightly convex. Thus for any given α it is possible to find two constants which approximate the relation between K and M . In order to approximate the velocity profile, using these three constants, the Re number is needed. In Fig. 6 contours of constant Re in the α vs. K plane are given. From Fig. 6 and Eq. (7.14) or Eq. (7.22) the pressure gradient and the velocity profile can be calculated.

In Fig. 6 the stability line in the K vs. α plane is depicted, so that below this line the solution is unstable, and stable above it.

8.1.2 Pressure gradient in the upstream direction.

In the case where the pressure decreases in the upstream direction three patterns of flow can be defined (as expressed in Eq. (7.16)): The first is a symmetric pattern of flow without inverse flow near the walls (positive shear stress on both walls). The second is an asymmetric pattern of flow with an inverse flow near one wall (positive shear stress on one wall and negative shear stress on the other). The third is a symmetric flow pattern with an inverse flow near both walls (negative shear stress on the two walls).

It is obvious that for any pattern we can find several zones of negative and positive velocity that obey the rules appearing in Eq. (7.16). As mentioned in Paragraph 7 when $K = K_p$, the range of inverse flow is reduced and the three patterns of flow become the same.

In Fig. 7 curves of constant α are plotted in the plane of M (mass flow rate) vs. $(\partial p / \partial r)_w$ (the pressure gradient on the walls), for the case where only one range of positive velocity exists. In this case, for any α we have three branches with a common point at $K = K_p$. The left branch is for the case without inverse flow, the centre branch for inverse flow near one wall and the right branch describes the case with inverse flow near both walls. The left branches are the continuation of the curves obtained when the pressure decreases in the downstream direction.

From Fig. 7 we conclude that the contours are qualitatively similar for the full range of α . Fig. 8 shows curves of $\alpha = 20^\circ$ in the plane of $(\partial p / \partial r)_w$ vs. M , for single double and triple positive velocity zones.

From Fig. 7 and Fig. 8 we also conclude that in the case of the velocity profile without an inverse flow (left branches in Fig. 7) the solution is unique. In patterns of flows where zones of negative velocity appear, for every pressure gradient we have at least two solutions for the mass flow rate. Fig. 9 describes the zones where one solution and multiple solutions exist, in the plane of α vs. $(\partial p / \partial r)_w$.

In Fig. 7, we see that for pressure decreasing in the upstream direction we can have higher mass flow rate than we had in the case of pressure decreasing in the downstream direction. From Fig. 7 and Fig. 8 we understand that it is possible to define the ranges of mass flow rate and the range of pressure gradient for each flow pattern. Beyond these range this pattern cannot exist (similar to Fig. 9).

From the stability analysis we found that all the patterns of flow where the pressure gradient is in the upstream direction are unstable. We found that there are cases where the pressure gradient is in the upstream direction and increasing the pressure gradient causes an increase in the mass flow rate. Analysis based on physical reasoning could lead us to the conclusion that these patterns are stable. The stability method, described in Paragraph 7, shows however that the flow is unstable. This instability can be explained by the combinations of unstable elements. The instability expresses itself in the fact that, in such elements a decrease in the mass flow rate causes an increase in the pressure gradient.

8.2 Conical Solution

The Schiff-Steger PNS code [aa] has been modified to allow computation of conical flowfields around cones at high incidence. The improved algorithm of Degani and Schiff [aa] has been incorporated with the PNS code. This algorithm adds the cross derivative and circumferential viscous terms to the original PNS code and modifies the algebraic eddy viscosity turbulence model to take into account regions of so call cross-flow separation. Assuming the flowfield is conical (but not necessarily symmetric) a marching stepback procedure is used: the solution is marched one step downstream using improved PNS code and the flow variables are then scaled to place the solution back to the original station. The process is repeated until no change in the flow variables is observed with further marching. The flow variables are then constant along rays of the flowfield. The experiments obtained by Bannik and Nebbeling [20] were chosen as a test case. In this experiments a cone of 7.5° half angle at Mach number 2.94 and Reynolds number 1.372×10^7 was tested up 34° angle of attack. At High angle of attack nonconical asymmetric leeward side vortex patterns were observed. In the first set of computations, using an earlier obtained solution of the above cone for angle of attack of 22.6° and at station $x=0.5$ as a starting solution, the angle of attack was gradually increases up to 34° . During this procedure the grid was carefully adjusted to capture the bow shock and to keep y^+ near the cone surface smaller then 5. A Stable, converged symmetric solution was obtained. It was the first time that a numerical solution was obtained for an angle-of-attack-to-half-cone-angle ratio as high as this case.

Since the numerical code is perfectly symmetric, in the second set of computations a random perturbation of about 1% of the local flowfield variables was introduced at each point of the flowfield and the marching stepback procedure was continued till a new converged solution was obtained. It was found that in all cases tested the solution converged back to the original symmetric solution. By increasing the initial perturbation above 2% - 5% of the local flowfield variables the numerical solution became unstable and did not converge.

In the third set of numerical experiments the possible effect of surface roughness or non perfect body shape was investigated. The cross section of the cone has been changed randomly up to 1% of the original diameter and kept so until a new converged solution was obtained using the marching stepback procedure. It was found that in all cases investigated the changes in the converged solutions were of the order of the surface perturbation.

8.3 Marching Solution

8.3.1 Algebraic Turbulence Model

As mentioned earlier, Bannik and Nebbeling [20] found in their experiments that at high angle of attack a nonconical asymmetric vortex pattern is obtained. Therefore, for these cases the full marching technique should be used. Moreover, since the transition from symmetric to asymmetric pattern probably occurs near the tip of the cone, a new starting solution should be generated instead of the one at $x=0.5$ (which was used for the conical solutions). A new conical solution near tip of the cone at $x=0.05$ was generated for angle of attack of 22.6° . Figs. 10-11 show results with the old algebraic turbulence model and Figs. 12-13 show results using the modified algebraic model. From the velocity vector plots one can see that the use of the modified model resulted with strong primary symmetric vortices and secondary ones. The results of the old model show just one weak pair of primary vortices. Using these results another conical solution for angle of attack of 34° at $x=0.05$ was generated. Figs. 14-15 show the results for this case using the old turbulence model. At this point the modified algebraic model was introduced but the solution became unstable. The only solution which showed some improvement in comparison to the solution obtained with the old turbulence model and was still stable obtained by relaxing the two models together. A solution which obtained using a ratio of 90% of the value of eddy viscosity from the improved model and 10% of from the old model is shown in Figs. 16-17. The results are not impressive and one has to remember that although the ratio is 9:1 the eddy viscosity is probably still too high.

8.3.2 One Equation Turbulence Model

For flowfield where the mean flow changes so rapidly that the turbulence cannot remain in equilibrium with mean motion, an algebraic model might not be sufficient. In cases where the region of separation is relatively small compare to the upstream boundary layer thickness a one equation turbulence model can be used (see paragraph 6.3). Although the use of this model improved the simulation of separated flows in some cases (see for example Ref. [31]), it did not improve the unstable behaviour of our 34° angle of attack case.

8.3.3 Asymmetric solution for $\alpha=34^\circ$

Using the combined old and modified turbulence models, as mentioned

above, an asymmetric solution was obtained by perturbing the initial flowfield. Starting with a conical (symmetric) solution near the tip of the body, the PNS code was used to march down the body at 34° angle of attack. During the first ten steps a small perturbation of about 1% of the local value of the symmetric solution was added in random. Figure 18 shows the density contours at different stations down the body and Figure 19 shows the velocity vectors for the same stations.

The results shows large asymmetry of the solution (And it is much larger than the initial perturbation) and the primary vortices are not straight or parallel to the leeward plane of symmetry. These results are qualitatively similar to Bannik and Nebbeling experiments [20].

The solution for $k=144$ points (circumferentially) was unstable for all turbulence models.

8.4 Navier-Stokes Simulation

Computation were carried out using the NAS CRAY-2 computer, for an ogive-cylinder body of revolution, having a 3.5 caliber nose and a 7 caliber cylindrical afterbody, at a freestream Mach number of 0.2, a Reynolds number of 200,000 based on the body diameter, and an angle of attack of 40° . This body geometry and test conditions correspond to those of an experimental study carried out by Lamont [6,7] in the NASA Ames 12-foot Pressure Wind Tunnel, in which surface pressure measurements were obtained. Recent analysis of the data, carried out by Hall [32], showed that for this laminar flow condition a wide variety of side force values could be obtained, depending on the orientation which the (nominally axisymmetric) body had in the wind tunnel.

The computational grid (which is shown in Figure 20), consisted of 59 points in the axial direction, 120 points circumscribing the body in the circumferential direction, and 50 radial points. In the computations the flow was assumed to be laminar; that is, no turbulence model was employed, and the viscosity coefficients were obtained using Sutherland's viscosity law and the Stokes hypothesis.

Three cases have been computed, all at $\alpha = 40^\circ$. In the first, the flow was set to free-stream conditions throughout the computational mesh, and the solution advanced in time. After an initial transient, the computed flow was found to evolve to a time-periodic, symmetric state. The second case was identical to the first, except that a very small jet was introduced into the computation on one side of the body to break the symmetry of the solution. The jet was located axially about half length of the ogive nose, and was located circumferentially 90° from the angle of attack plane. In the third case a small geometrical disturbance (about 2% of the body diameter) was added to the body at the same location as the jet. In the

second case the solution again evolved to a time periodic state, but the solution was asymmetric.

Figs. 21-23 are sample results for the symmetric computation of the second case. Figure 21 presents density contours in crossflow planes normal to axis of the body. The position of the vortex cores are indicated by the regions of low density, shown by the closed contours. Although the computational region extends circumferentially completely around the body, in this case the flow was found to be symmetric about the angle of attack plane, and thus contours for only one half of the flowfield are shown. One main vortex (pair) is visible about the leeward side. In addition, a smaller vortices are seen in the figure, originating near the flanks of the body on the leeward side. These small vortices are seen to move upwards from the body surface with increasing time, and to merge with the main vortex pair. As this occurs, Additional small vortices are observed to form at the flanks (below the upward moving vortices). This cycle continues, and has a definite periodic frequency.

Time histories of normal force and pitching-moment coefficients (moments taken about the nose) are shown in Figs. 22 and 23, respectively. These show part of the initial transient, and the eventual evolution of the solution to a periodic stat. The period of the force and moment history corresponds to the time between the generation of successive small vortices at the flanks of the body. The occurrence of the time periodic solution is extrimely intriguing. At present we believe that this phenomenon is akin to the shear-layer instability observed by Payne et al. [33] and Blackwelder and Gad-el-Hak [34] in experimental investigations of the flow about delta wings at low Reynolds numbers. As such, it may indicate that Navier-Stokes computations, using reasonable grid resolution, may permit direct computations of flow instabilities and initial transition to turbulence for flow about complete configutrations. Additional numerical investigation of this phenomena is underway.

The corresponding results for the asymmetric cases are shown in Figs. 24-30. Figure 24 shows color contours of density in crossflow planes normal to the axis of the body. The position of the vortex cores are indicated by the regions of low density (denoted by reds and yellows). Dark blue contours denote densities approaching free-stream density. At least four major vortices are visible, which shed from the body and extend into the leeward-side flow. The first leaves the near side of the body at the ogive -cylinder junction, as indicated by the change in the vortex core density from red to green to blue in this region. A second vortex leaves the far side of the body mid-way down the cylinder, while a third leaves the near side of the body at the rear of the cylinder. A fourth major vortex exists on the far side of the cylinder, but it cannot be seen in this figure,

since it lies behind the near-side vortex. In addition to the four main vortices, small-scale vortices, similar to those observed in the symmetric case, are visible.

Figure 25 shows particle traces for the same flowfield, and confirms the presence of multiple vortices. The particles emanating from the near side of the body are colored blue, while those from the far side are red. The vortices are seen to extend downstream over the entire body from their point of origin.

Time histories of the normal force, pitching moment, and yawing moment coefficients (moments taken about the nose) are shown in Figs. 26-28 respectively. As was presented for the symmetric case, these figures show part of the initial transient, and the evolution to a periodic state. The mean values of the normal force and pitching moment coefficients are close to those obtained for the symmetric case. However, yawing moment coefficient is seen to undergo a periodic variation about a non zero value, at the same frequency of the variation in the pitching moment coefficient. In contrast, in the symmetric case the yawing moment coefficient was zero at all times, since the solution, although unsteady, was always symmetric. Comparison of side forces acting on the body for the asymmetric case, with the net side forces caused by the jet alone, showed that the latter are only 6% of total side forces. This indicates that the jet merely breaks the symmetry of the solution.

Figs. 29-30 show density contours in crossflow planes normal to the axis of the body for the third case, where a small geometrical disturbance had added to the body. Although the solution has not been converged yet to a periodic state as in the above case, and these results are part of the initial transient, it is clear that the solution has been becoming asymmetric. We believe that this asymmetric flowfield will be converged to a non-symmetric periodic state similar to the one obtained when the symmetry of the solution was broken by a jet.

The viscous flux vectors in Eq. (14) are

$$\hat{R}^{\eta} = J^{-1} \begin{bmatrix} 0 \\ \frac{1}{3}\mu\eta_x(\eta_x u_{\eta} + \eta_y v_{\eta} + \eta_z w_{\eta}) + \mu(\eta_x^2 + \eta_y^2 + \eta_z^2) u_{\eta} \\ \frac{1}{3}\mu\eta_y(\eta_x u_{\eta} + \eta_y v_{\eta} + \eta_z w_{\eta}) + \mu(\eta_x^2 + \eta_y^2 + \eta_z^2) v_{\eta} \\ \frac{1}{3}\mu\eta_z(\eta_x u_{\eta} + \eta_y v_{\eta} + \eta_z w_{\eta}) + \mu(\eta_x^2 + \eta_y^2 + \eta_z^2) w_{\eta} \\ \{(\eta_x^2 + \eta_y^2 + \eta_z^2)[\mu(uu_{\eta} + vv_{\eta} + ww_{\eta}) + \kappa Pr^{-1}(\gamma - 1)^{-1}(a^2)_{\eta}] \\ + \frac{1}{3}\mu(\eta_x u + \eta_y v + \eta_z w)(\eta_x u_{\eta} + \eta_y v_{\eta} + \eta_z w_{\eta})\} \end{bmatrix}, \quad (A1)$$

$$\hat{R}^{\zeta} = J^{-1} \begin{bmatrix} 0 \\ \mu[u_{\zeta}(\frac{4}{3}\eta_x \zeta_x + \eta_y \zeta_y + \eta_z \zeta_z) + v_{\zeta}(\eta_y \zeta_x - \frac{2}{3}\eta_x \zeta_y) + w_{\zeta}(\eta_z \zeta_x - \frac{2}{3}\eta_x \zeta_z)] \\ \mu[u_{\zeta}(\eta_x \zeta_y - \frac{2}{3}\eta_y \zeta_x) + v_{\zeta}(\eta_x \zeta_x + \frac{4}{3}\eta_y \zeta_y + \eta_z \zeta_z) + w_{\zeta}(\eta_z \zeta_y - \frac{2}{3}\eta_y \zeta_z)] \\ \mu[u_{\zeta}(\eta_x \zeta_z - \frac{2}{3}\eta_z \zeta_x) + v_{\zeta}(\eta_y \zeta_z - \frac{2}{3}\eta_z \zeta_y) + w_{\zeta}(\eta_x \zeta_x + \eta_y \zeta_y + \frac{4}{3}\eta_z \zeta_z)] \\ \mu u_{\zeta}(\frac{4}{3}\eta_x \zeta_x + v\eta_x \zeta_y + w\eta_x \zeta_z + u\eta_y \zeta_y + u\eta_z \zeta_z - \frac{2}{3}v\eta_y \zeta_x - \frac{2}{3}w\eta_z \zeta_x) \\ + \mu v_{\zeta}(\frac{4}{3}v\eta_y \zeta_y + u\eta_y \zeta_x + v\eta_x \zeta_x + w\eta_y \zeta_z + v\eta_z \zeta_z - \frac{2}{3}u\eta_x \zeta_y - \frac{2}{3}w\eta_z \zeta_y) \\ + \mu w_{\zeta}(\frac{4}{3}w\eta_z \zeta_z + u\eta_z \zeta_x + v\eta_z \zeta_y + w\eta_x \zeta_x + w\eta_y \zeta_y - \frac{2}{3}u\eta_x \zeta_z - \frac{2}{3}v\eta_y \zeta_z) \\ + \kappa Pr^{-1}(\gamma - 1)^{-1}(\eta_x \zeta_x + \eta_y \zeta_y + \eta_z \zeta_z)(a^2)_{\zeta} \end{bmatrix}, \quad (A2)$$

$$\hat{S}^{\eta} = J^{-1} \begin{bmatrix} 0 \\ \mu[u_{\eta}(\frac{4}{3}\zeta_x \eta_x + \zeta_y \eta_y + \zeta_z \eta_z) + v_{\eta}(\zeta_y \eta_x - \frac{2}{3}\zeta_x \eta_y) + w_{\eta}(\zeta_z \eta_x - \frac{2}{3}\zeta_x \eta_z)] \\ \mu[u_{\eta}(\zeta_x \eta_y - \frac{2}{3}\zeta_y \eta_x) + v_{\eta}(\zeta_x \eta_x + \frac{4}{3}\zeta_y \eta_y + \zeta_z \eta_z) + w_{\eta}(\zeta_z \eta_y - \frac{2}{3}\zeta_y \eta_z)] \\ \mu[u_{\eta}(\zeta_x \eta_z - \frac{2}{3}\zeta_z \eta_x) + v_{\eta}(\zeta_y \eta_z - \frac{2}{3}\zeta_z \eta_y) + w_{\eta}(\zeta_x \eta_x + \zeta_y \eta_y + \frac{4}{3}\zeta_z \eta_z)] \\ \mu u_{\eta}(\frac{4}{3}\zeta_x \eta_x + v\zeta_x \eta_y + w\zeta_x \eta_z + u\zeta_y \eta_y + u\zeta_z \eta_z - \frac{2}{3}v\zeta_y \eta_x - \frac{2}{3}w\zeta_z \eta_x) \\ + \mu v_{\eta}(\frac{4}{3}v\zeta_y \eta_y + u\zeta_y \eta_x + w\zeta_y \eta_z + v\zeta_x \eta_x + v\zeta_z \eta_z - \frac{2}{3}u\zeta_x \eta_y - \frac{2}{3}w\zeta_z \eta_y) \\ + \mu w_{\eta}(\frac{4}{3}w\zeta_z \eta_z + u\zeta_z \eta_x + v\zeta_z \eta_y + u\zeta_z \eta_x + v\zeta_z \eta_y - \frac{2}{3}u\zeta_x \eta_z - \frac{2}{3}v\zeta_y \eta_z) \\ + \kappa Pr^{-1}(\gamma - 1)^{-1}(\zeta_x \eta_x + \zeta_y \eta_y + \zeta_z \eta_z)(a^2)_{\eta} \end{bmatrix}, \quad (A3)$$

$$\hat{S}^{\zeta} = J^{-1} \begin{bmatrix} 0 \\ \frac{1}{3}\mu\zeta_x(\zeta_x u_{\zeta} + \zeta_y v_{\zeta} + \zeta_z w_{\zeta}) + \mu(\zeta_x^2 + \zeta_y^2 + \zeta_z^2) u_{\zeta} \\ \frac{1}{3}\mu\zeta_y(\zeta_x u_{\zeta} + \zeta_y v_{\zeta} + \zeta_z w_{\zeta}) + \mu(\zeta_x^2 + \zeta_y^2 + \zeta_z^2) v_{\zeta} \\ \frac{1}{3}\mu\zeta_z(\zeta_x u_{\zeta} + \zeta_y v_{\zeta} + \zeta_z w_{\zeta}) + \mu(\zeta_x^2 + \zeta_y^2 + \zeta_z^2) w_{\zeta} \\ \{(\zeta_x^2 + \zeta_y^2 + \zeta_z^2)[\mu(uu_{\zeta} + vv_{\zeta} + ww_{\zeta}) + \kappa Pr^{-1}(\gamma - 1)^{-1}(a^2)_{\zeta}] \\ + \frac{1}{3}\mu(\zeta_x u + \zeta_y v + \zeta_z w)(\zeta_x u_{\zeta} + \zeta_y v_{\zeta} + \zeta_z w_{\zeta})\} \end{bmatrix}, \quad (A4)$$

References

1. Allen, H.J. and Perkins, E.W., "A Study of the Effects of Viscosity on Flow Over Slender Inclined Bodies of Revolution," NACA TR 1048, 1951.
2. Jorgenson, L.H. and Perkins, E.W., "Investigation of Some Wake Vortex Characteristics of an Inclined Ogive-Cylinder Body at Mach Number 2," NACA TR 1371, 1958.
3. Lamont, P.J. and Hunt, B.L., "Pressure and force distributions on a sharp-nosed circular cylinder at large angles of inclination to a uniform subsonic stream," J. fluid Mech. (1976) Vol. 76, part 3, pp. 519-559.
4. Keener, E.R., Chapman, G.T., Cohen, L., and Taleghani, J., "Side Forces on a Tangent Ogive Forebody with a Fineness Ratio of 3.5 at High Angles of Attack and Mach Numbers from 0.1 to 0.7," NASA TM X-3437, 1977.
5. Dexter, P.C. and Hunt, B.L., "The Effects of Roll Angle on the Flow over a Slender Body of Revolution at High Angles of Attack," AIAA Paper 81-358, Jan. 1981.
6. Lamont, P.J., "Pressure Measurements on an Ogive-Cylinder at High Angles of Attack with Laminar, Transition, or Turbulent Separation," AIAA Paper 80-1556-CP, August, 1980.
7. Lamont, P.J., "the Complex Asymmetric Flow Over a 3.5D Ogive Nose and Cylindrical Afterbody at High Angles of Attack," AIAA Paper 812-0053, Jan. 1982.
8. Wardlaw, A.B., "Multivortex Model of Asymmetric Shedding on Slender Bodies at High Angle of Attack," AIAA Paper 75-123, Jan. 1975.
9. Deffenbaugh, F.D. and Koerner, W.G., "Asymmetric Vortex Wake Development on Missiles at High Angles of Attack," Journal of Spacecraft, Vol. 14, No. 3, 1977, pp. 155-162.
10. Mendenhall, M.R. and Perkins, S.C., "Prediction of the Vortex Wake for Noncircular Missiles in Supersonic Flow", AIAA Paper 84-0504, Jan. 1984.

11. Smith, J.H.B., "Behavior of a Vortex Sheet Separating From a Smooth Surface," RAE TR 77058, 1977.
12. Almosnino, D., "High-Angle-of-Attack Calculations of the Subsonic Vortex Flow on Slender Bodies," AIAA J., Vol. 23, No. 8, 1985, pp. 1150-1156.
13. Strigberger, J., "A Viscous/Inviscid Zonal Method for the Computation of Two and Three-Dimensional Compressible Fluid Flows with "Separation", Ph.D. Thesis, Stanford Univ., Oct. 1985.
14. L.B. Schiff and W.B. Sturek, "Numerical Simulation of Steady Supersonic Flow Over an Ogive-Cylinder-Boattail Body," AIAA 18th Aerospace Sciences Meeting, Pasadena, CA, January 14-16, 1980.
15. L.B. Schiff and J.L. Steger, AIAA J. 18. 1421 (1980).
16. R.P. Reklis and W.B. Sturek, "Surface Pressure Measurements on Slender Bodies at Angle of Attack in Supersonic Flow", ARBRL-MR-02876, November 1978 (unpublished).
17. L.D. Kayser and W.B. Sturek, "Experimental Measurements in the Turbulent Boundary Layer of a Yawed, Spinning, Ogive-Cylinder body of Revolution at Mach 3.0, Part II, Data Tabulation," ARBRL-MR-028113, March 1978 (unpublished).
18. L. D. Kayser and W.B. Sturek, "Turbulent Boundary Layer Measurements on the Boattail Section of a Yawed, Spinning Projectile Shape at Mach 3.0," ARBRL-MR-02880, November 1978 (unpublished).
19. D. Degani and L.D. Schiff, "Computation of Turbulent Supersonic flows around Pointed Bodies Having Crossflow Separation", Journal of Computational Physics 66, 173-196, 1986.
20. W.J. Bannink and C. Nebbeling. "Measurement of the Supersonic Flow Field Past a Slender Cone at High Angles of Attack", AGARD cp-247, 1978.
21. D.J. Peake, F.K. Owen and D.A. Johnson, "Control of Forebody Vortex Orientation to Alleviate Side Forces", AIAA Paper 80-0183, 1980.
22. M.W. Rubesin, "A One-Equation Model of Turbulence for Use with the Compressible Navier-Stokes Equations", NASA TM X-73, 128, 1976.

23. G.S. Glashko, "Turbulent Boundary Layer on a Flat Plate in an Incompressible Fluid", Bull. Acad. Sci. USSR, Mech. Ser., 4, 1965, pp. 13-23.
24. Ying,, S.X., Steger, J.L., Schiff, L.B., Baganoff, D., "Numerical Simulation on Unsteady, Viscous, High-Angle-of-Attack Using a Partially Flux-Split Algorithm," AIAA Paper 816-2179, August, 1986.
25. Shapira, M., Degani, D. and Weiss, D., "Viscous Flow in a Divergent Channel of Arbitrary Angle, and its stability," TME-1432, 1986.
26. R.M. Beam and R.F. Warming, AIAA J. 16. 393 (1978).
27. L.B. Schiff and J.L. Steger, "Numerical Simulation of Steady Supersonic Viscous Flow," NASA TP-1749, May 1981 (unpublished).
28. Ying, S.X., "Three-Dimensional Implicit Approximately Factored Schemes for Equations of Gasdynamics," Ph.D. Thesis, Stanford Univ., June, 1986.
29. B.S. Baldwin and H. Lomax, "Thin Layer Approximation and Algebraic Model for Separated Turbulent Flows", AIAA 16th Aerospace Sciences Meeting, Huntsville, AL. January 16-18, 1978.
30. T. Cebeci, "Calculation of Compressible Turbulent Boundary Layers with Heat and Mass Transfer," AIAA 3rd Fluid and Plasma Dynamics Conference, Los Angeles, CA, June 29-July 1, 1970.
31. Degani, D. and Smits, A.J., "Numerical Study of the Response of a Compressible, turbulent Boundary Layer to a Short Region of Surface Curvature", AIAA 18th Fluid Dynamics and Plasmadynamics and Lasers Conference, Cincinnati, Ohio, July, 1985.
32. Hall, R.M., "Forebody and Missile Side Forces and the Time Analogy", AIAA Paper 87-0327, 1987.
33. Payne, F.M., Ng, T.T., Nelson, R.C. and Schiff, L.B., "Visualization and Flow Surveys of the Leading Edge Vortex Structure on Delta Wing Planforms", AIAA Paper 87-0330, 1987.
34. Blackwelder, R.F. and Gad-el-Hak, M., "The Discrete Vortices from a Delta Wing," AIAA J. Vol. 23, NO. 6, 1985, pp. 961-962.

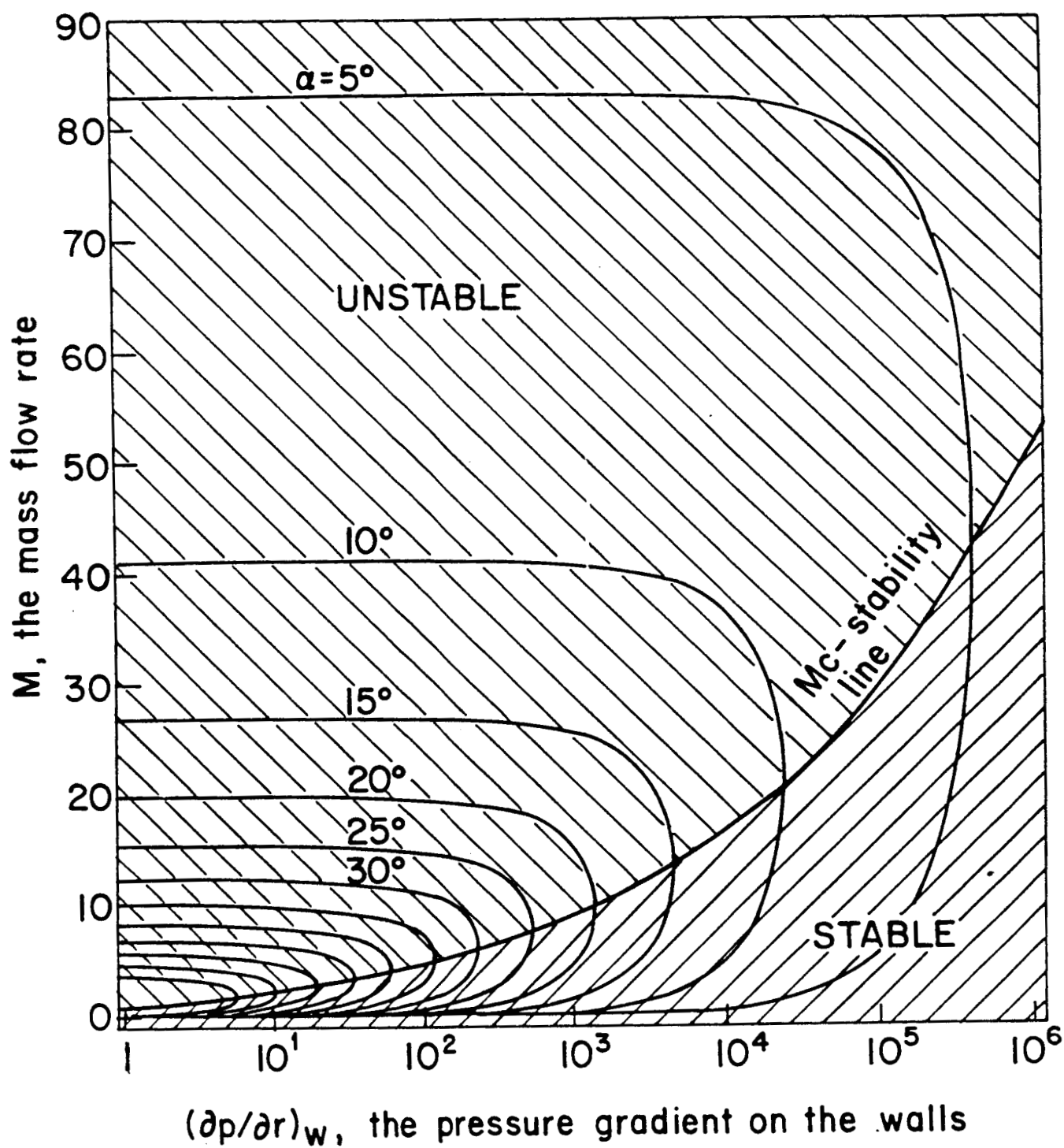


Fig. 1 - Contours of constant α , in the plane of M (the mass flow rate) vs. $(\partial p / \partial r)_w$ (the pressure gradient on the walls), where the pressure decreases, in the downstream direction. M_c Curve - stability line, and zones of stability and instability.

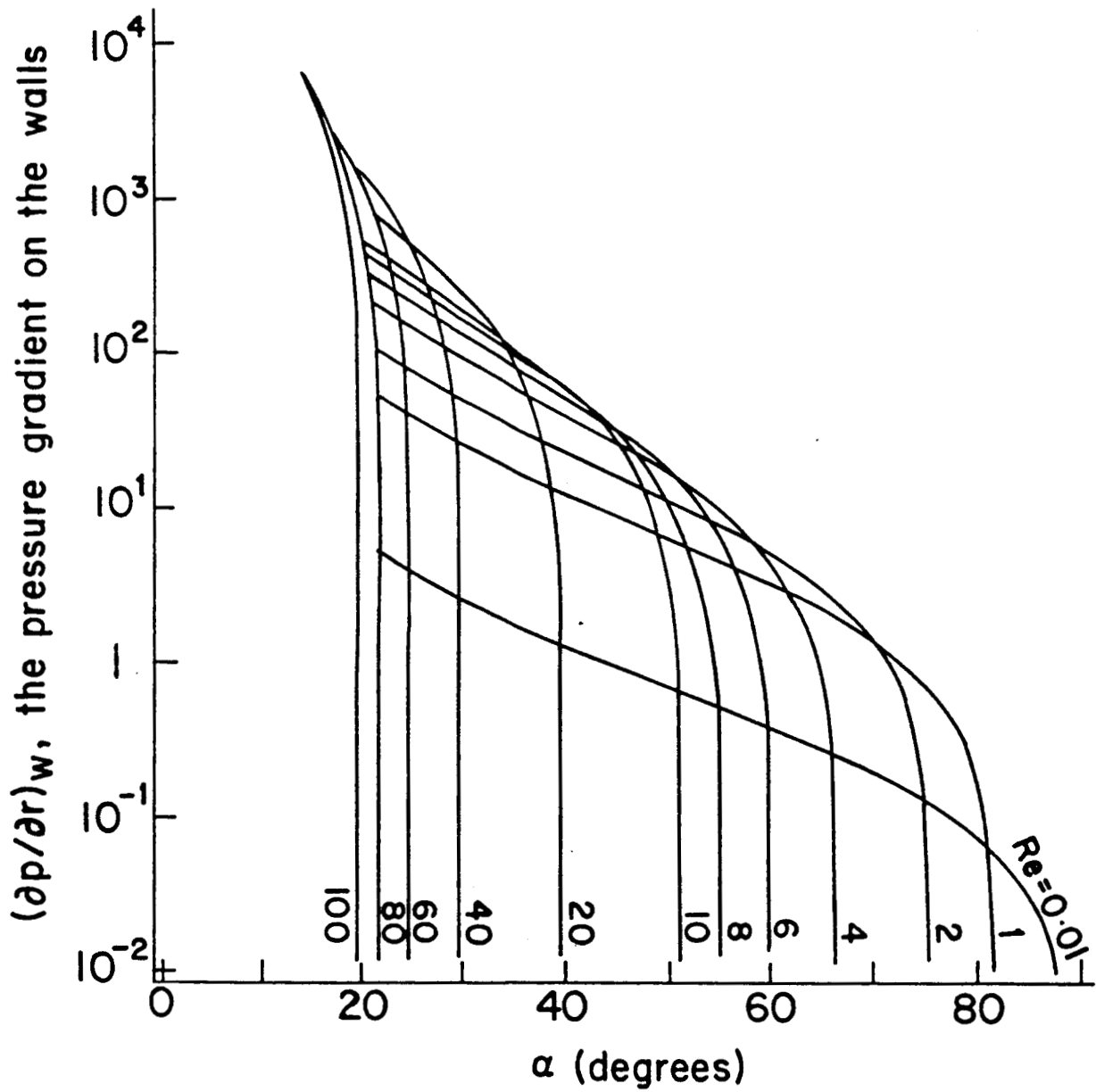


Fig. 2 - Contours of constant Re , in the plane of $(\partial p / \partial r)_w$ (the pressure gradient on the walls) vs. α where the pressure decreases, in the downstream direction.

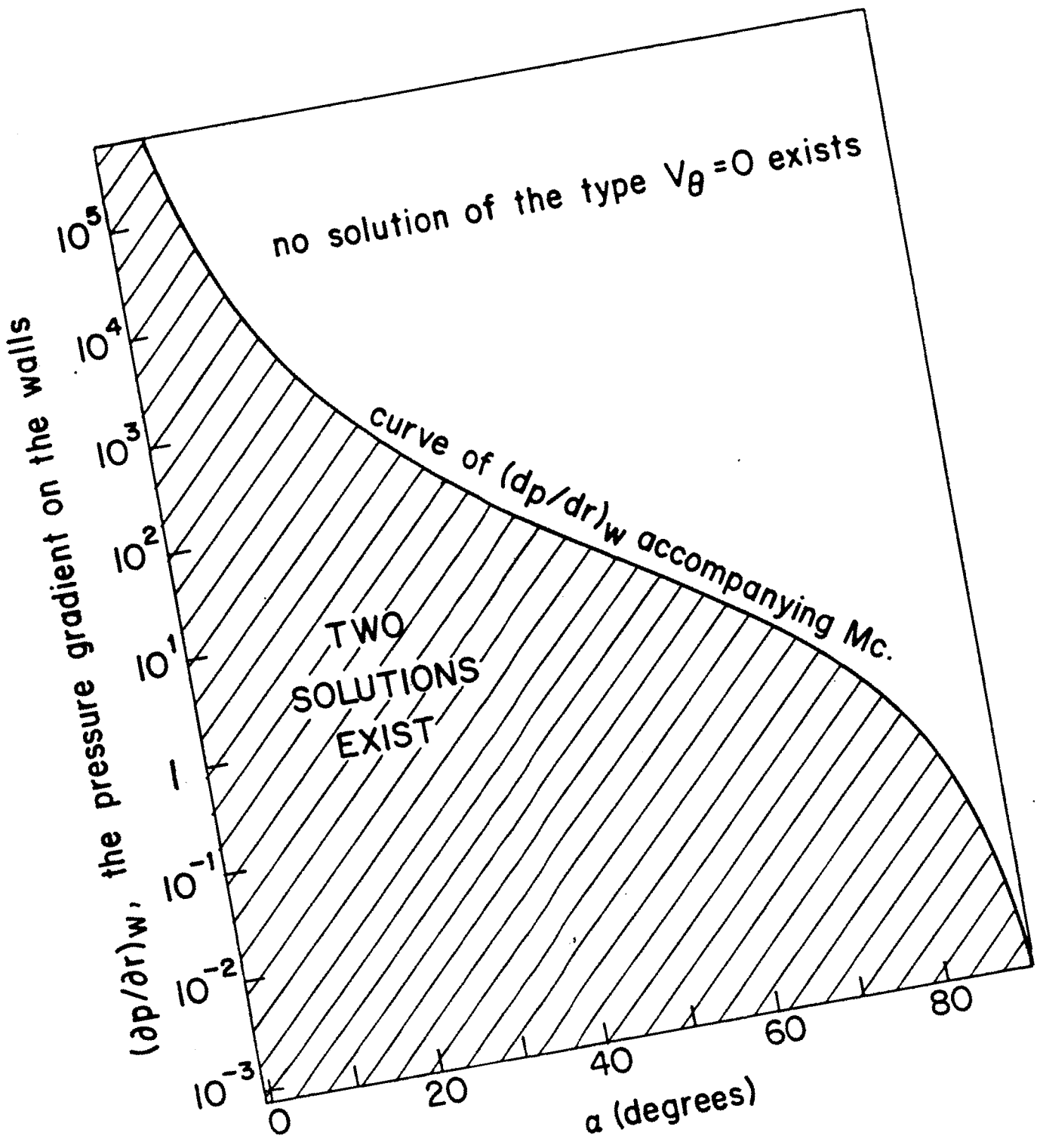


Fig. 3 - The zone of two solutions, and the zone where no solution of the type $V_\theta = 0$ exists, where the pressure decreases, in the downstream direction, and the curve of $(dp/dr)_w$ accompanying M_c .

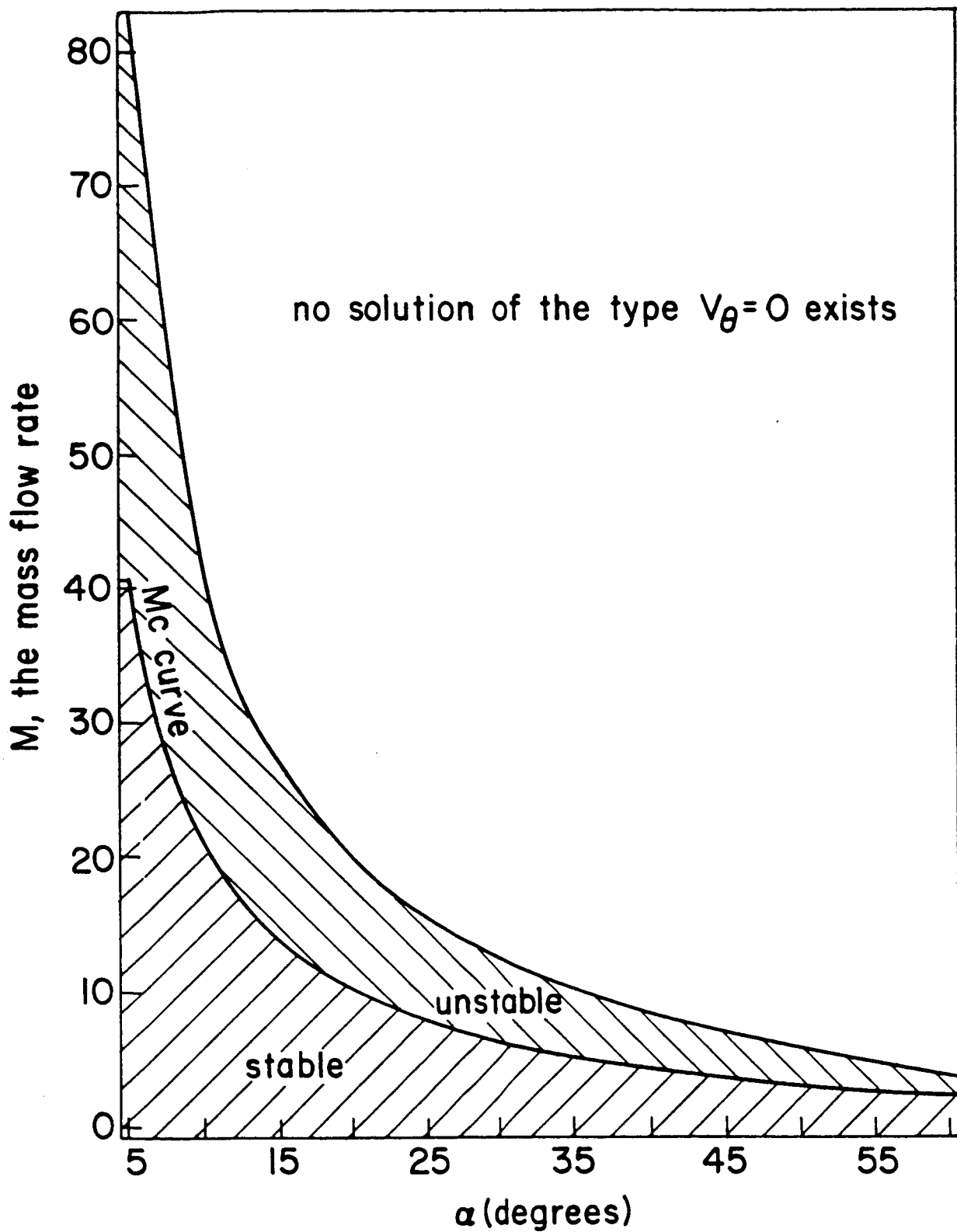


Fig. 4 - Zones of existence of solutions and their stability, where the pressure decreases, in the downstream direction and the curve of M_c .

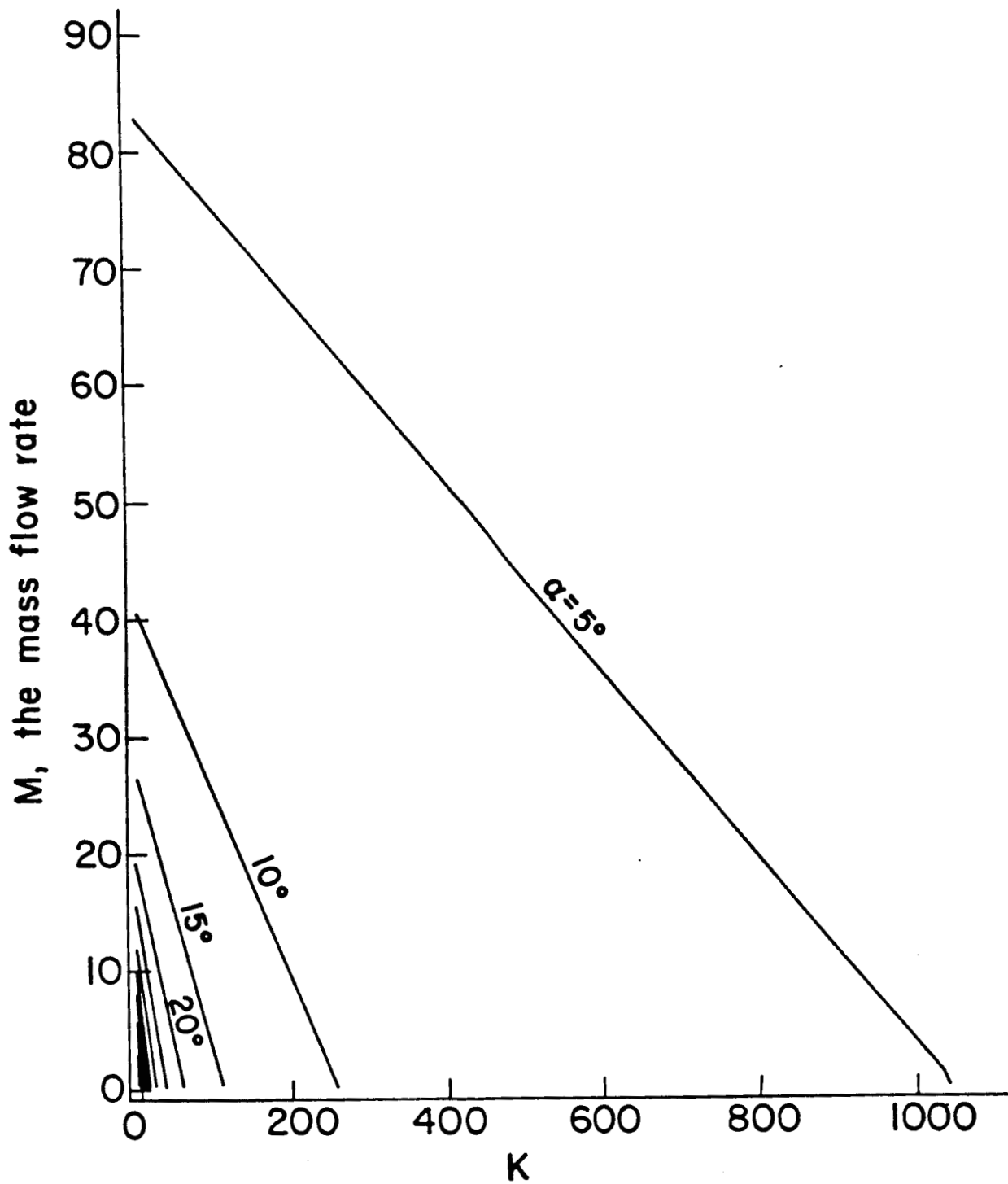


Fig. 5 - Contours of constant α , in the plane of M (the mass flow rate) vs. k, where the pressure decreases, in the downstream direction.

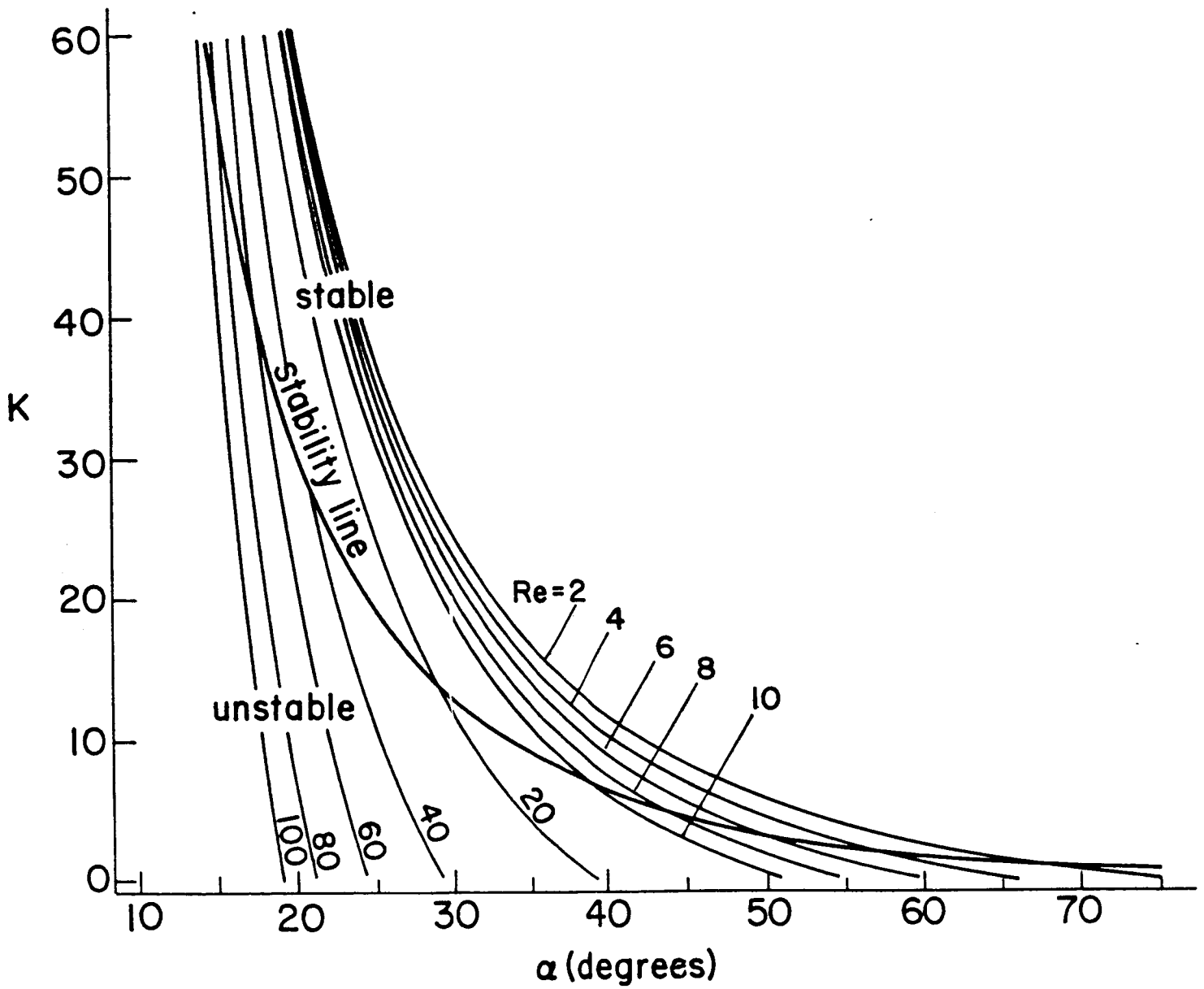


Fig. 6 - Contours of constant Re, where the pressure decreases, in the downstream direction, and stability line, in the plane of k vs. α .

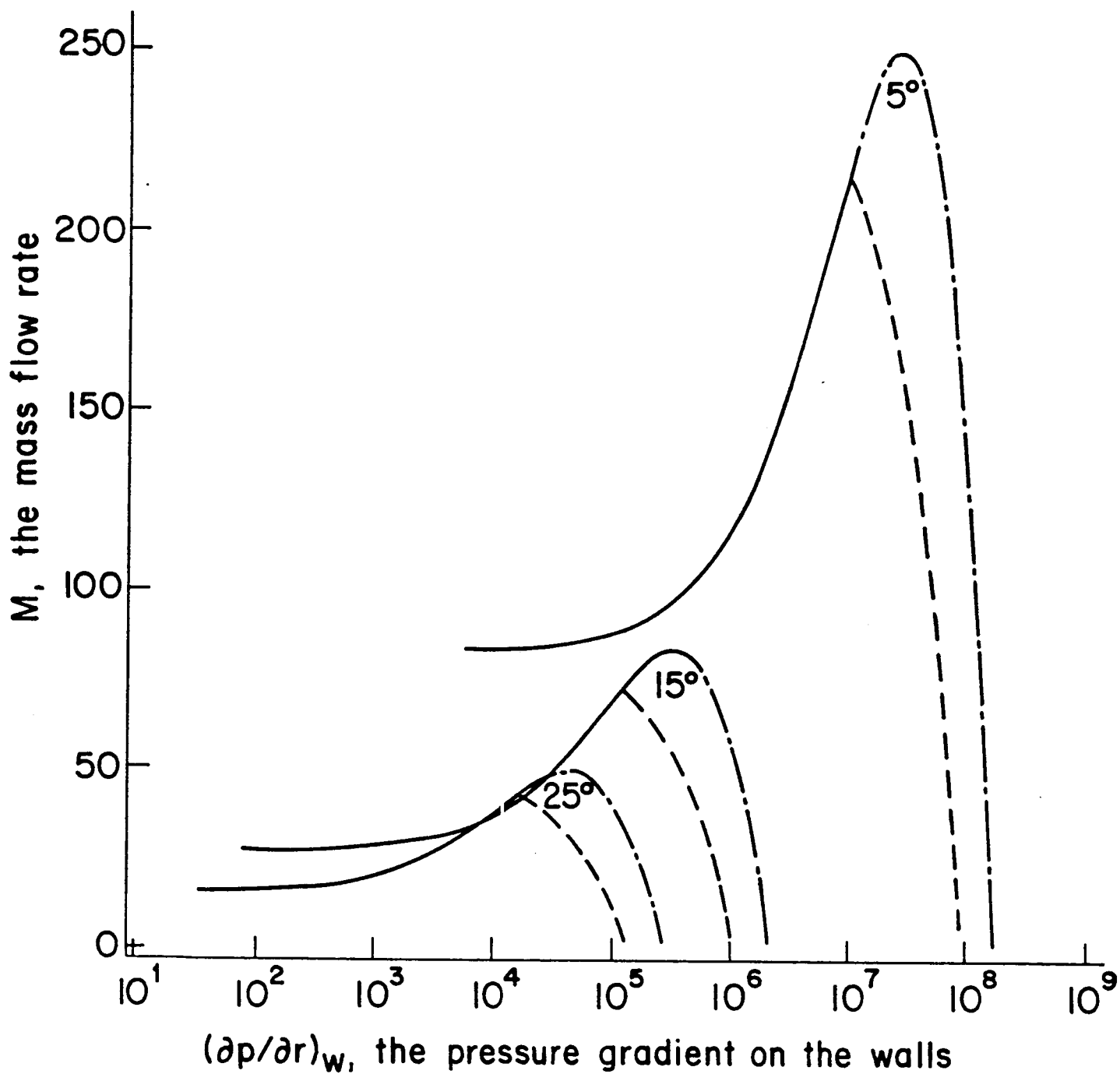


Fig. 7 - Contours of constant α , in the plane of M (mass flow rate) vs. $(\partial p / \partial r)_w$ (the pressure gradient on the walls), for the case where only one range of positive velocity exists, and the pressure increases, in the downstream direction.

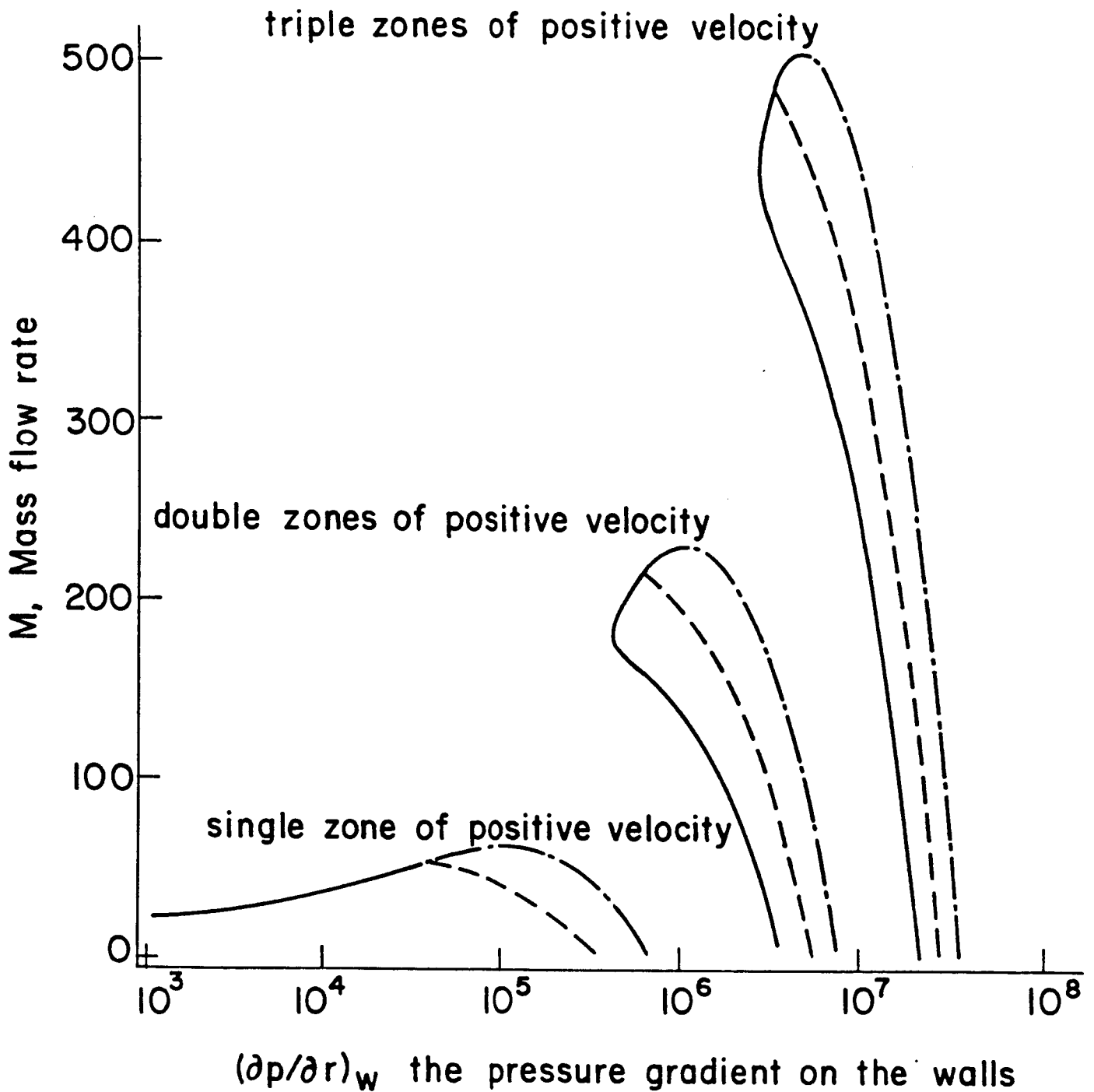


Fig. 8 - Curves of $\alpha = 20^\circ$ in the plane of M (the mass flow rate) (vs. $(\partial p / \partial r)_w$ (the pressure gradient on the walls)) for single double and triple positive direction velocity zones, where the pressure increases, in the downstream direction.

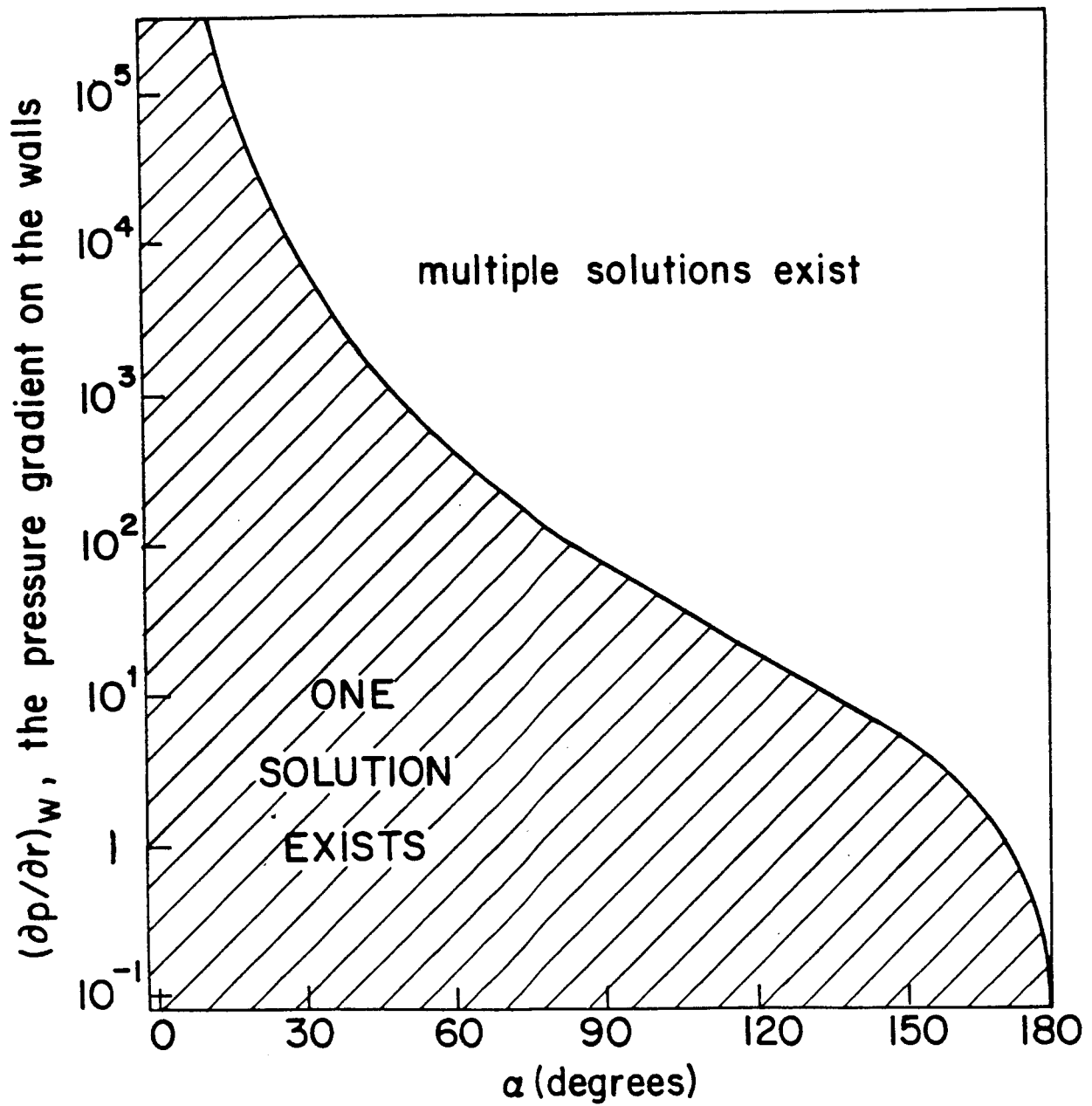
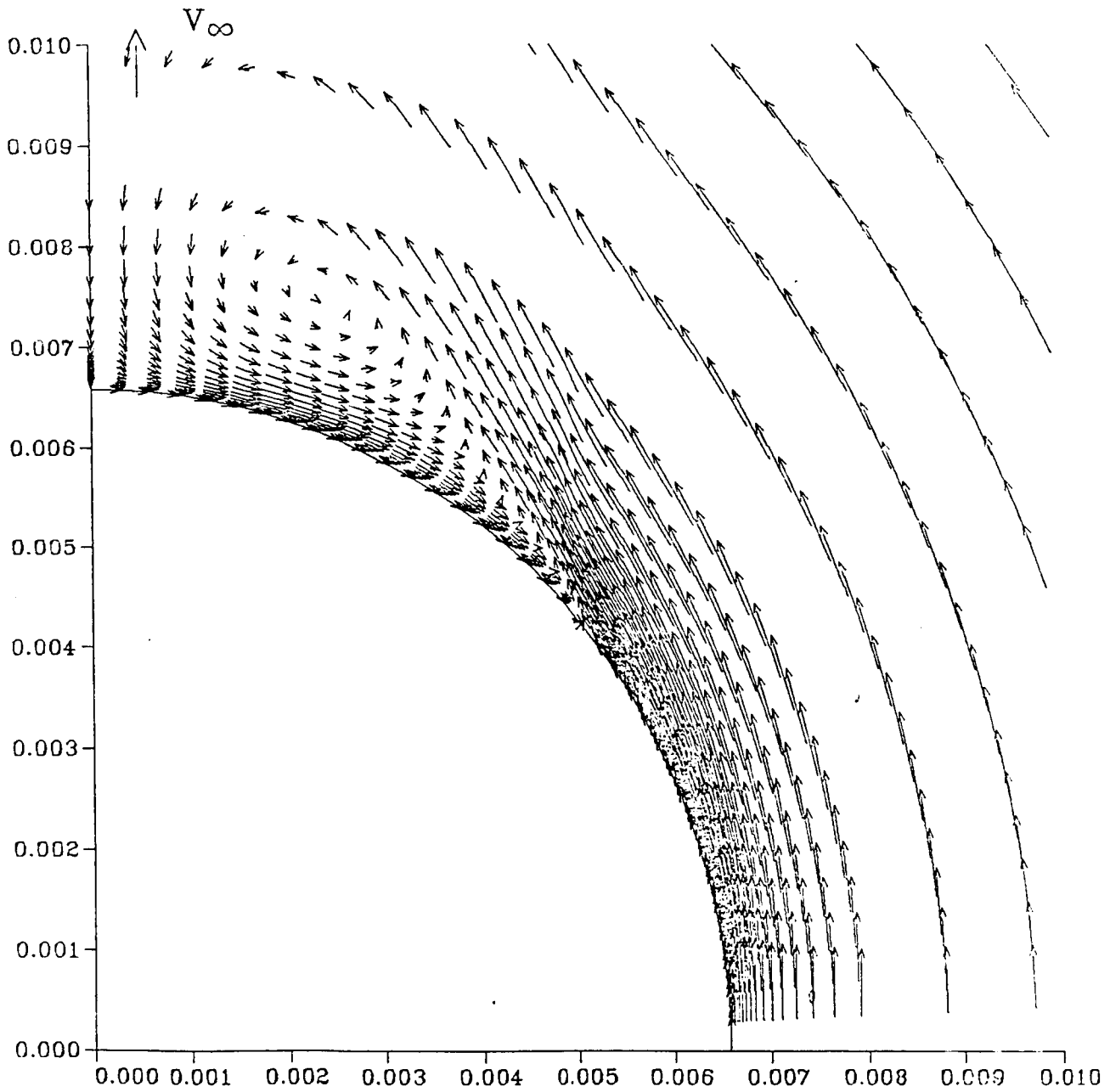


Fig. 9 - The zones where one solution and multiple solutions exist, in the plane of $(\partial p / \partial r)_w$ (the pressure gradient on the walls) vs. α , where the pressure increases, in the downstream direction.

ORIGINAL PAGE IS
OF POOR QUALITY

VELOCITY VECTORS

CONE 7.5 DEG., ALPHA = 22.6 DEG., MACH = 2.94

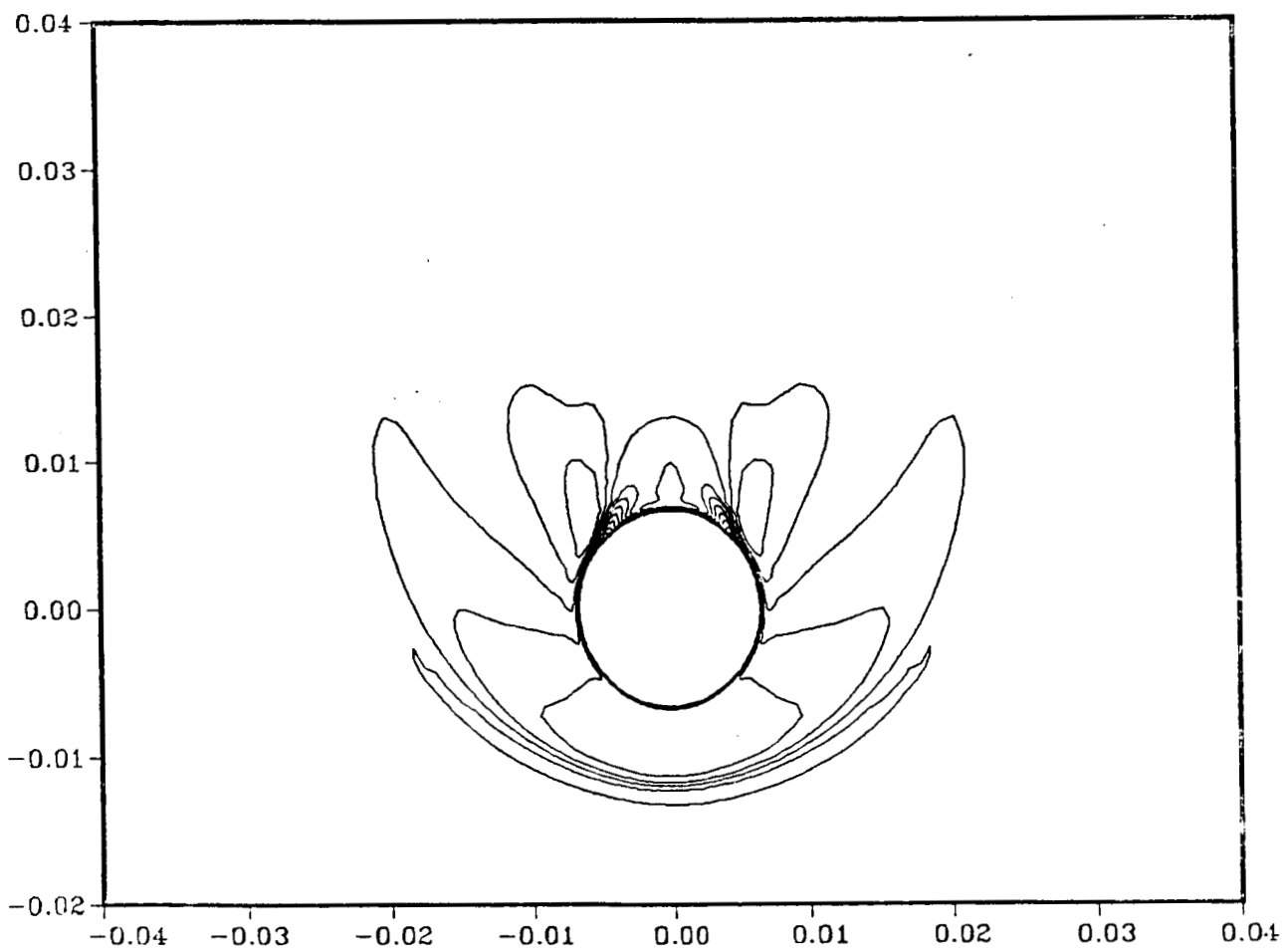


$M_\infty = 2.94$ $\alpha = 22.60$ $Re = 1.372 \cdot 10^7$ $X = 0.0500$

Fig. 10 - Conical solution. Velocity vectors, $\alpha = 22.6^\circ$.

MACH CONTOURS

CONE 7.5 DEG., ALPHA = 22.6 DEG., MACH = 2.94



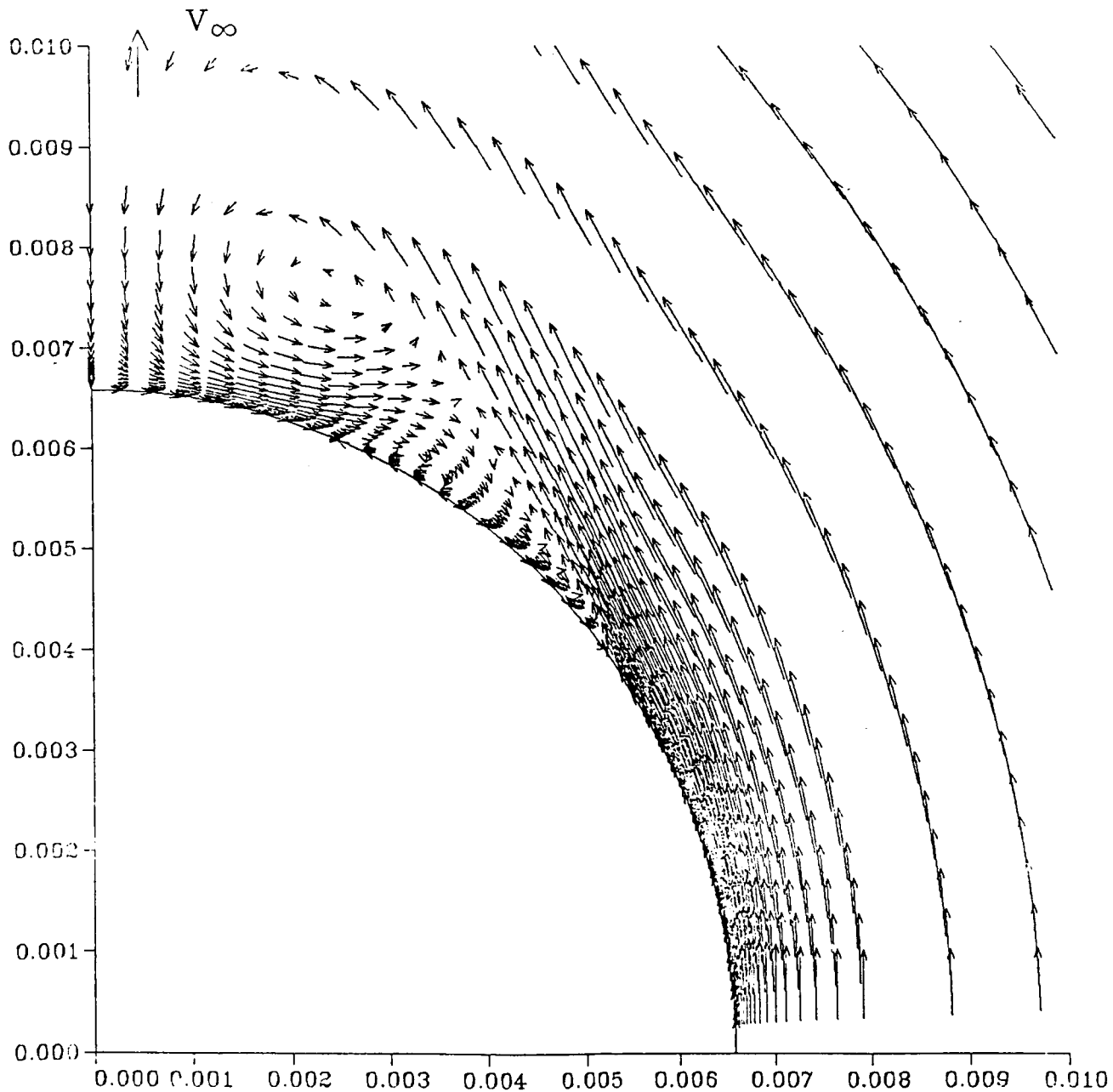
$M_\infty = 2.94$ $\alpha = 22.60$ $Re = 1.372 \cdot 10^7$ $X = 0.0500$

Fig. 11 - Conical solution. Mach contours, $\alpha = 22.6^\circ$.

ORIGINAL PAGE IS
OF POOR QUALITY

VELOCITY VECTORS

CONE 7.5 DEG., ALPHA = 22.6 DEG., MACH = 2.94

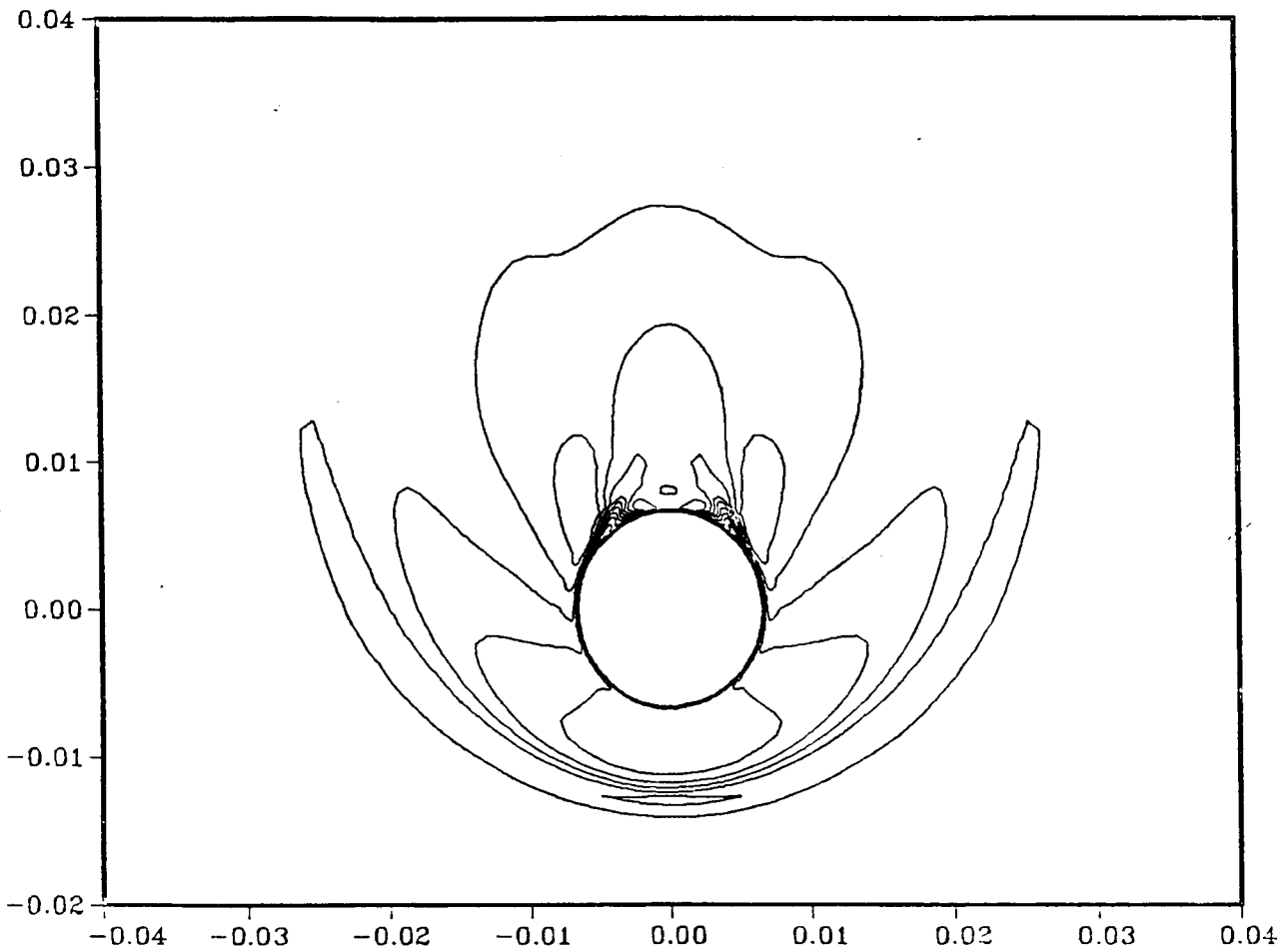


$M_\infty = 2.94$ $\alpha = 22.60$ $Re = 1.372 \cdot 10^7$ $X = 0.0500$

Fig. 12 - Conical solution. Velocity vectors, $\alpha = 22.6^\circ$.

MACH CONTOURS

CONE 7.5 DEG., ALPHA = 22.6 DEG., MACH = 2.94



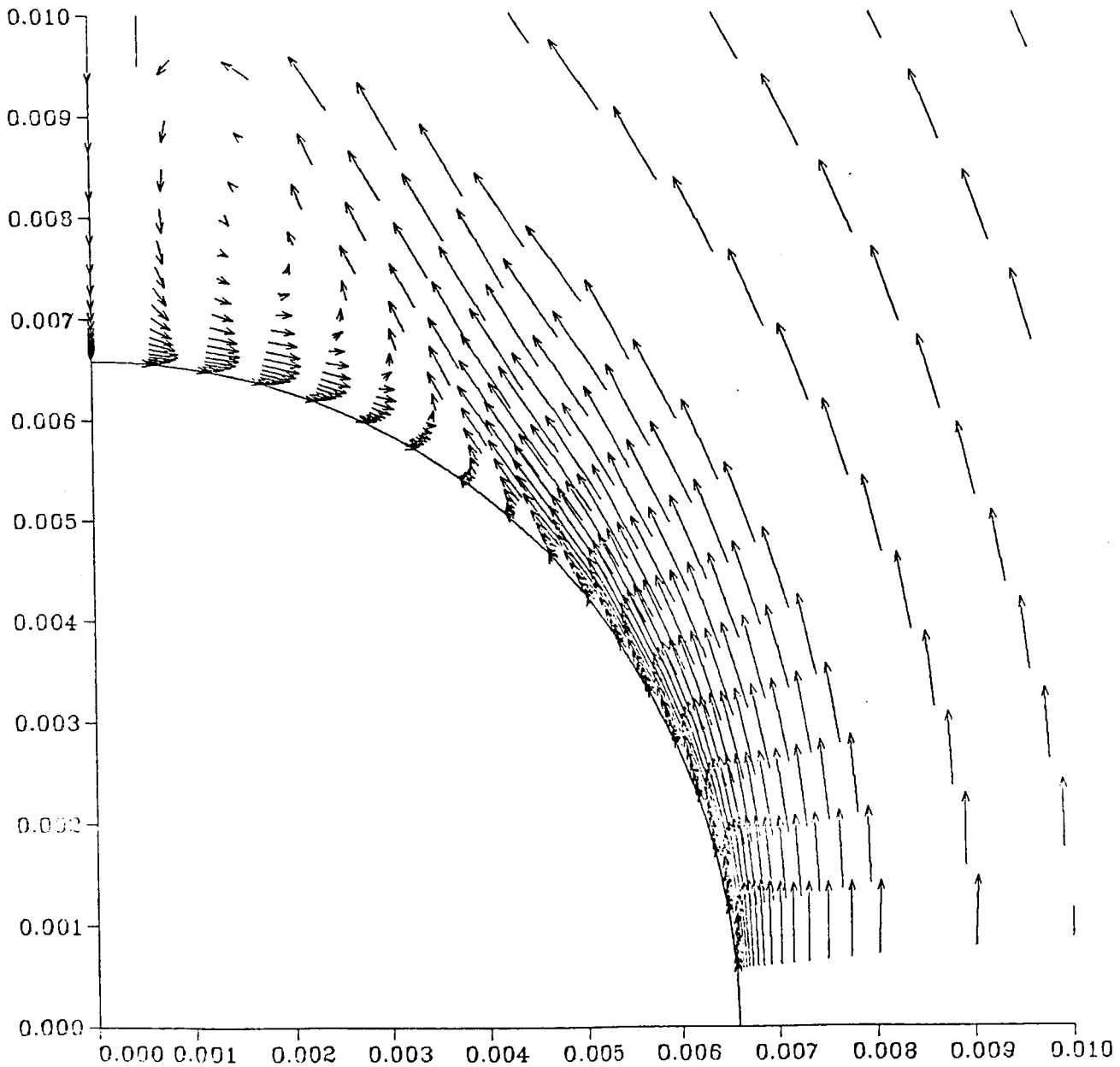
$M_\infty = 2.94$ $\alpha = 22.60$ $Re = 1.372 \cdot 10^7$ $X = 0.0500$

Fig. 13 - Conical solution. Mach contours, $\alpha = 22.6^\circ$.

VELOCITY VECTORS

CONE 7.5 DEG., ALPHA = 34.0 DEG., MACH = 2.94

V_∞



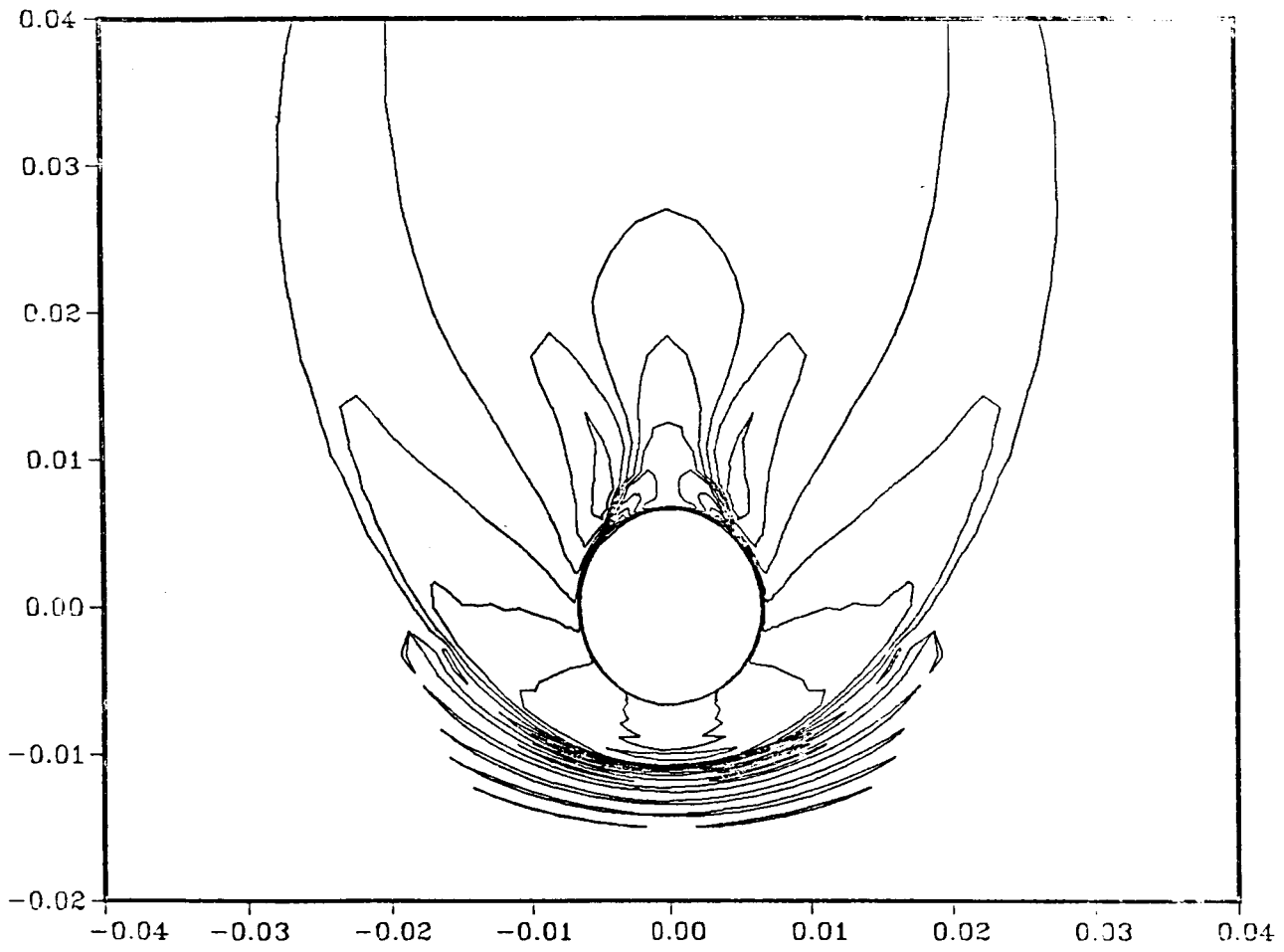
$M_\infty = 2.94$ $\alpha = 34.00$ $Re = 1.372 \cdot 10^7$ $X = 0.0500$

Fig. 14 - Conical solution. Velocity vectors, $\alpha = 34^\circ$.

ORIGINAL PAGE IS
OF POOR QUALITY

MACH CONTOURS

CONE 7.5 DEG., ALPHA = 34.0 DEG., MACH = 2.94



$M_{\infty} = 2.94$ $\alpha = 34.00$ $Re = 1.372 \cdot 10^7$ $X = 0.0500$

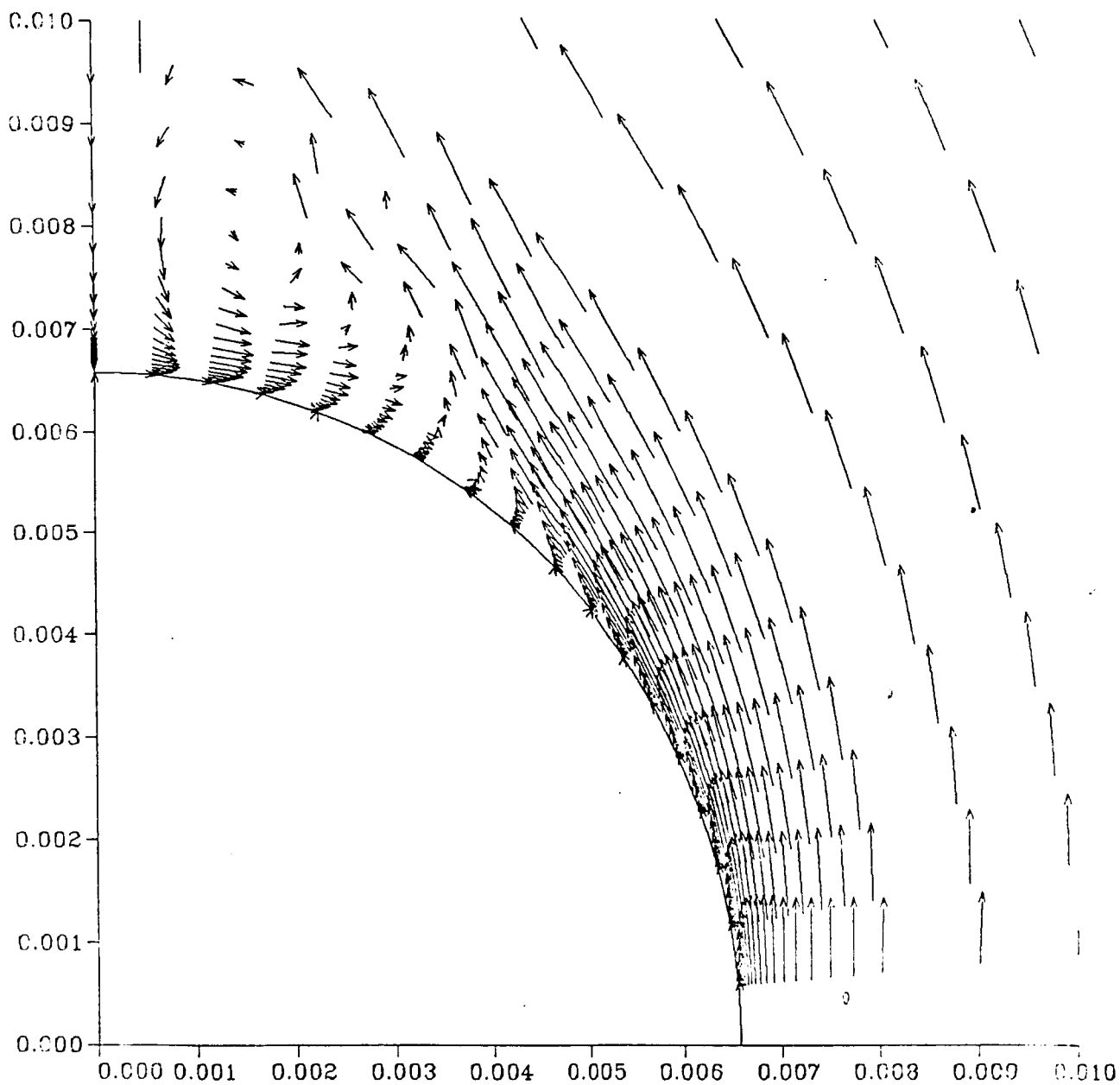
Fig. 15 - Conical solution. Mach contours, $\alpha = 34^{\circ}$.

ORIGINAL PAGE IS
OF POOR QUALITY

VELOCITY VECTORS

CONE 7.5 DEG., ALPHA = 34.0 DEG., MACH = 2.94

V_∞

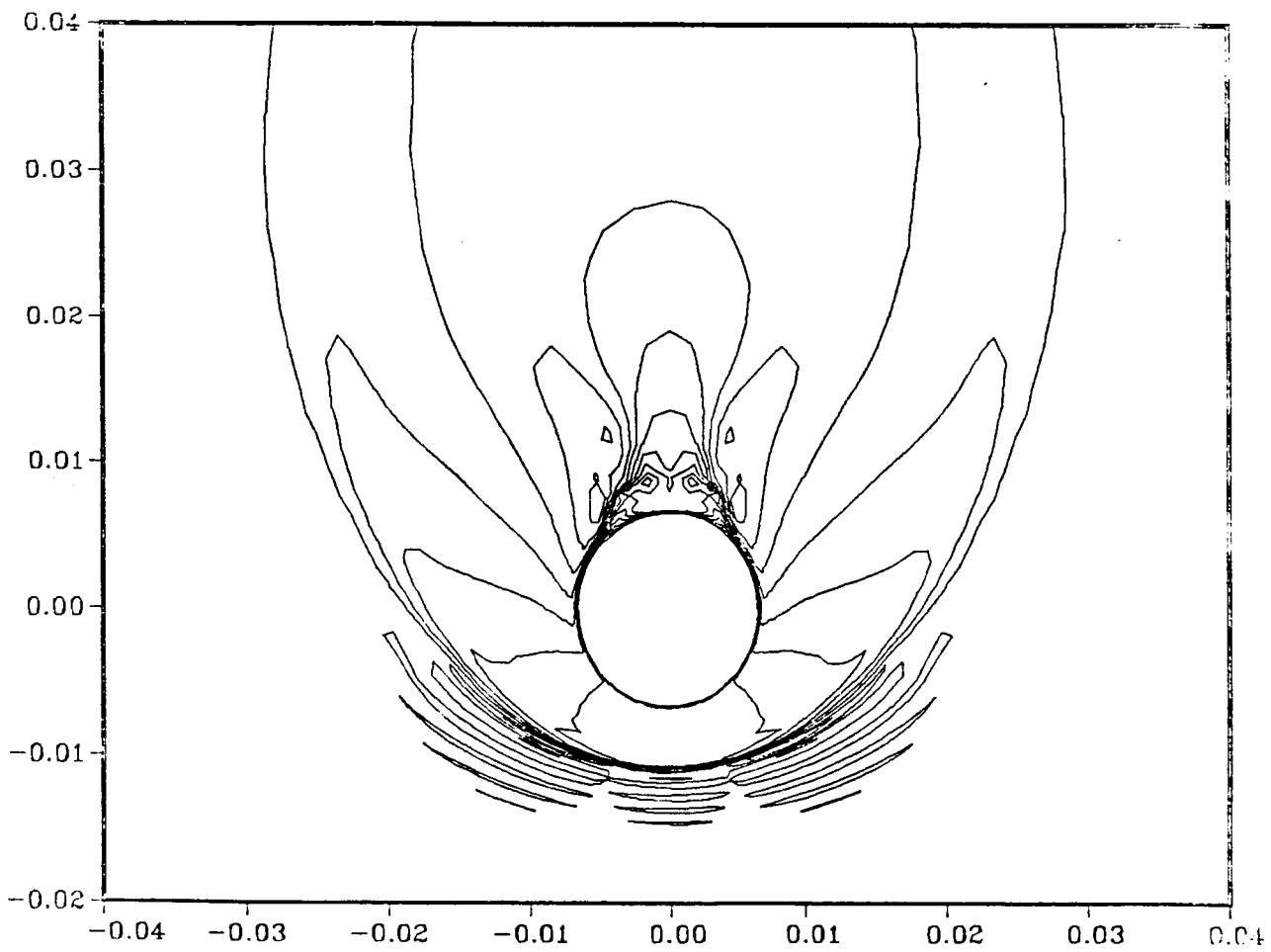


$M_\infty = 2.94$ $\alpha = 34.00$ $Re = 1.372 \cdot 10^7$ $X = 0.0500$

Fig. 16 - Conical solution. Velocity vectors, $\alpha = 34^\circ$.

MACH CONTOURS

CONE 7.5 DEG., ALPHA = 34.0 DEG., MACH = 2.94

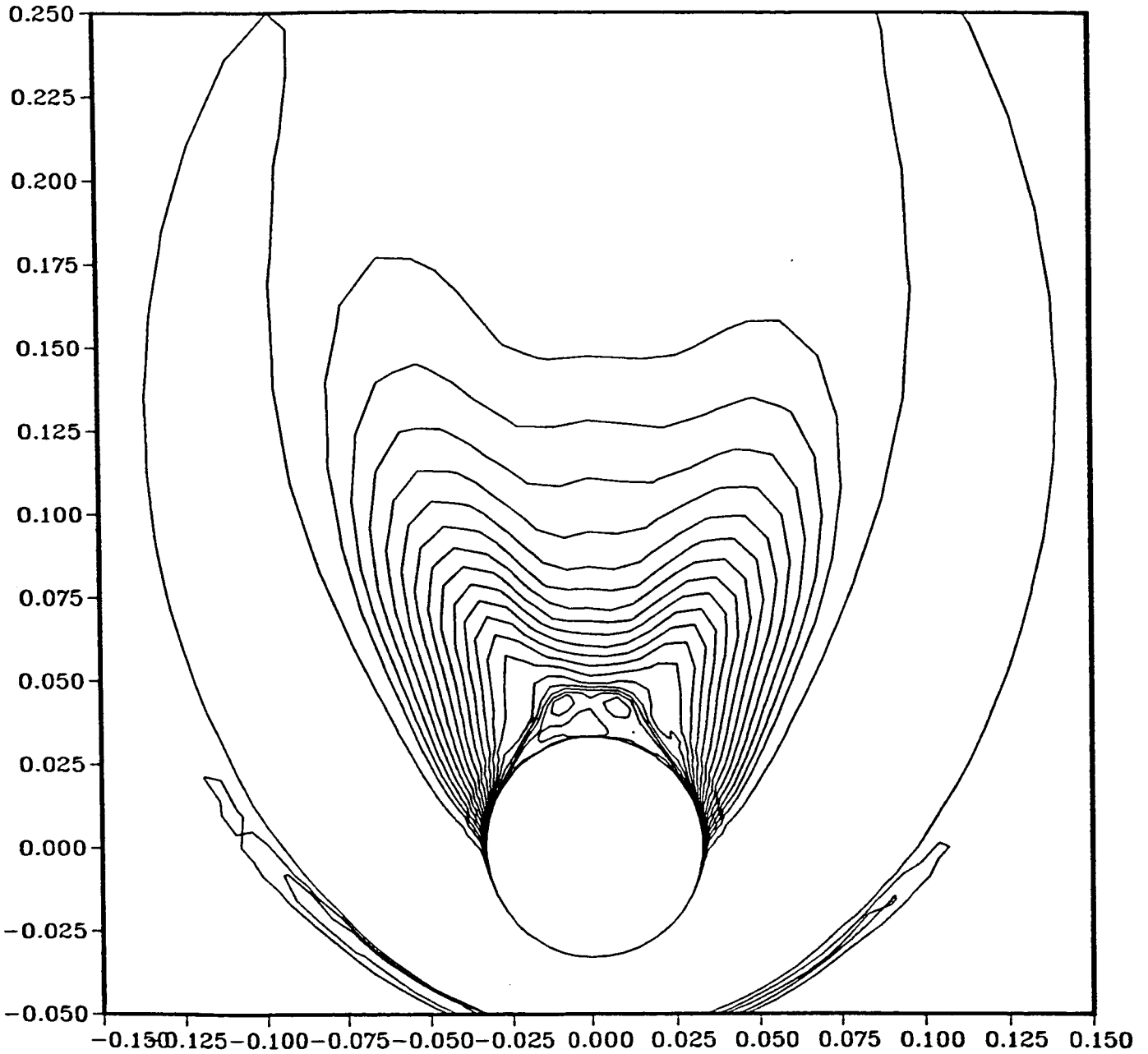


$M_\infty = 2.94$ $\alpha = 34.00$ $Re = 1.372 \cdot 10^7$ $X = 0.0500$

Fig. 17 - Conical solution. Mach contours, $\alpha = 34^\circ$.

DENSITY CONTOURS

MARCHING ON 7.5 DEG. CONE



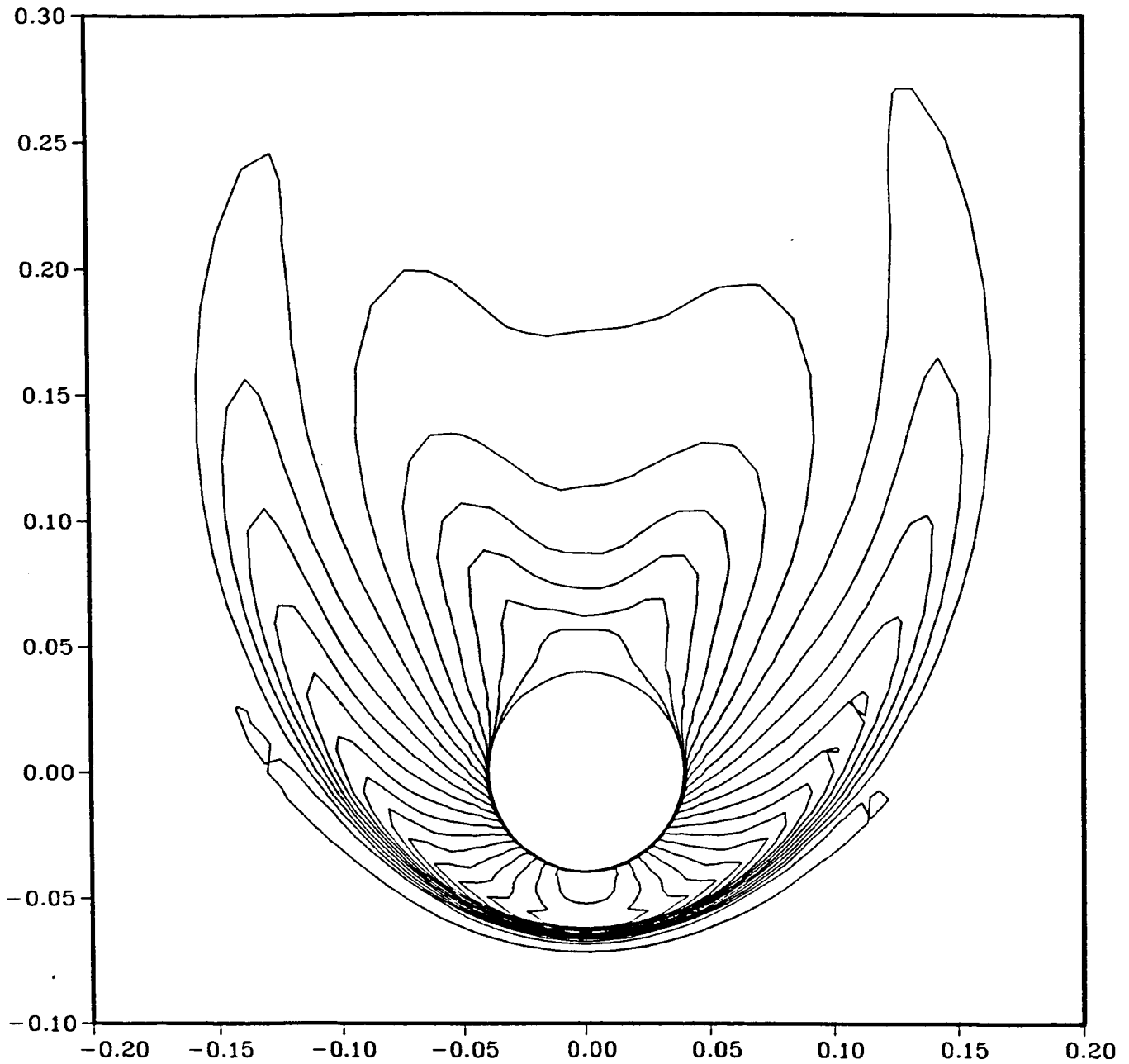
$M_\infty = 2.94$ $\alpha = 34.00$ $Re = 1.372 \cdot 10^7$ $X = 0.2500$

Fig. 18_a - Marching solution. Density Contours at different stations,
 $\alpha = 34^\circ$.

19.56.13 MED 5 FEB, 1986 JOB=CPL0T , MISA ARES DISSPLA 9.0
PLOT 1

DENSITY CONTOURS

cone 7.5 DEG. MARCHING



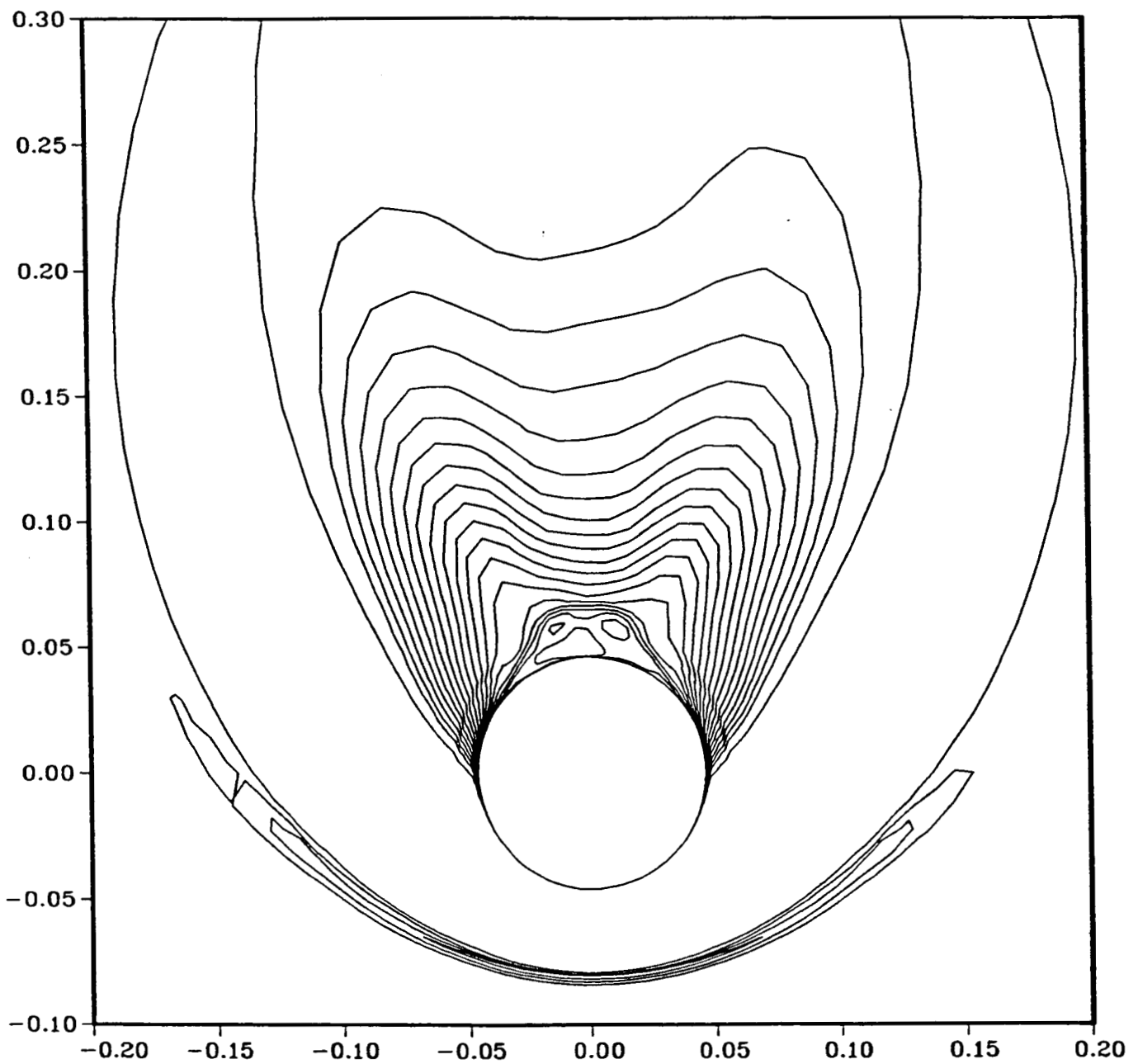
$M_\infty = 2.94$ $\alpha = 34.00$ $Re = 1.372 \cdot 10^7$ $X = 0.3000$

Fig. 18_b - Marching solution. Density Contours at different stations,
 $\alpha = 34^\circ$.

PLU1 2' 16.49.04 WED 5 11B, 1986 JUB-UNIV/LOT, NWSR AMES DISPLA 9.0

DENSITY CONTOURS

MARCHING ON 7.5 DEG. CONE



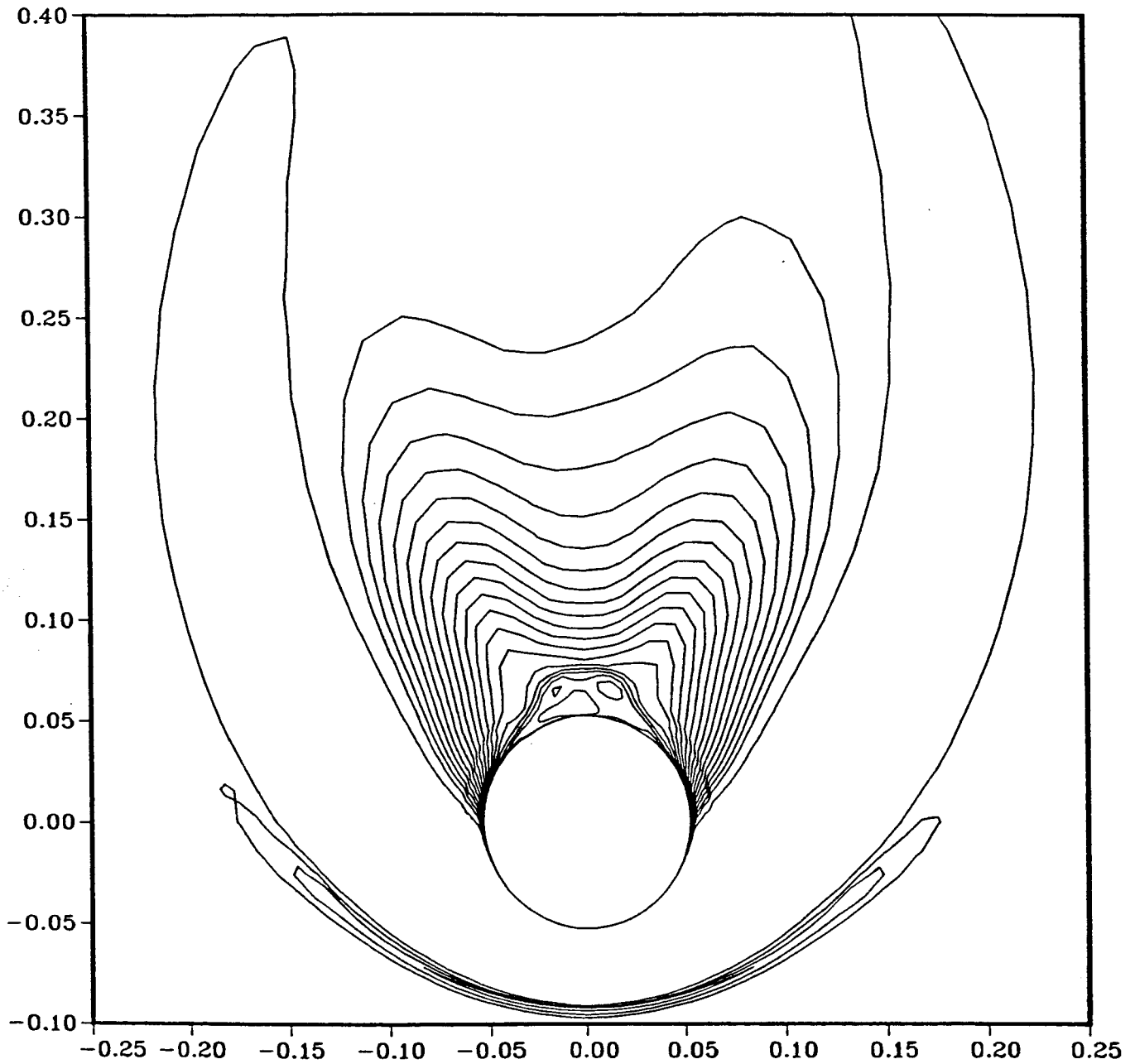
$M_\infty = 2.94$ $\alpha = 34.00$ $Re = 1.372 \cdot 10^7$ $X = 0.3500$

Fig. 18_c - Marching solution. Density Contours at different stations,
 $\alpha = 34^\circ$.

PLU1 1 - 20.38146 HDU 5 FEB, 1986 JUU-U-LUI , NISA PALS UISSPLA 9.0

DENSITY CONTOURS

MARCHING ON 7.5 DEG. CONE



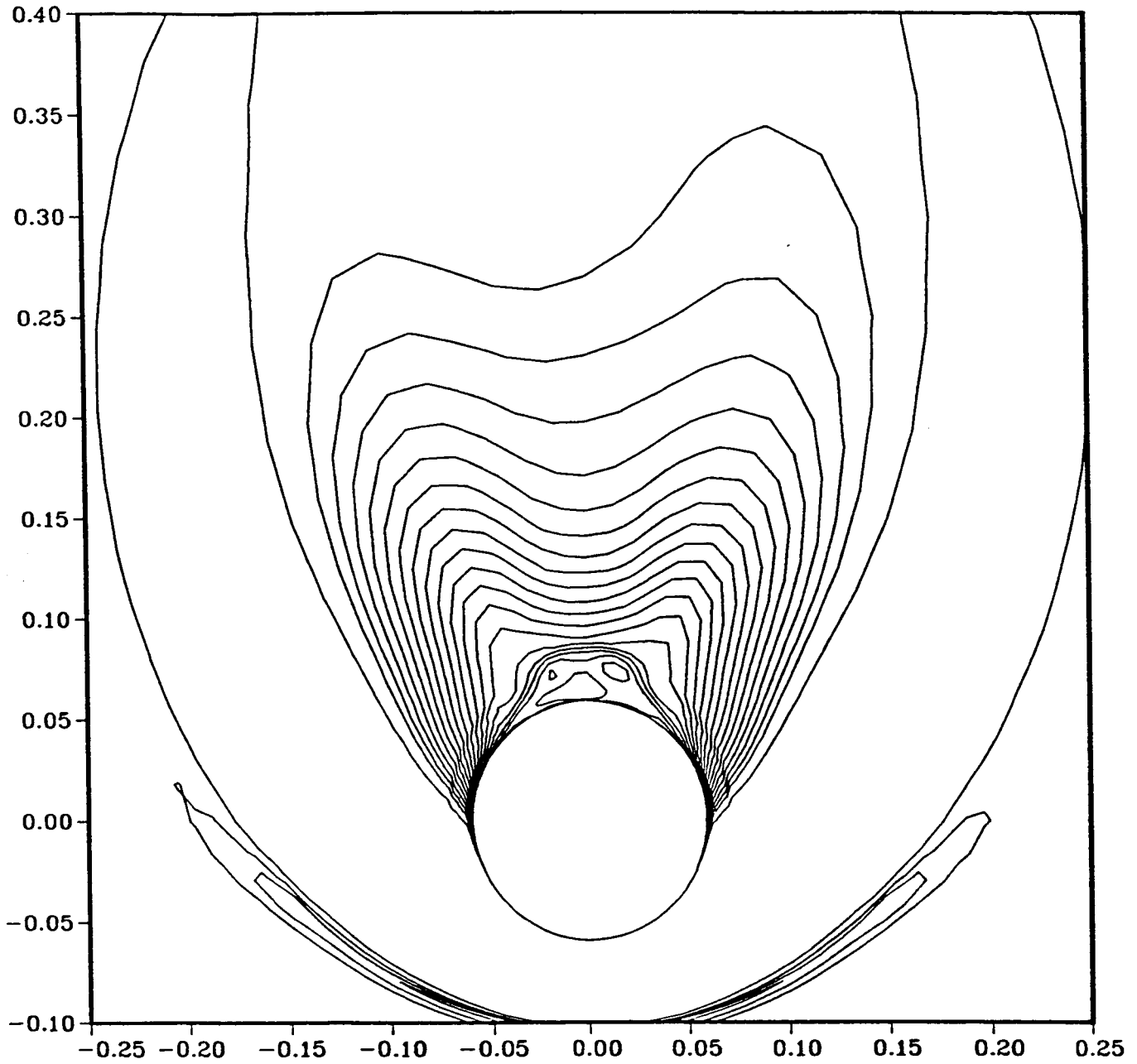
$M_\infty = 2.94$ $\alpha = 34.00$ $Re = 1.372 \cdot 10^7$ $X = 0.4000$

Fig. 18_d Marching solution. Density Contours at different stations,
 $\alpha = 34^\circ$.

PLOT 1 19.07.26 WED 5 FEB, 1986 JOB-CPL0T , NASA Ames DISPLA 9.0

DENSITY CONTOURS

MARCHING ON 7.5 DEG. CONE



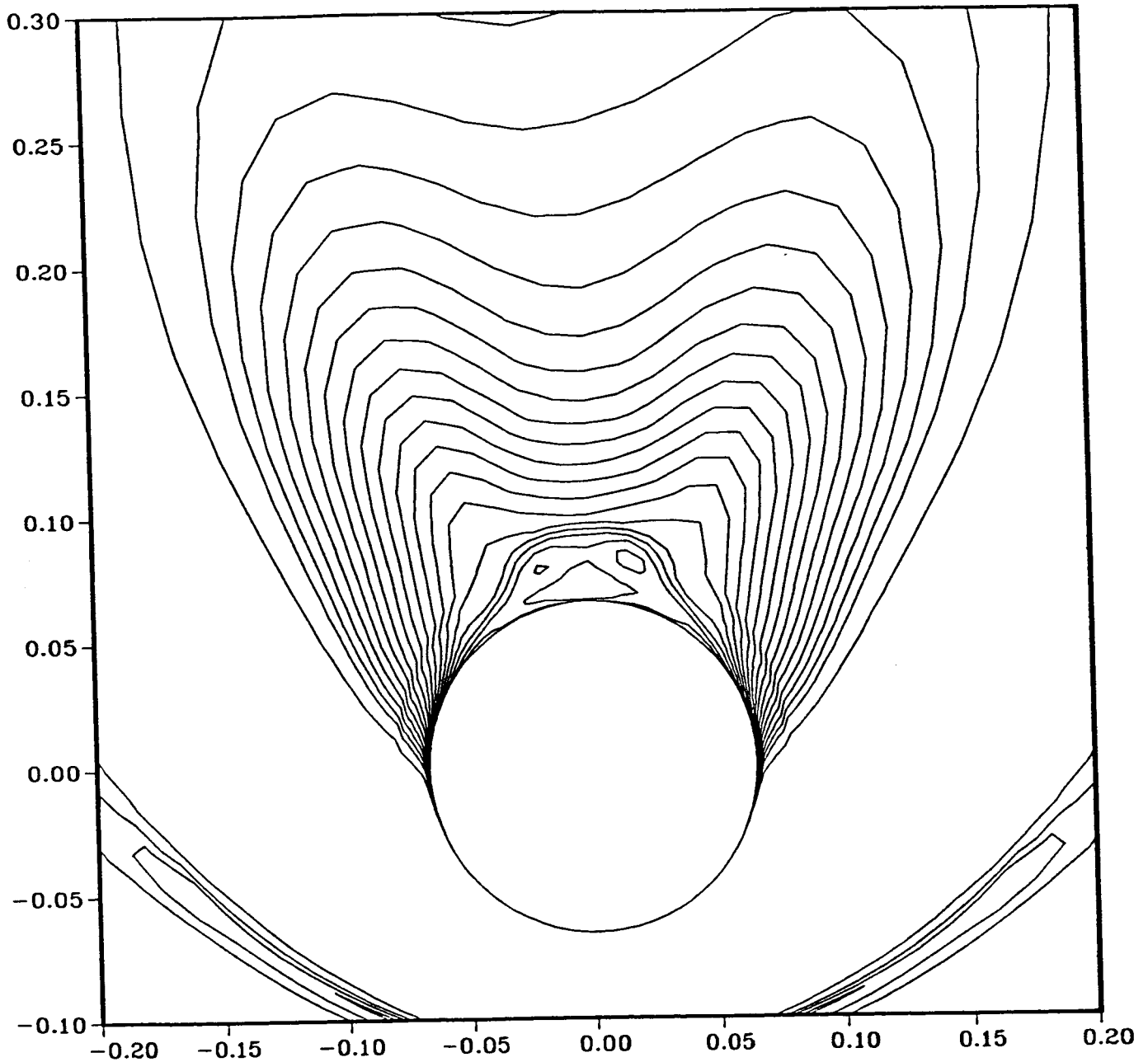
$M_\infty = 2.94$ $\alpha = 34.00$ $Re = 1.372 \cdot 10^7$ $X = 0.4500$

Fig. 18_e - Marching solution. Density Contours at different stations,
 $\alpha = 34^\circ$.

PL01 J 20:16.05 MED 5 FEB, 1966 JOB-CPL01 , NASA Ames DISPLA 9.0.

DENSITY CONTOURS

MARCHING ON 7.5 DEG. CONE



$M_\infty = 2.94$ $\alpha = 34.00$ $Re = 1.372 \cdot 10^7$ $X = 0.5000$

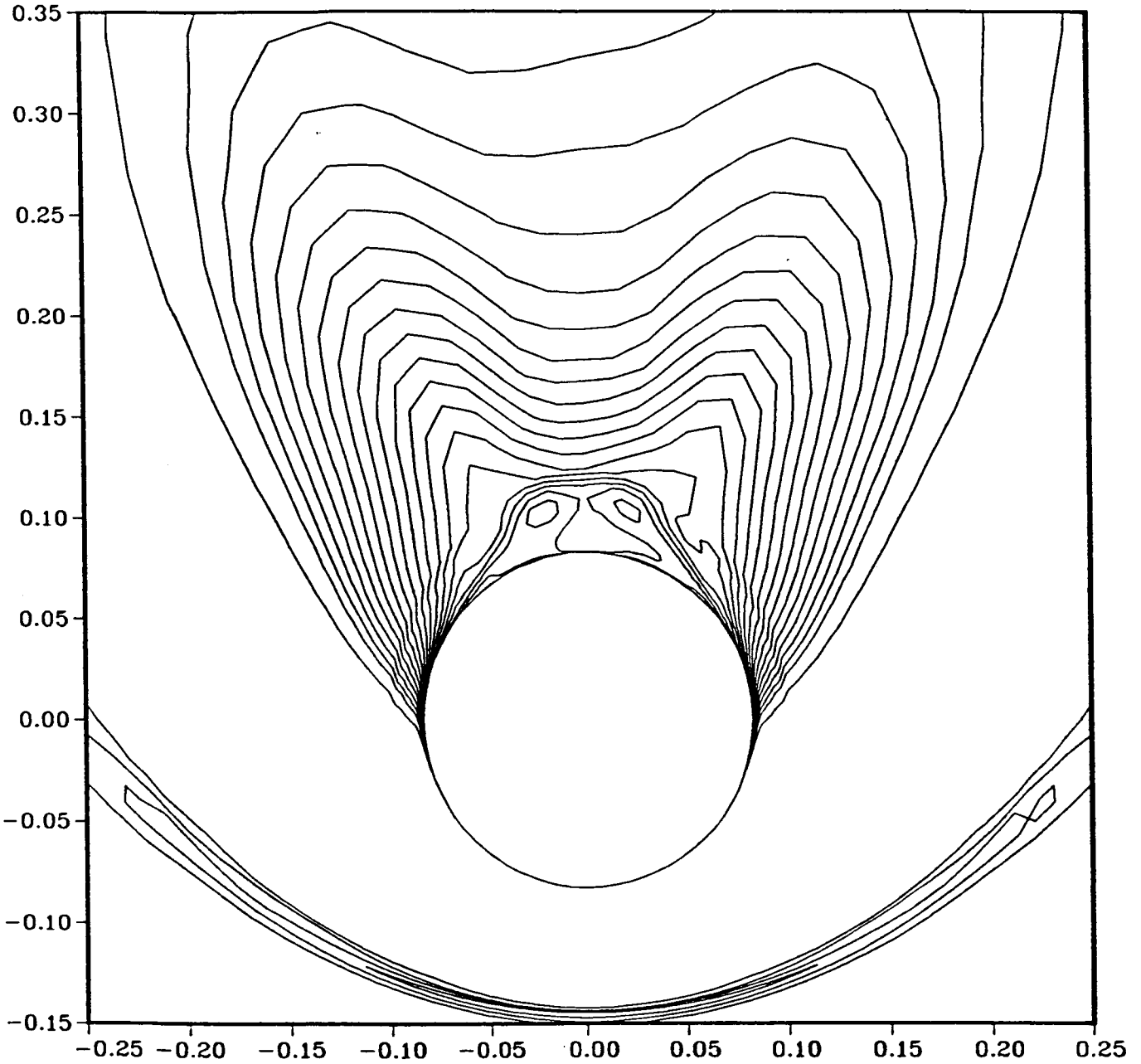
Fig. 18_f - Marching solution. Density Contours at different stations,
 $\alpha = 34^\circ$.

PLOT 1 21.07.28 MED 5 FEB, 1986 JOB-CPLOT , NASA Ames DISPLA 9.0.

ORIGINAL PAGE IS
OF POOR QUALITY

DENSITY CONTOURS

MARCHING ON 7.5 DEG. CONE



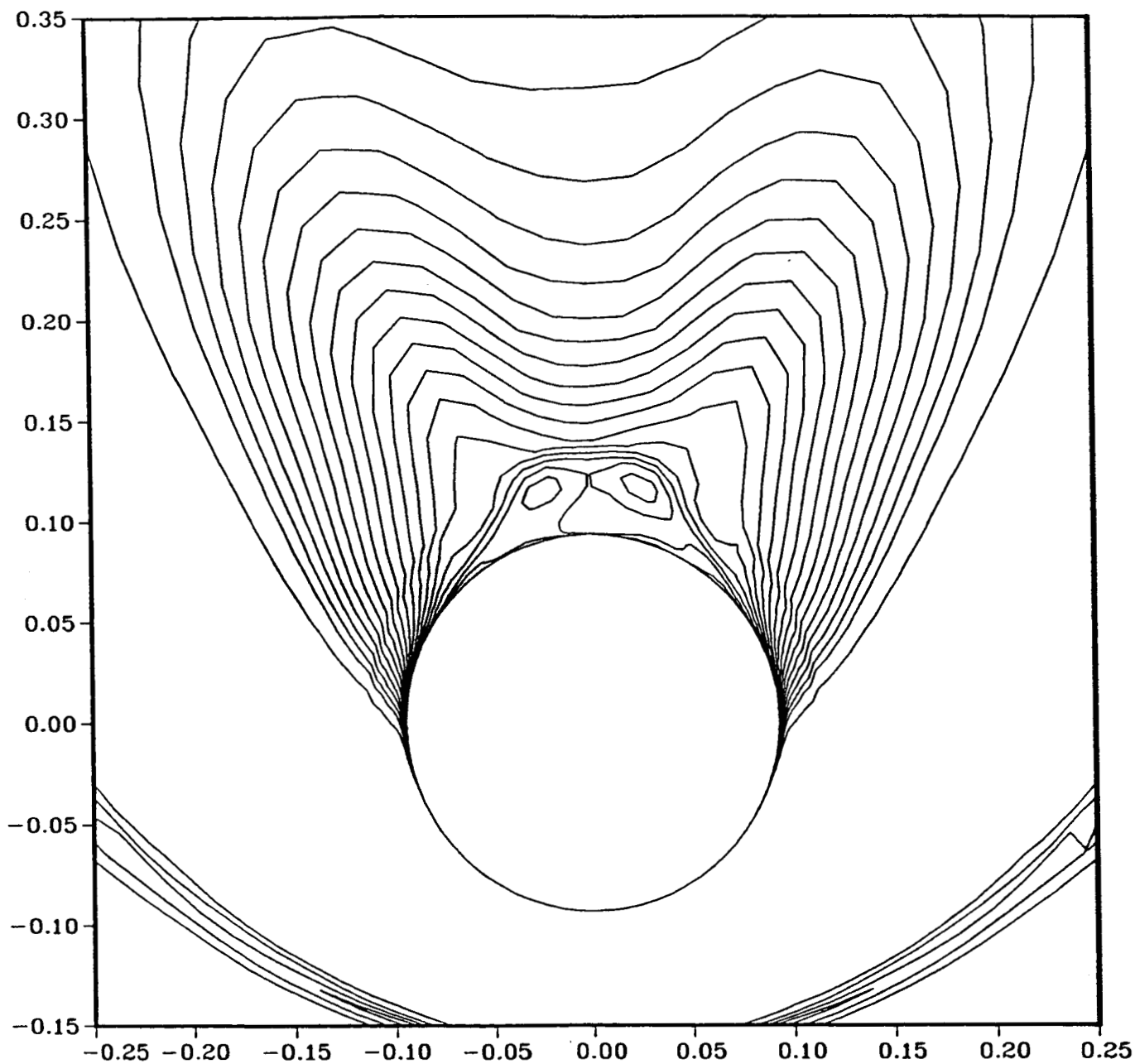
$M_\infty = 2.94$ $\alpha = 34.00$ $Re = 1.372 \cdot 10^7$ $X = 0.6300$

Fig. 18_g - Marching solution. Density Contours at different stations,
 $\alpha = 34^\circ$.

22.25.21 MED 5 FEB, 1986 JOB-CPL0T , NISA PAGES DISSPLA 9.0 PLOT 1

DENSITY CONTOURS

MARCHING ON 7.5 DEG. CONE

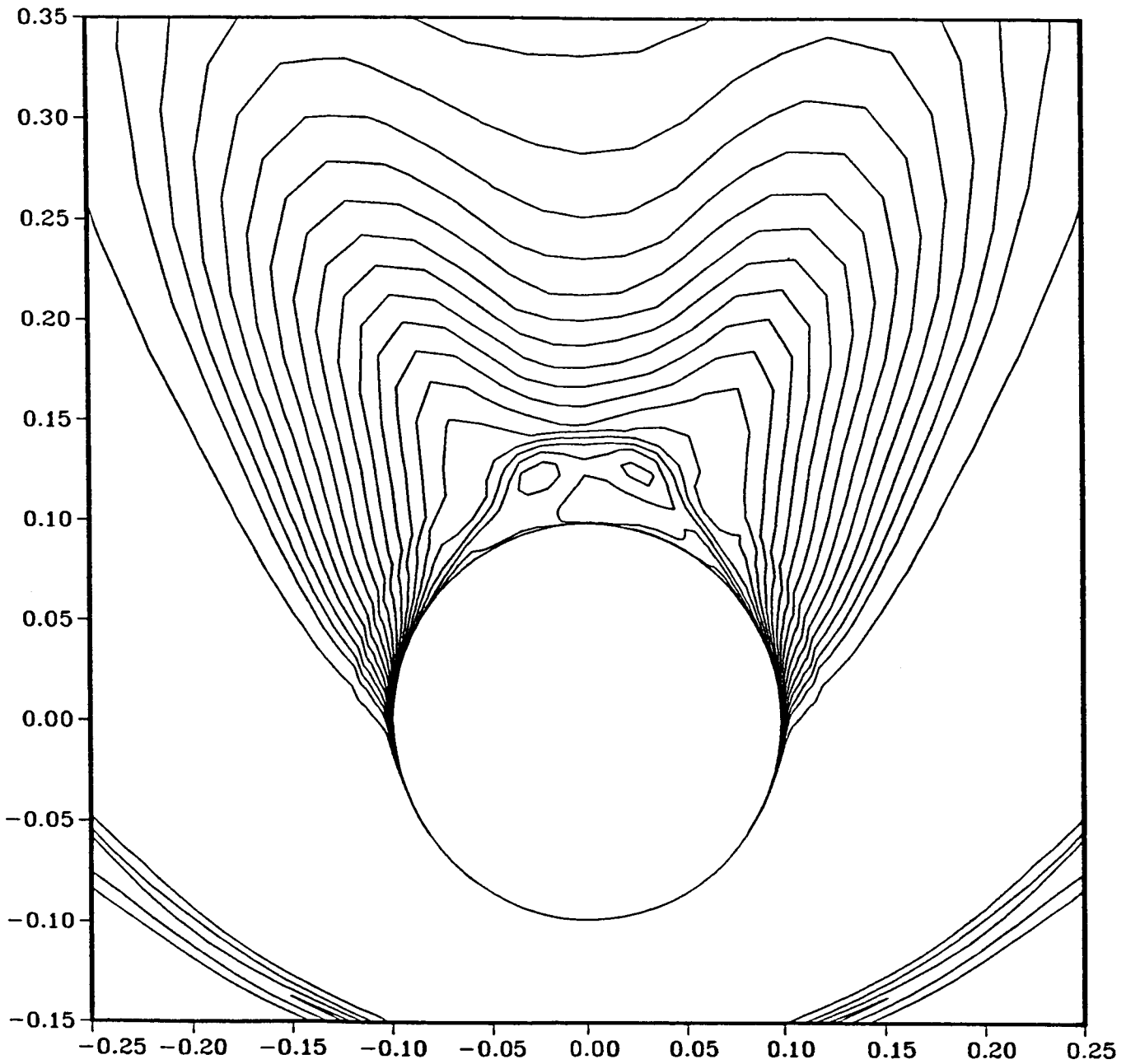


$M_\infty = 2.94$ $\alpha = 34.00$ $Re = 1.372 \cdot 10^7$ $X = 0.7100$

Fig. 18_h - Marching solution. Density Contours at different stations,
 $\alpha = 34^\circ$.

DENSITY CONTOURS

MARCHING ON 7.5 DEG. CONE

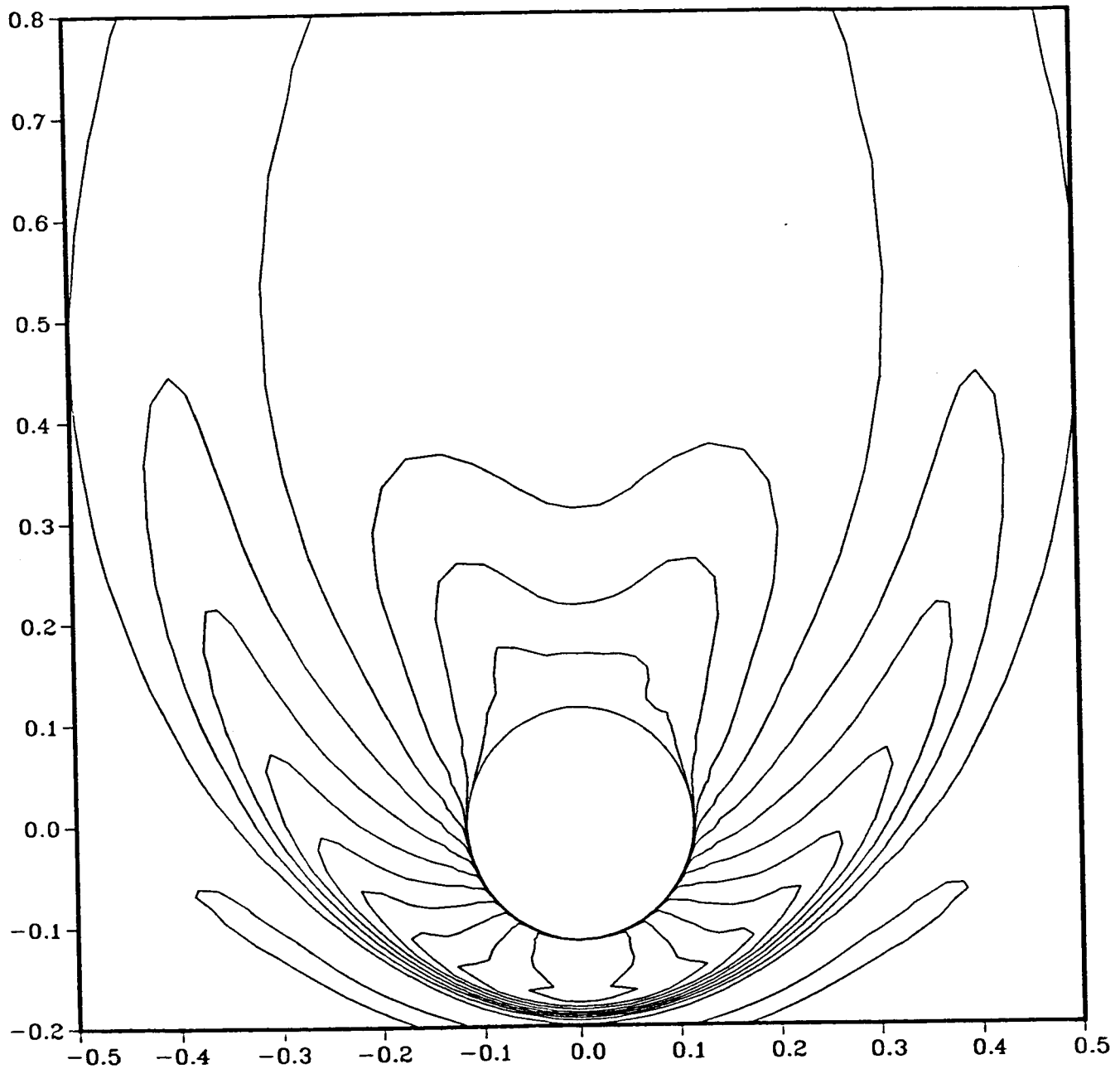


$M_\infty = 2.94$ $\alpha = 34.00$ $Re = 1.372 \cdot 10^7$ $X = 0.7500$

Fig. 18:- Marching solution. Density Contours at different stations,
 $\alpha = 34^\circ$.

DENSITY CONTOURS

cone 7.5 DEG. MARCHING



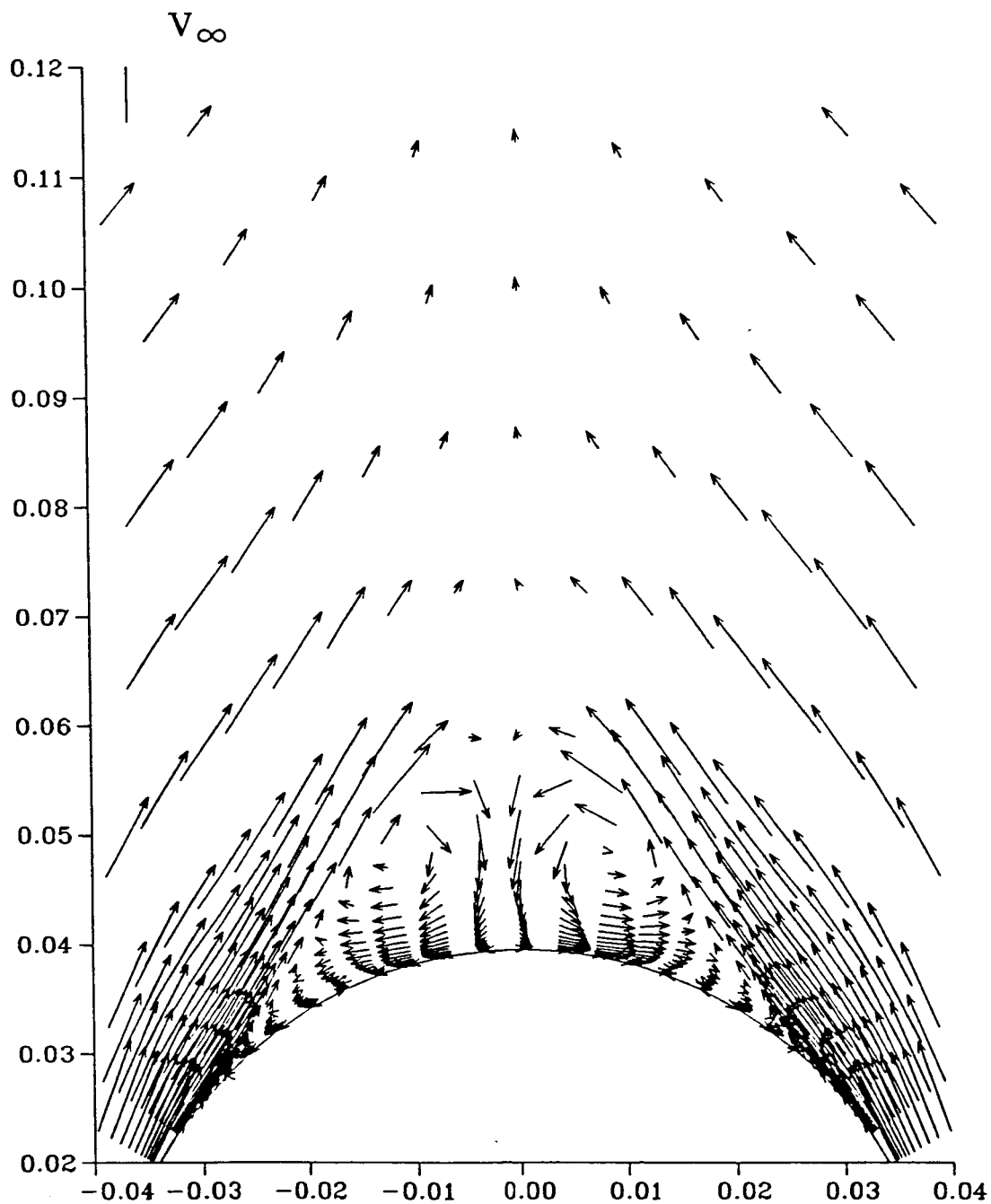
$M_\infty = 2.94$ $\alpha = 34.00$ $Re = 1.372 \cdot 10^7$ $X = 0.8700$

Fig. 18_j - Marching solution. Density Contours at different stations,
 $\alpha = 34^\circ$.

PUOT 2 12.19.34 MED 5 FEB, 1986 JOB-DRAWPLOT, MASH FILES UISSPLA 9.0

VELOCITY VECTORS

cone 7.5 DEG. MARCHING

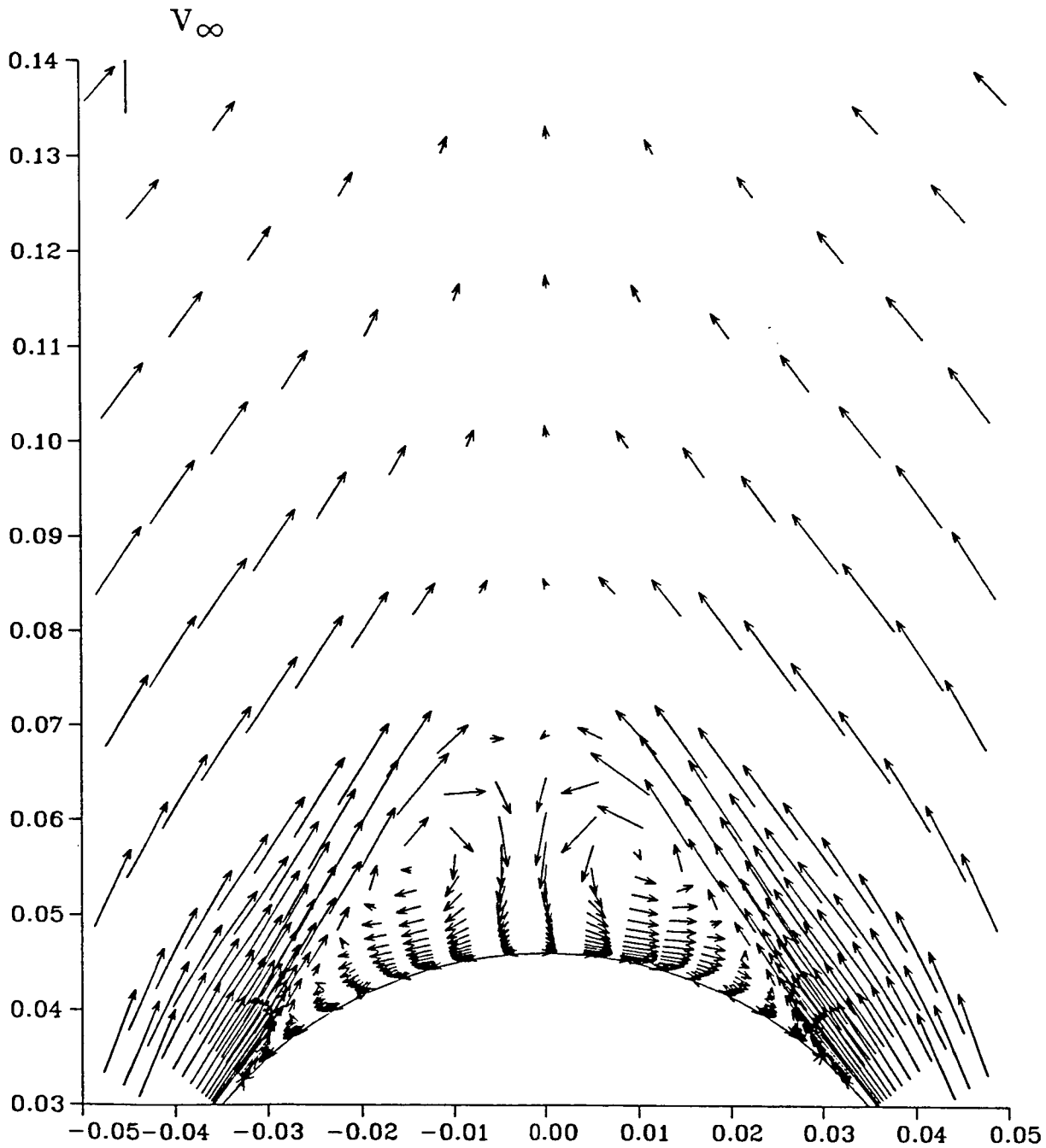


$M_\infty = 2.94$ $\alpha = 34.00$ $Re = 1.372 \cdot 10^7$ $X = 0.3000$

Fig. 19 - Marching solution. Velocity vectors at different stations,
 $\alpha = 34^\circ$.

VELOCITY VECTORS

cone 7.5 DEG. MARCHING

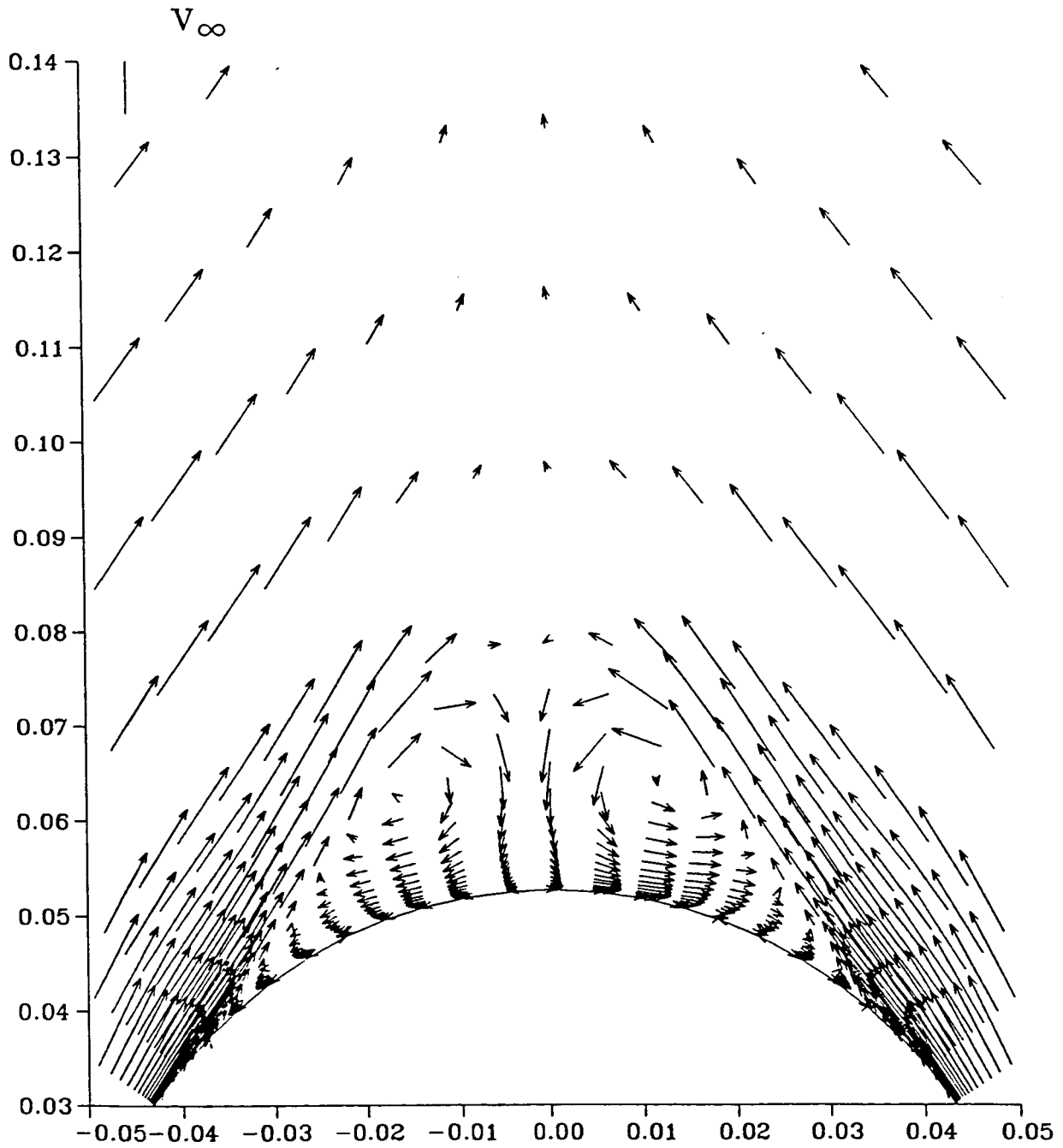


$M_\infty = 2.94$ $\alpha = 34.00$ $Re = 1.372 \cdot 10^7$ $X = 0.3500$

Fig. 19_b - Marching solution. Velocity vectors at different stations,
 $\alpha = 34^\circ$.

VELOCITY VECTORS

cone 7.5 DEG. MARCHING



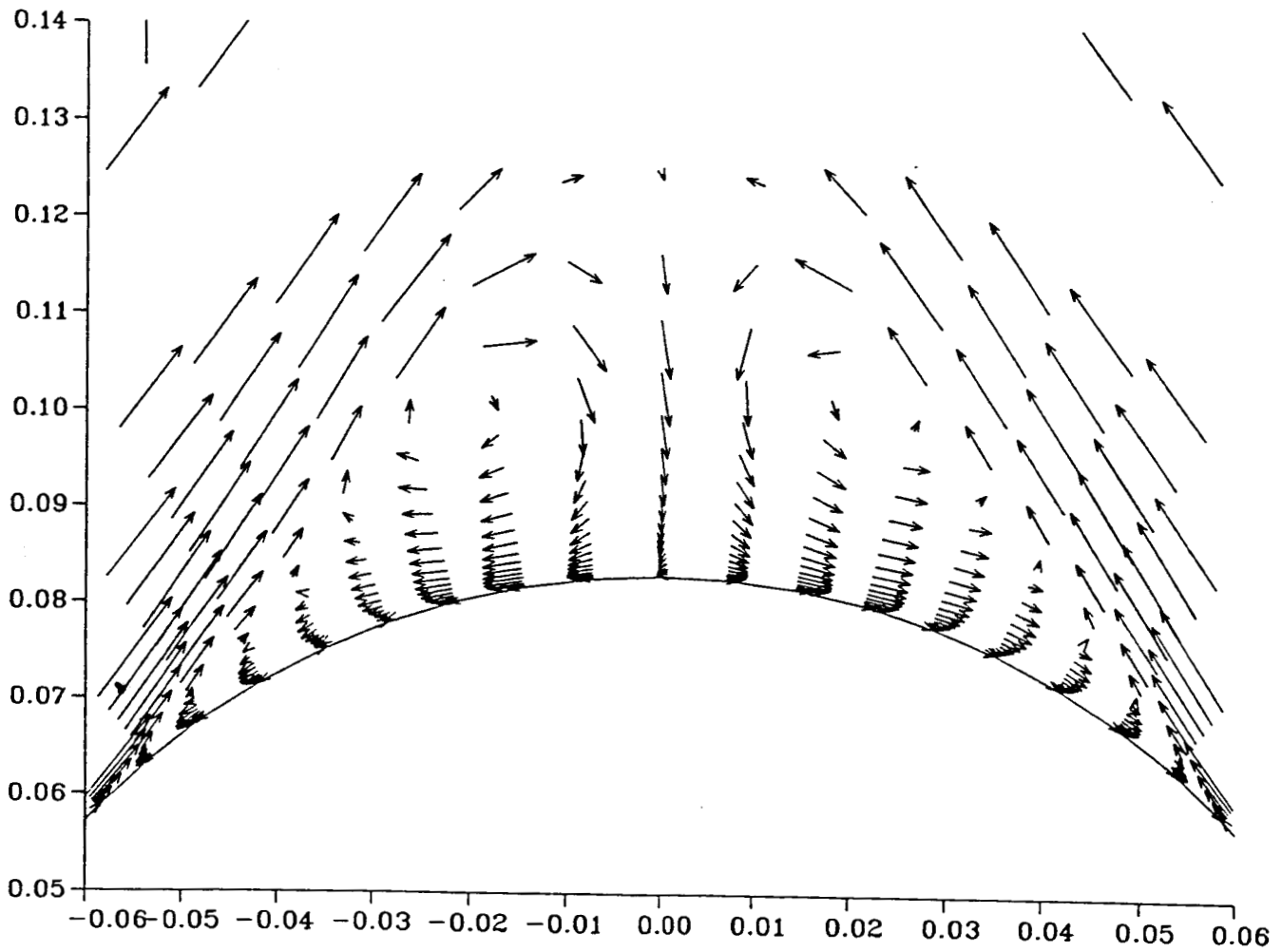
$M_\infty = 2.94$ $\alpha = 34.00$ $Re = 1.372 \cdot 10^7$ $X = 0.4000$

Fig. 19_c - Marching solution. Velocity vectors at different stations, $\alpha = 34^\circ$.

15.52.03 MCD 5 FEB, 1966 JOB-DRAWPLOT, MFISA FMES DISSPLA 9.0 PLOT 1

VELOCITY VECTORS

V_∞ cone 7.5 DEG. MARCHING

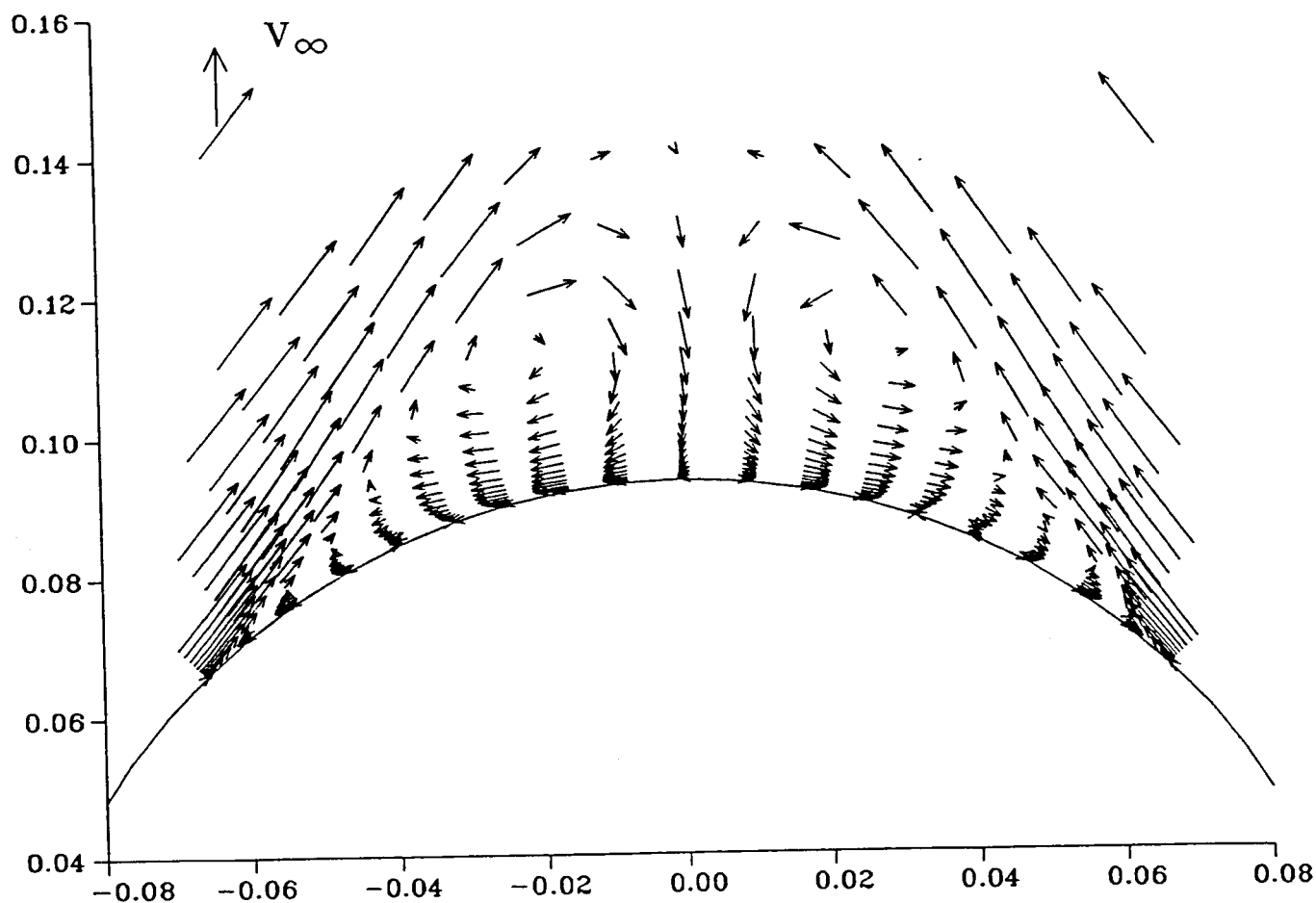


$M_\infty = 2.94$ $\alpha = 34.00$ $Re = 1.372 \cdot 10^7$ $X = 0.6300$

Fig. 19_d - Marching solution. Velocity vectors at different stations,
 $\alpha = 34^\circ$.

ORIGINAL PAGE IS
OF POOR QUALITY

VELOCITY VECTORS cone 7.5 DEG. MARCHING



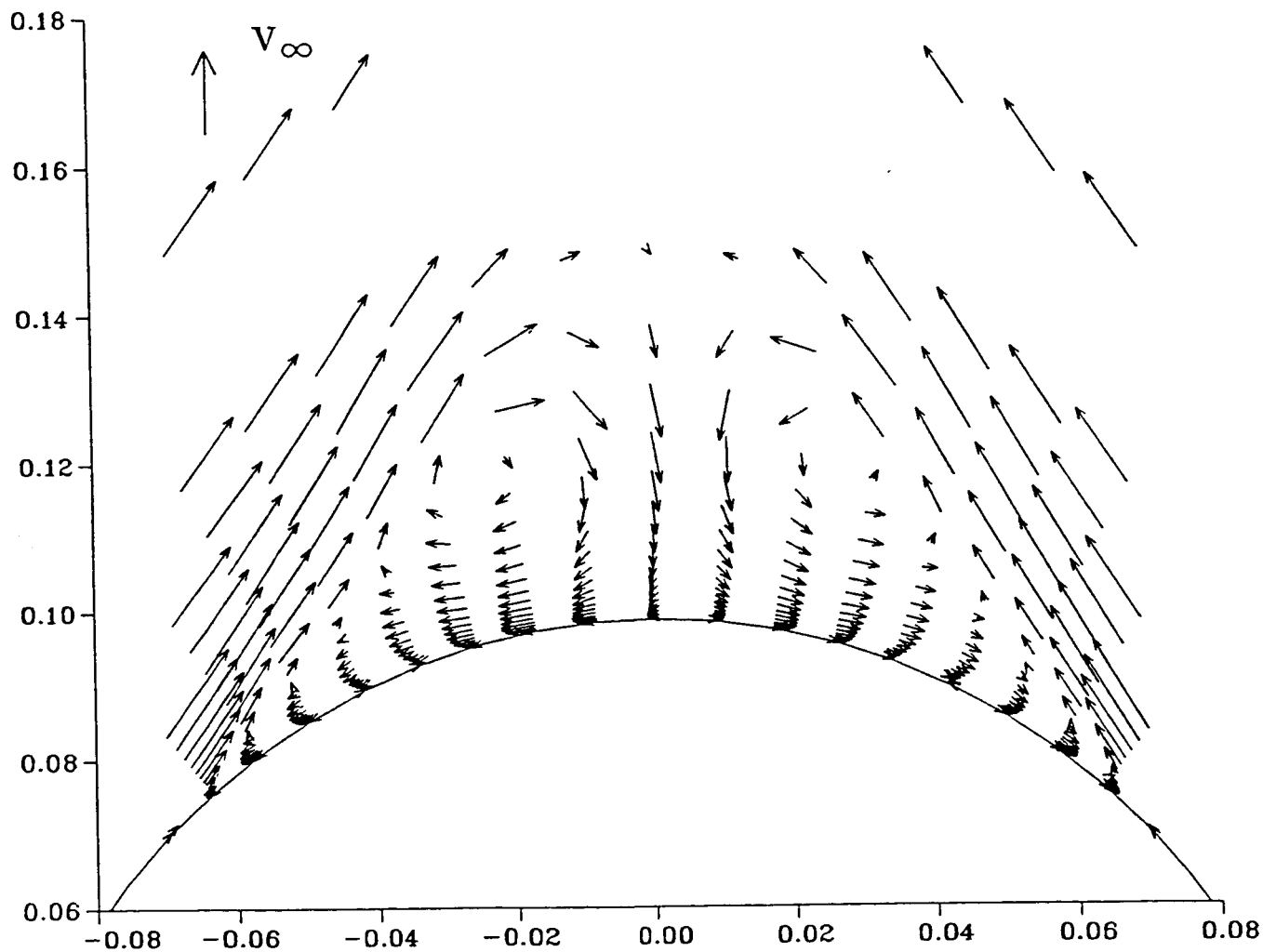
$M_\infty = 2.94$ $\alpha = 34.00$ $Re = 1.372 \cdot 10^7$ $X = 0.7100$

Fig. 19_e - Marching solution. Velocity vectors at different stations,
 $\alpha = 34^\circ$.

PL01 J 10.16.14 WED 5 FEB, 1986 JOB-DRAWPLOT, NASA AMLS DISPLA 9.0

VELOCITY VECTORS

cone 7.5 DEG. MARCHING



$M_\infty = 2.94$ $\alpha = 34.00$ $Re = 1.372 \cdot 10^7$ $X = 0.7500$

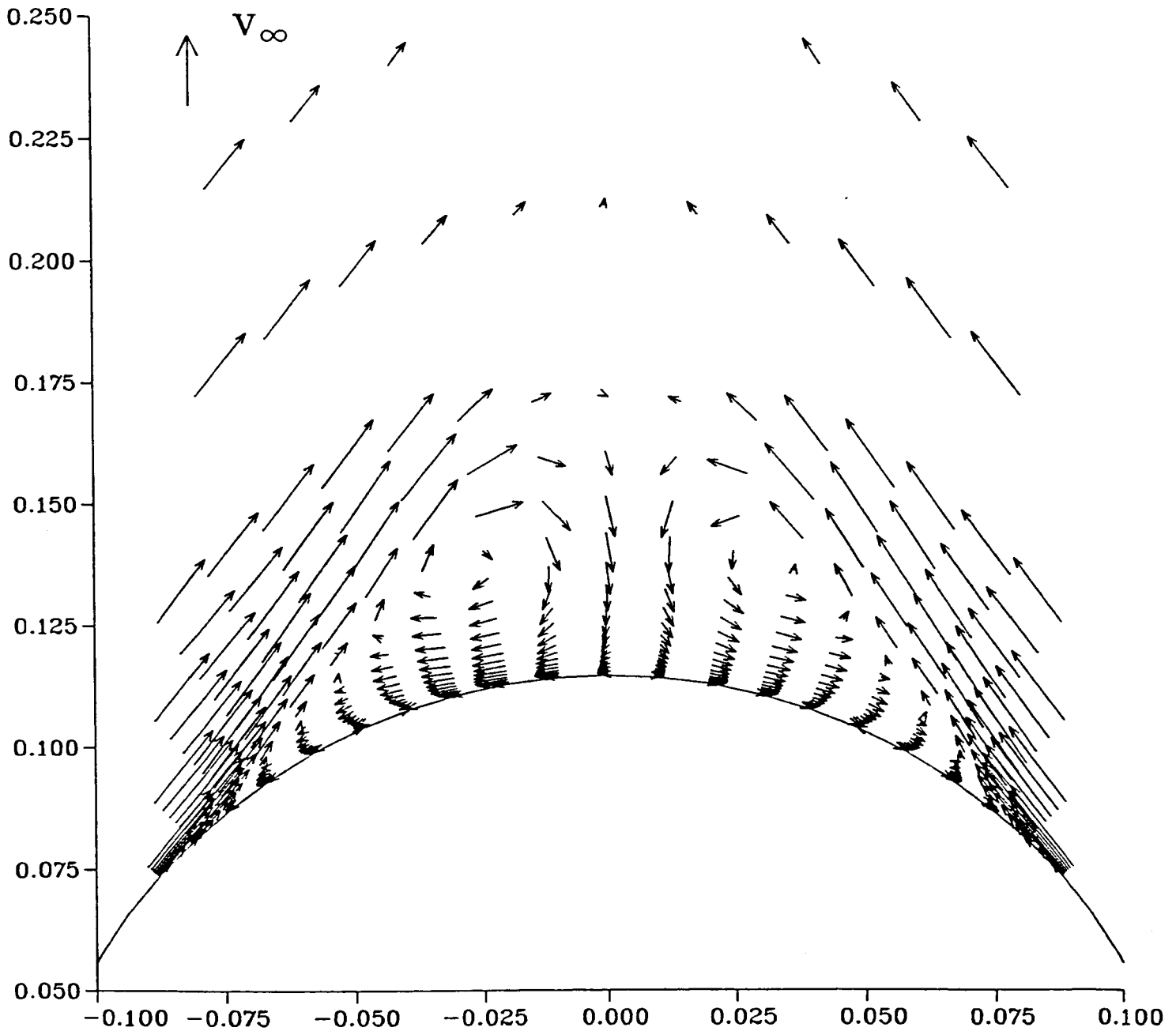
Fig. 19 - Marching solution. Velocity vectors at different stations,
 $\alpha = 34^\circ$.

FLUENT 11.02.06 WED 5 FEB, 1986 JOB=URVFLOI, NISHI FMLES DISJOINT 9.0

ORIGINAL PAGE IS
OF POOR QUALITY

VELOCITY VECTORS

cone 7.5 DEG. MARCHING



$M_\infty = 2.94$ $\alpha = 34.00$ $Re = 1.372 \cdot 10^7$ $X = 0.8700$

Fig. 19_g - Marching solution. Velocity vectors at different stations,
 $\alpha = 34^\circ$.

GRID PLOT

ORIGINAL PAGE IS
OF POOR QUALITY

OGIVE-CYLINDER GRID

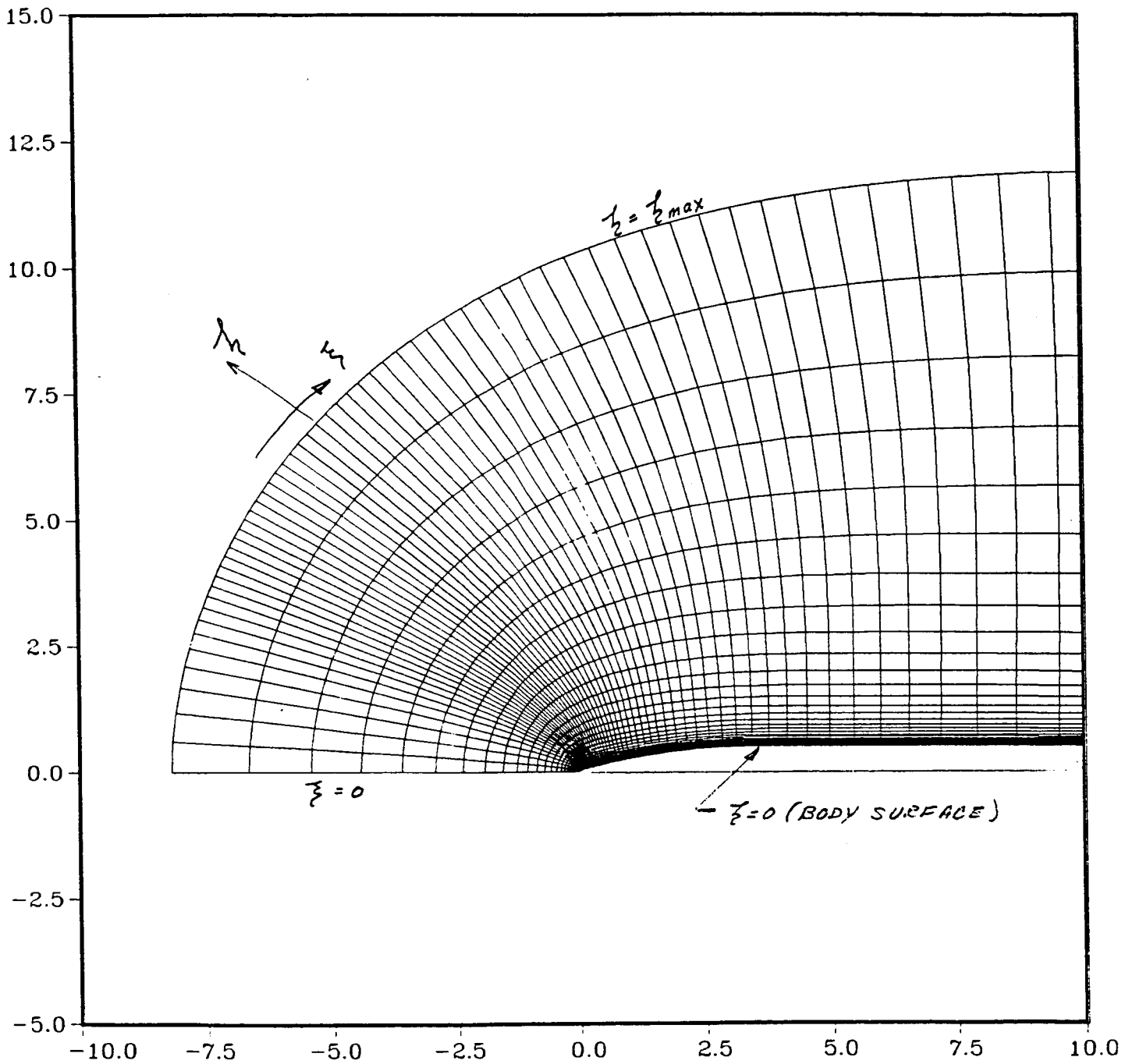


Fig. 20 - Computational grid and coordinates.

DENSITY

CONTOUR LEVELS

- 0.95000
- 0.95250
- 0.95500
- 0.95750
- 0.96000
- 0.96250
- 0.96500
- 0.96750
- 0.97000
- 0.97250
- 0.97500
- 0.97750
- 0.98000
- 0.98250
- 0.98500
- 0.98750
- 0.99000
- 0.99250

200

10.00 DEG

2.00x10⁺⁵

30x121x50

MACH

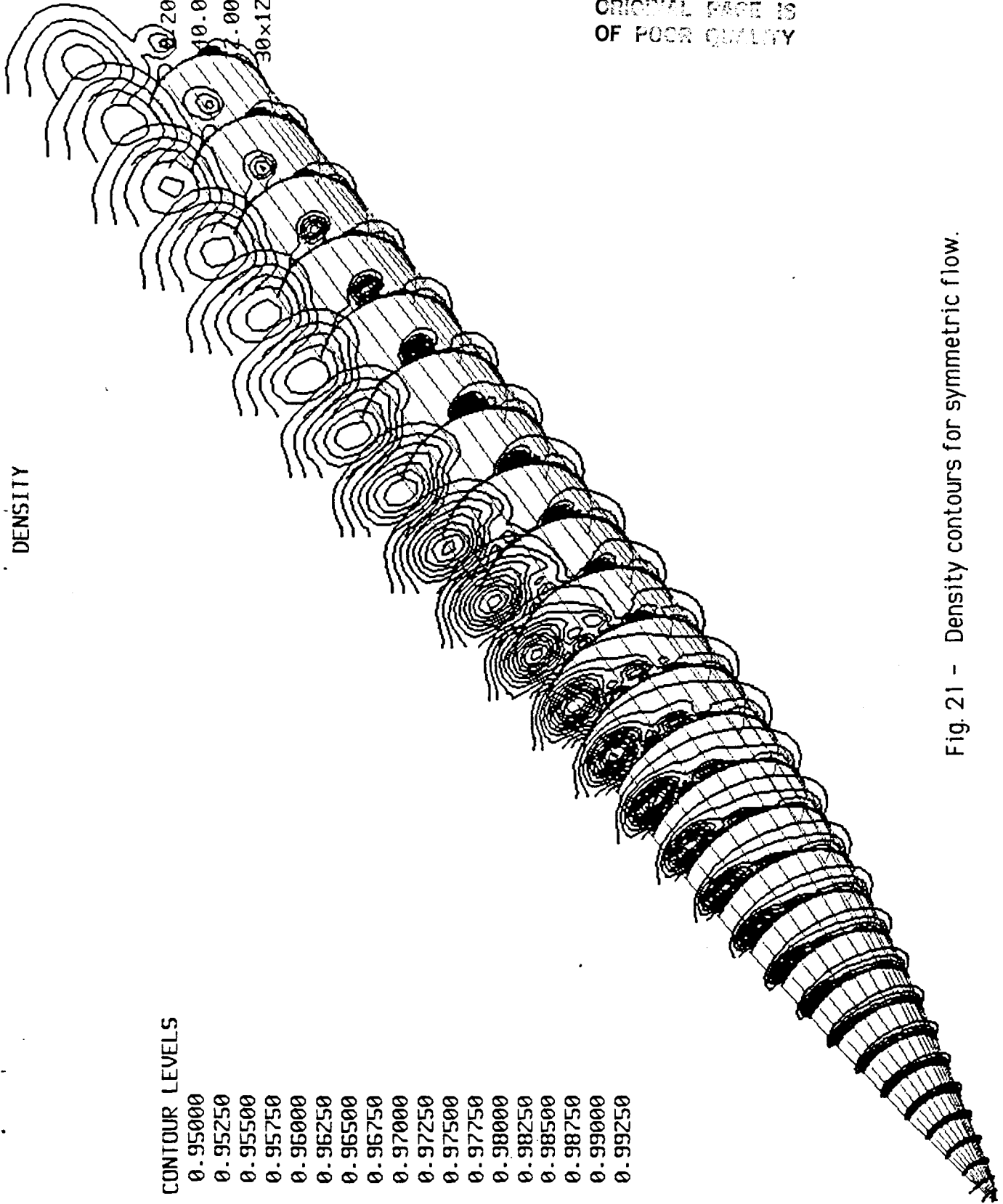
ALPHA

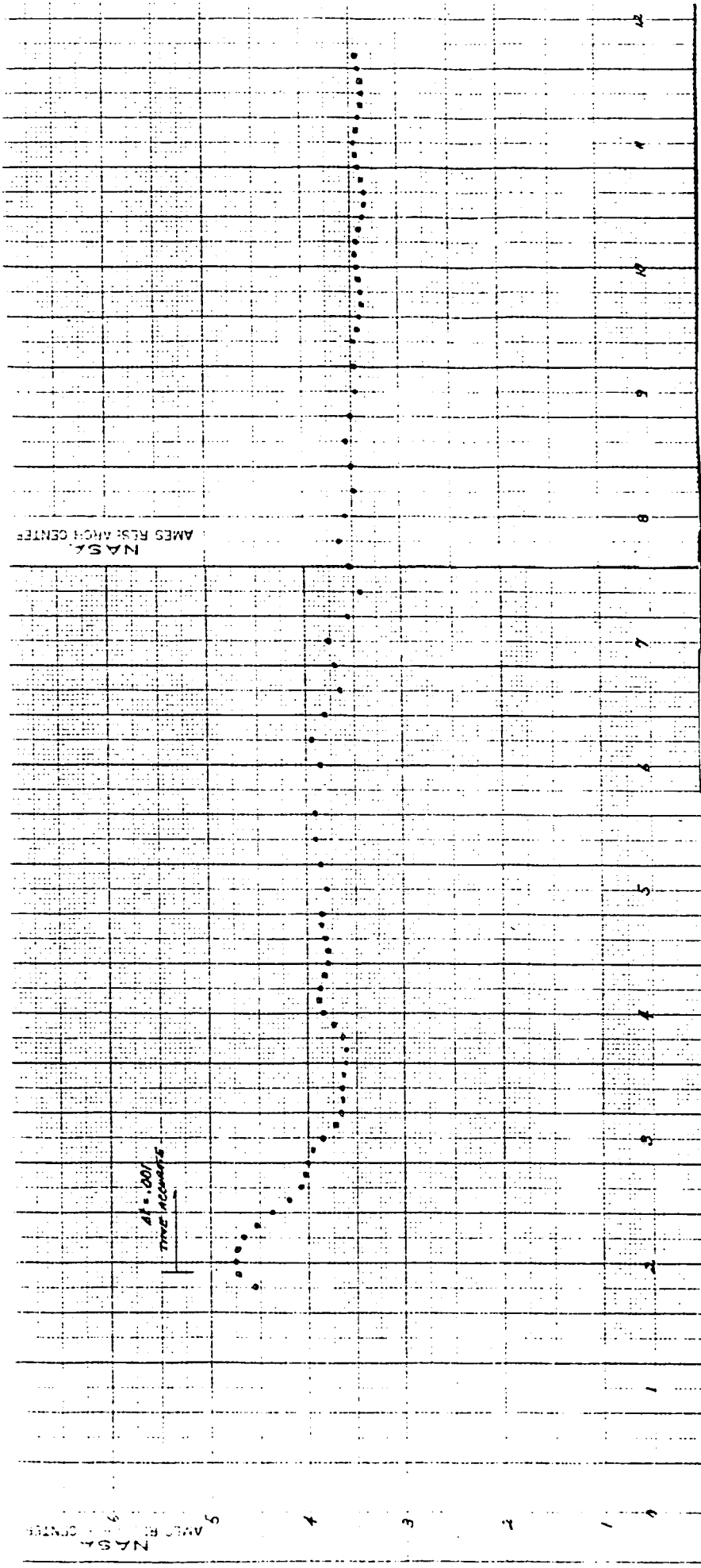
Re

GRID

ORIGINAL PAGE IS
OF POOR QUALITY

Fig. 21 - Density contours for symmetric flow.





ORIGINAL PAGE IS
OF POOR QUALITY

Fig 22 - Normal force coefficient history, symmetric flow.

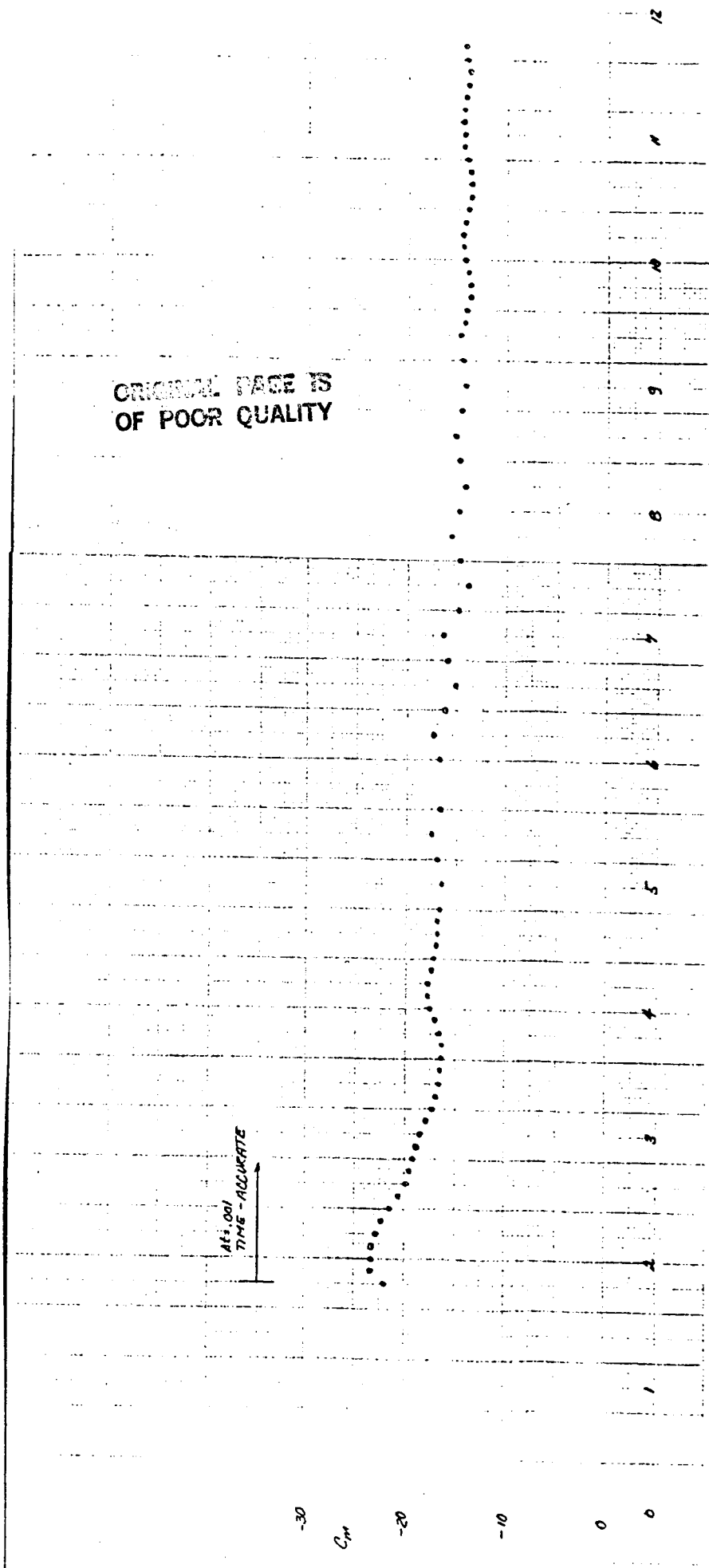


Fig. 23 - Pitching moment coefficient history, symmetric flow.

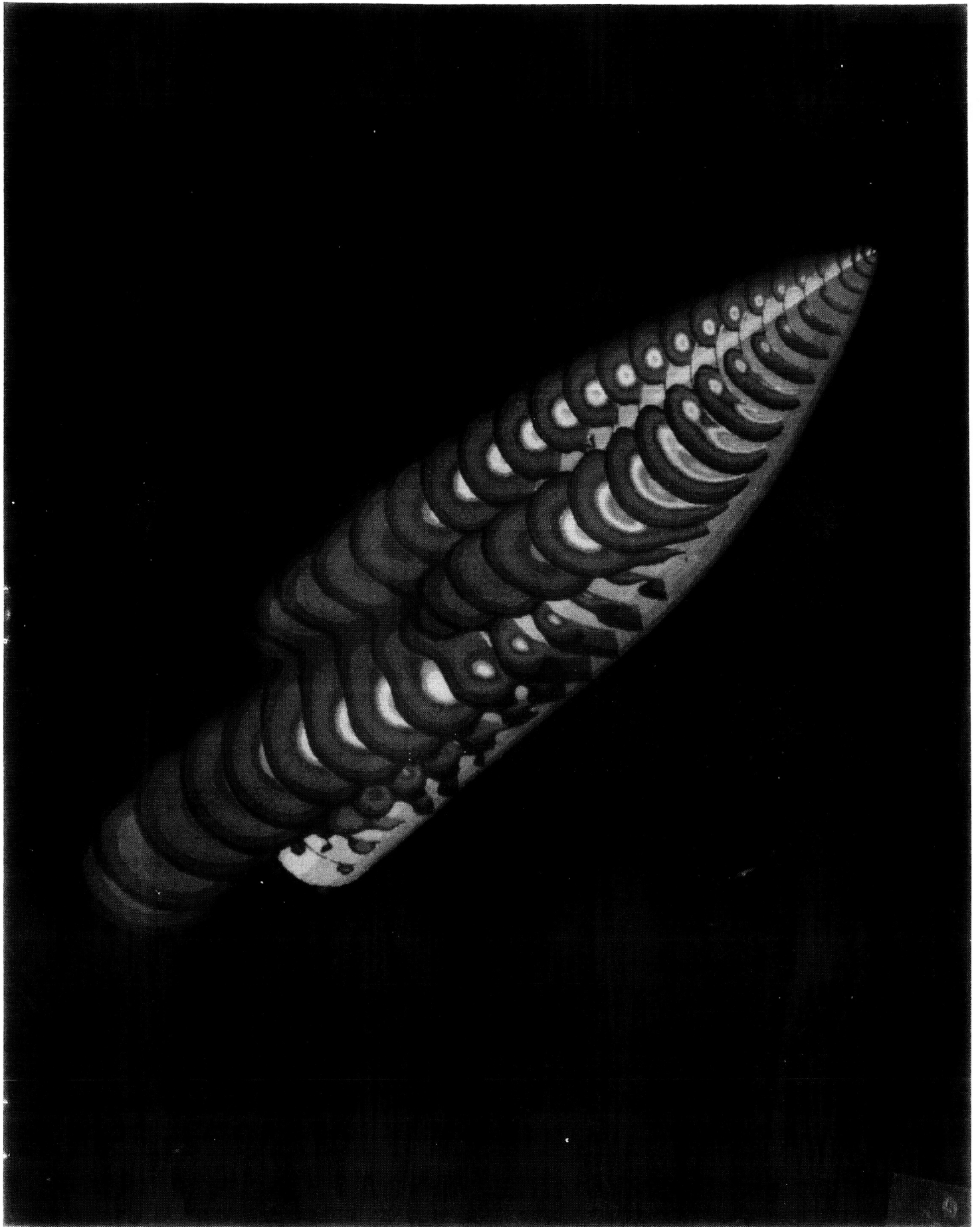


Fig. 24 - Density contours showing vortex asymmetry.

ORIGINAL PAGE
COLOR PHOTOGRAPH

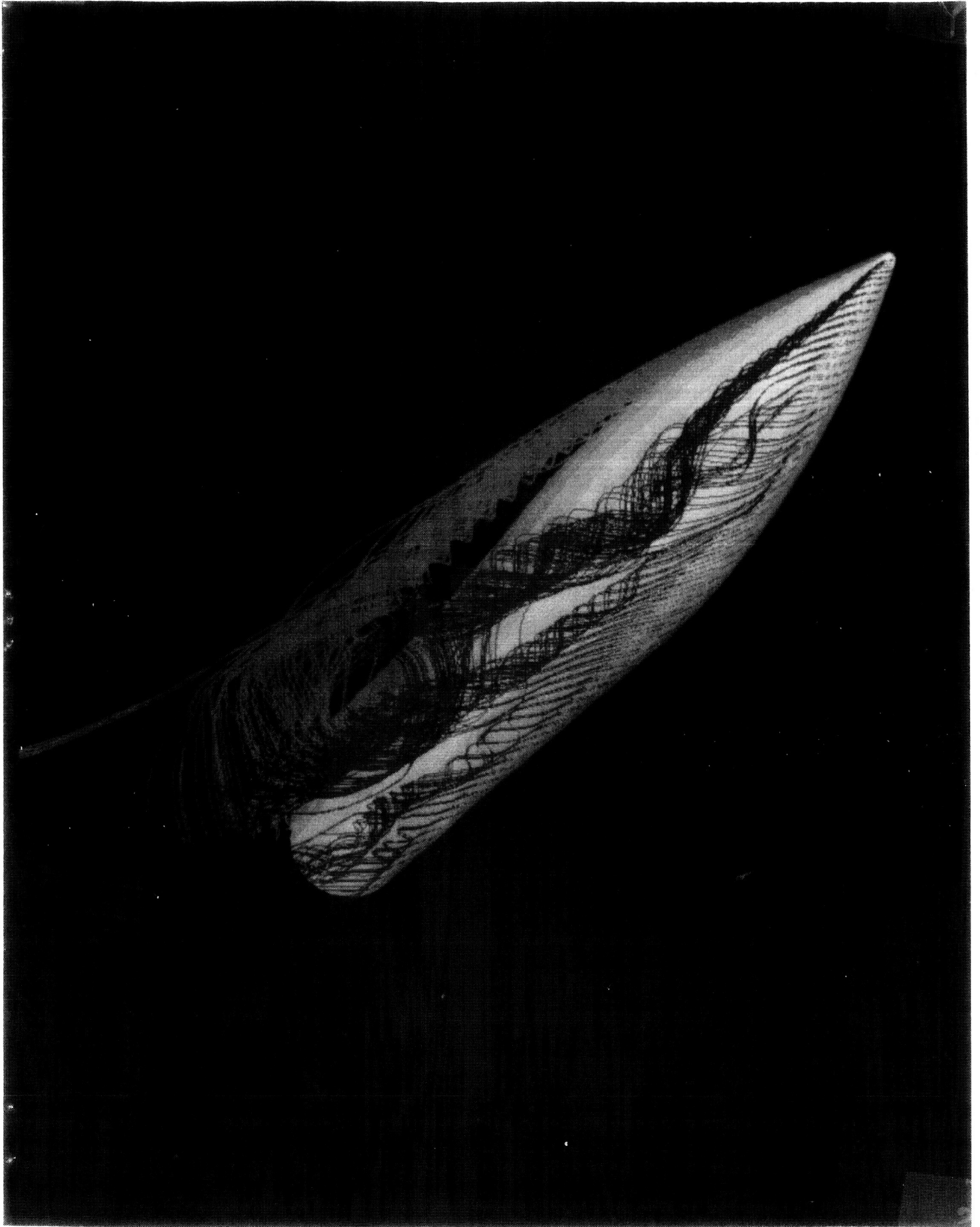


Fig. 25 - Partical traces above leeward side, showing vortex asymmetry.

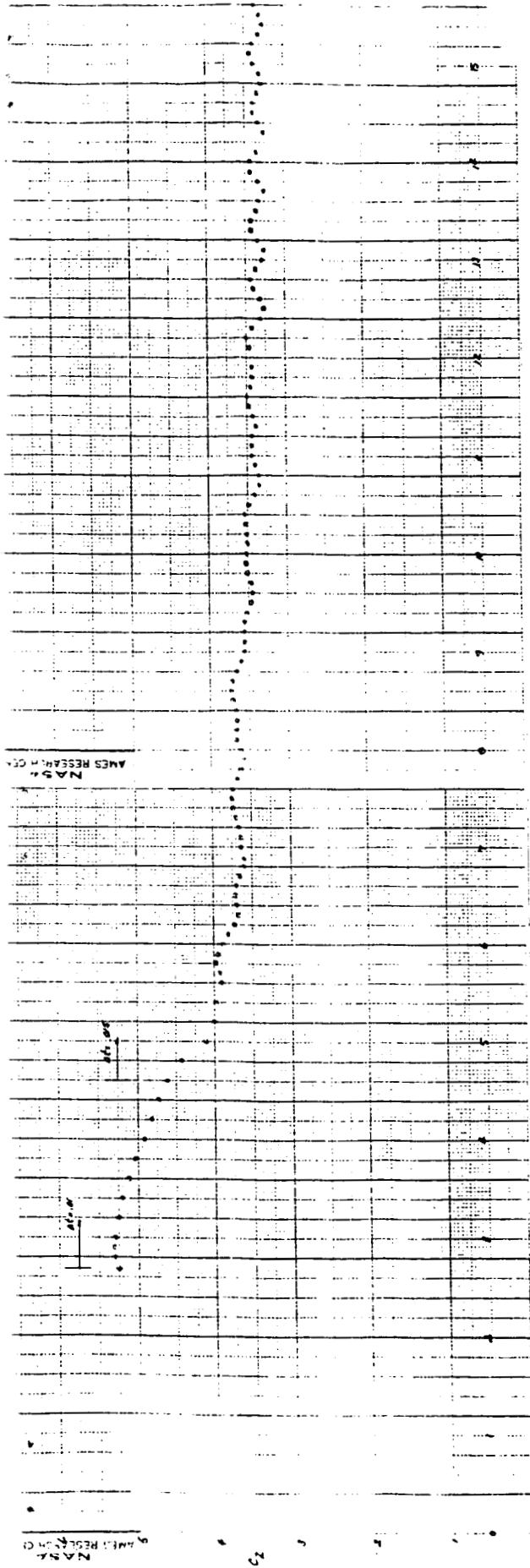


Fig. 26 - Normal force coefficient history, asymmetric case.

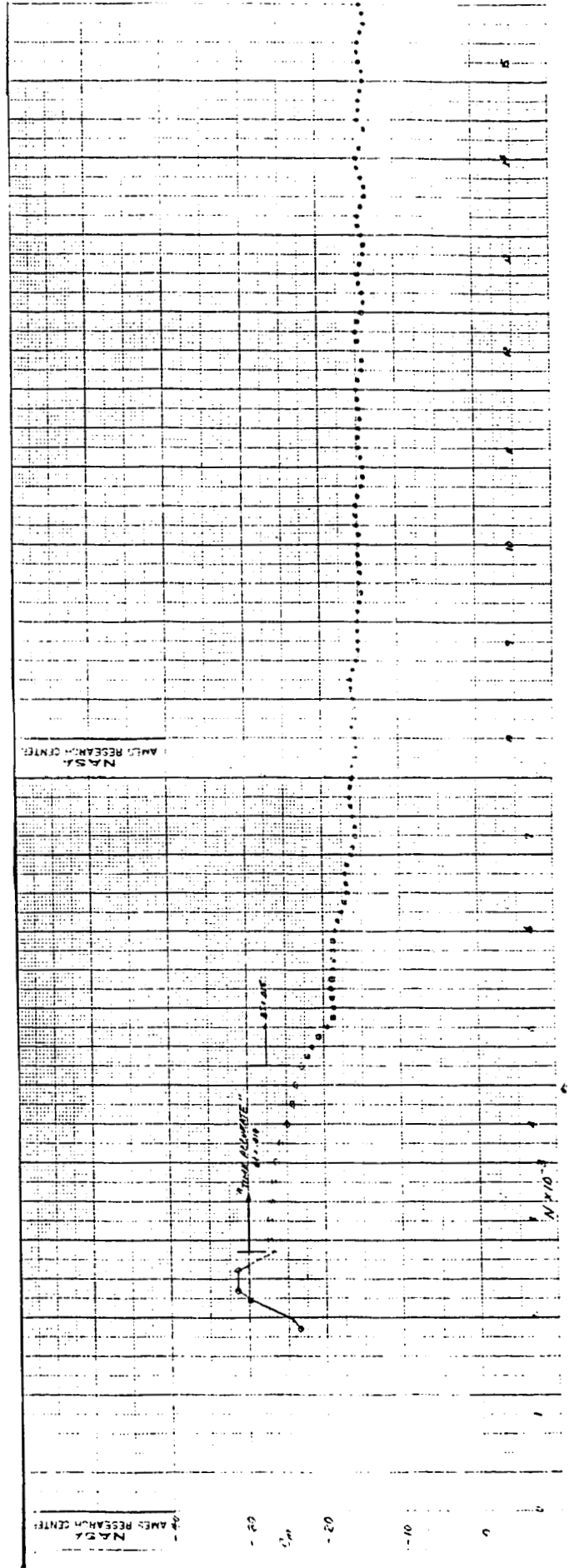


Fig. 27 - Pitching moment coefficient history, asymmetric case.

ORIGINAL PAGE IS
OF POOR QUALITY

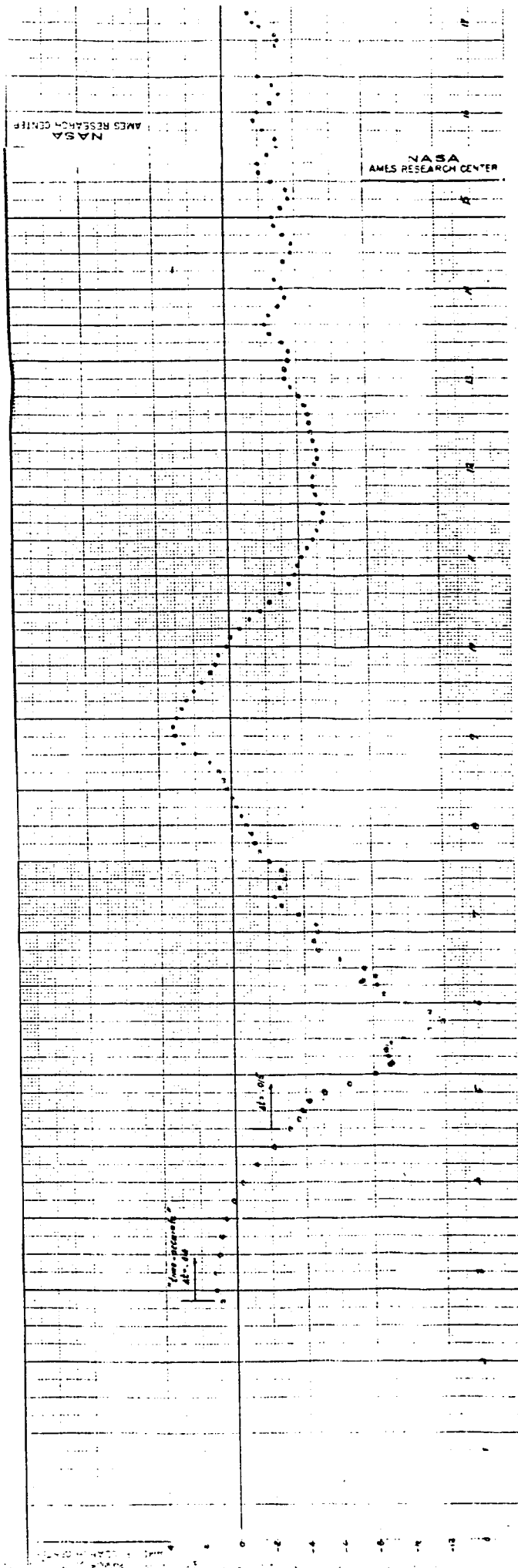


Fig. 28 - Yawing moment history, asymmetric case.

DENSITY

seper 4700

CONTOUR
0.95000
0.95250
0.95500
0.95750
0.96000
0.96250
0.96500
0.96750
0.97000
0.97250
0.97500
0.97750
0.98000
0.98250
0.98500
0.98750
0.99000
0.99250

0.200 MACH
40.00 DEG ALPHA
2.00x10**5 Re
30x121x50 GRID

ORIGINAL PAGE IS
OF POOR QUALITY

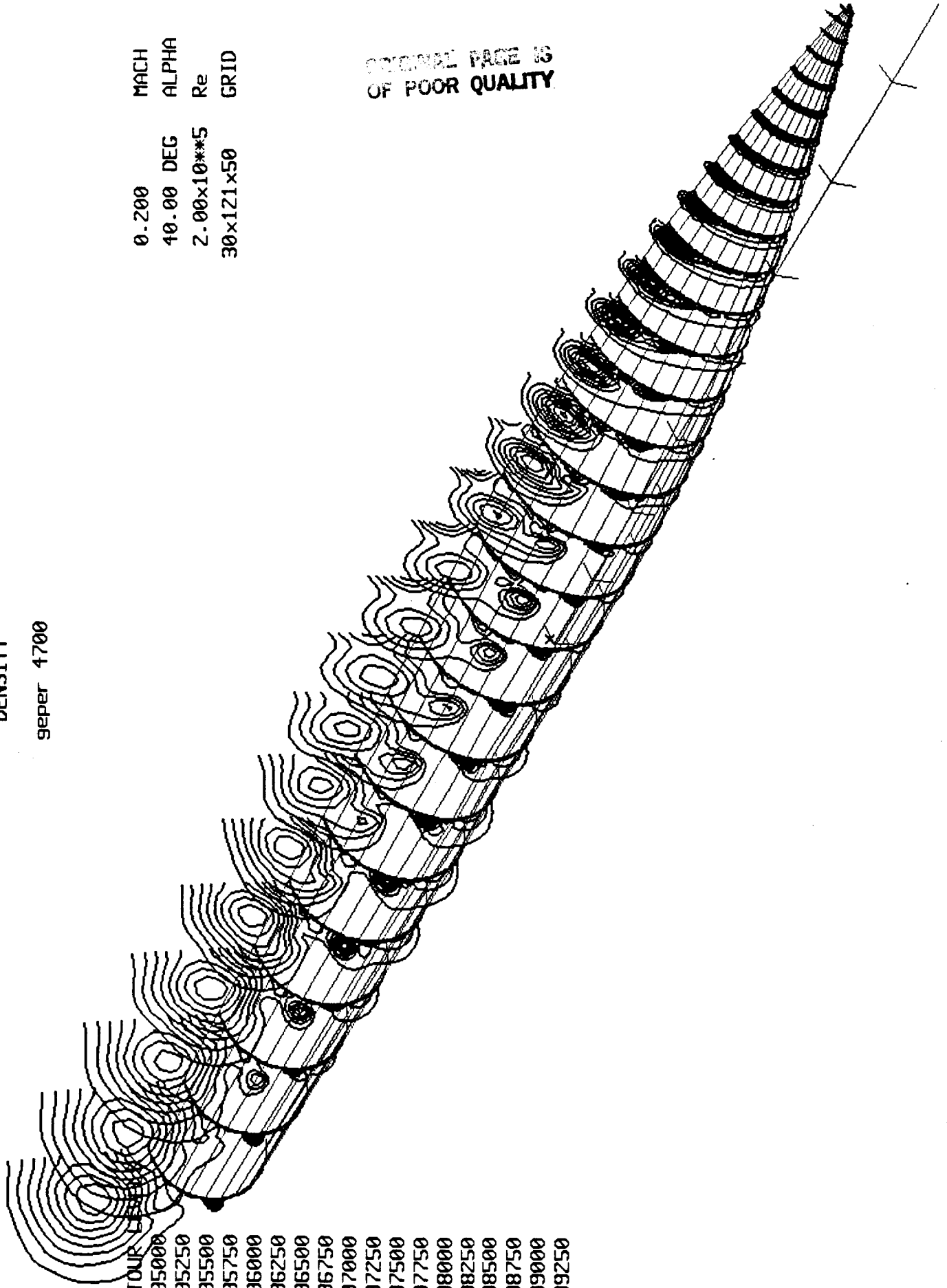


Fig. 29 - Density contours. Left side of the body. Asymmetric case with geometrical disturbance.

DENSITY
geper 4700

CONTOUR LEVELS

0.95000
0.95250
0.95500
0.95750
0.96000
0.96250
0.96500
0.96750
0.97000
0.97250
0.97500
0.97750
0.98000
0.98250
0.98500
0.98750
0.99000
0.99250

MACH 0.200
ALPHA 40.00 DEG
Re 2.00x10**5
GRID 30x121x50

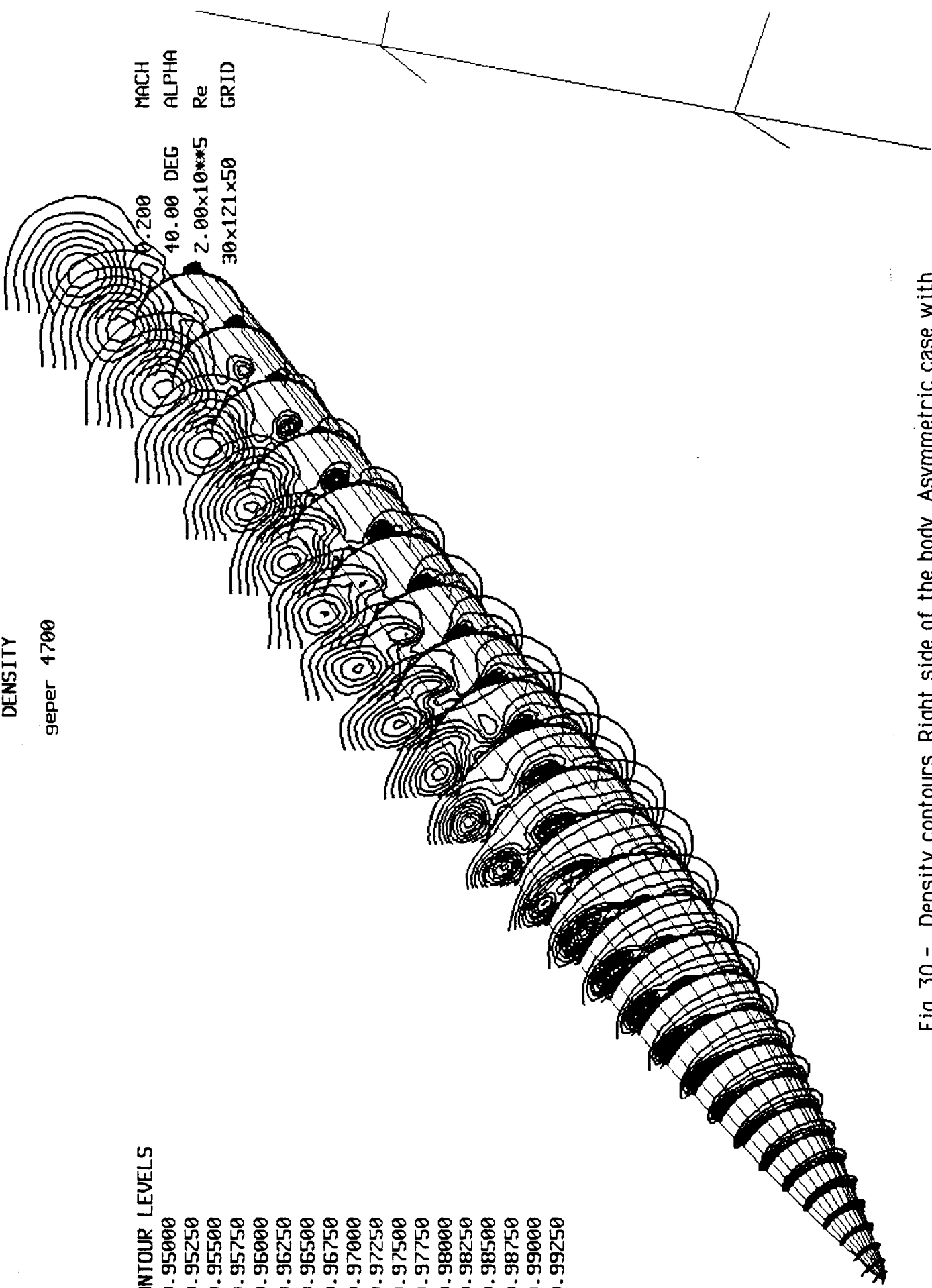


Fig. 30 - Density contours. Right side of the body. Asymmetric case with geometrical disturbance.